

# Hygrothermal Ageing and Damage Characterization in Epoxies and in Epoxy-Glass Interfaces: a Micromechanical Approach Using Embedded Optical Sensors

THÈSE N° 5127 (2011)

PRÉSENTÉE LE 26 AOÛT 2011

À LA FACULTÉ SCIENCES ET TECHNIQUES DE L'INGÉNIEUR  
LABORATOIRE DE MÉCANIQUE APPLIQUÉE ET D'ANALYSE DE FIABILITÉ  
PROGRAMME DOCTORAL EN MÉCANIQUE

ÉCOLE POLYTECHNIQUE FÉDÉRALE DE LAUSANNE

POUR L'OBTENTION DU GRADE DE DOCTEUR ÈS SCIENCES

PAR

**Marco LAI**

acceptée sur proposition du jury:

Prof. J.-F. Molinari, président du jury  
Prof. I. Botsis, directeur de thèse  
Prof. K. Friedrich, rapporteur  
Prof. D. Karalekas, rapporteur  
Prof. V. Michaud, rapporteur



ÉCOLE POLYTECHNIQUE  
FÉDÉRALE DE LAUSANNE

Suisse  
2011



*A zia Peppa*



# Abstract

Nowadays, composite materials are increasingly used in high technology fields such as aerospace and automotive because of the combination of excellent mechanical performance and lightweight. For these characteristics, classical metal alloys are progressively replaced in primary structural components by reinforced polymer composites. The service life of such structural components is more and more increased thus raising questions on the composites' durability since it is well known that they are susceptible to long term aggressive environments. In fact, UV radiations, high temperature, solvents, fuel, humidity and water synergistically act with mechanical loads to reduce the resistance of composite materials.

To address this problem two main approaches are used. On one hand, the macromechanical approach is used for the long term reliability of composite materials that experimentally is characterized by means of accelerated ageing tests that reproduce the service environments. On the other hand, the micromechanical approach is aimed at understanding the intimate degradation mechanisms triggered by the environmental conditions. This objective is partially accomplished by reducing the geometrical complexity of the material microstructure subdividing it into elementary unit cells.

In this work, the combination of moderate high temperature and moisture is chosen as the ageing environment. The effects of the hygrothermal ageing on the properties of an epoxy resin are studied using a single fiber composite (SFC) unit cell.

The reinforcement of the SFC is an optical glass fiber that presents, along a portion of its core, a fiber Bragg grating (FBG) sensor capable of gathering information about the deformation field inside the unit cell.

This particular configuration allows to study evolution of the internal stress state during cure, at high temperatures and during the ageing process.

The residual deformation field in the SFC is investigated by using a mixed experimental-numerical technique. A series of radial cuts are introduced into the SFC geometry while the induced strain perturbation is recorded by the embedded FBG sensor. This knowledge is used in an identification scheme in order to determine a shrinkage function capable of reproducing the initial deformation state in the axisymmetric configuration. The calculated deformation field is in good agreement with similar studies in literature.

The study of the thermomechanical response of the SFC allows to determine the

resin's coefficient of thermal expansion. The procedure is validated in the case of an epoxy resin reinforced with different weight percent of  $SiO_2$  nanoparticles and rubber microparticles. It is shown that the method provides more stable results if compared to the classical TMA analysis.

The resin response to the wet environment at 50°C is characterized firstly by means of a gravimetric analysis that led to the determination of the water diffusion kinetic parameters. Secondly, the mechanical property evolution as function of humidity is determined by means of tensile, multiple relaxation tests and microindentations. Lastly, the resin coefficient of moisture expansion is determined and displays a non linear trend.

A residual-thermo-hygro mechanical model is built on the basis of the determined parameters showing excellent agreement with the recorded experimental data.

Moreover, the hygrothermally induced fiber fracture is analyzed by means of the linear elastic fracture mechanics and the shear lag theory.

Finally, the fiber-matrix debonding, triggered by the reinforcement failure, is characterized by the use of cohesive elements whose mechanical properties are varied as function of the concentration at the interface. The calculated redistribution of stresses after the fiber failure and the debonding kinetic reproduces accurately the recorded experimental behaviour.

**keywords:** single fiber composite, micromechanics, hygrothermal ageing, residual strains, degree of cure, moisture diffusion, thermal expansion coefficient, moisture expansion coefficient, fiber fracture, fiber-matrix debonding, cohesive elements, unidirectional composites, nano fillers, micro fillers.

## Estratto

Oggigiorno i materiali compositi sono crescentemente utilizzati in campi ad alta tecnologia, come l'aerospazio o il settore automobilistico, per la combinazione di eccellenti prestazioni meccaniche e leggerezza. Grazie a queste caratteristiche, le leghe leggere che costituivano i componenti delle strutture portanti sono progressivamente rimpiazzate da compositi a matrice polimerica.

D'altro canto, la durata in servizio di questi componenti è sempre più accresciuta sollevando inevitabili interrogativi sul loro comportamento a lungo termine visto la loro ben nota suscettibilità nei confronti di ambienti aggressivi. In fatti, la radiazione ultravioletta, le alte temperature, la presenza di solventi, carburante e umidità agiscono sinergicamente con i carichi meccanici riducendo la resistenza di questi materiali.

In generale, due tipi di approcci sono utilizzati nell'analisi di questo problema. Dal punto di vista macromeccanico l'affidabilità a lungo termine è caratterizzata per mezzo di tests di invecchiamento rapido che riproducono le condizioni di servizio. D'altro canto, l'approccio micromeccanico è dedicato all'analisi dei fattori di degradazione attivati dall'ambiente in cui questi materiali operano. Questo obiettivo viene raggiunto attraverso una riduzione della complessità della microstruttura del materiale suddividendola in celle elementari.

In questo studio, l'ambiente di invecchiamento scelto è costituito dalla combinazione di moderatamente alte temperature e umidità. L'effetto che questo invecchiamento idrotermico ha sulle proprietà di una resina epossidica sono studiate utilizzando una cella elementare monofibra di un composito (SFC, single fiber composite). Il rinforzo di tale cella è costituito da una fibra ottica al cui interno è stato iscritto un sensore a reticolo di Bragg (FBG, fiber Bragg grating) capace di misurare il campo deformativo all'interno della cella stessa. Questa particolare configurazione permette lo studio dell'evoluzione degli stress interni durante il processo di reticolazione, ad alte temperature e durante il processo di invecchiamento.

Il campo di deformazioni residue nella cella elementare è studiato per mezzo di una tecnica mista sperimentale – numerica. Una serie di incisioni radiali sono introdotte in diverse posizioni della SFC e la corrispondente modifica dello stato deformativo è registrato attraverso il sensore FBG. I dati raccolti vengono quindi inseriti in un processo di identificazione determinando così la funzione di contrazione (shrinkage function) associata.

Lo studio della risposta termomeccanica della SFC permette altresì la determi-

nazione del coefficiente di espansione termica della resina. Questa metodologia è validata nel caso di una matrice epossidica rinforzata da differenti percentuali in peso di nanoparticelle di silice e macroparticelle di caucciù'.

La risposta della resina ad un ambiente caldo umido è determinata in prima istanza attraverso un'analisi gravimetrica e alla successiva determinazione della cinetica di diffusione. In secondo luogo, l'evoluzione delle proprietà meccaniche in funzione della temperatura e della concentrazione d'acqua sono determinate grazie all'utilizzo di test di trazione, rilassamento e macroindentazione. Il coefficiente di espansione all'umidità' è quindi calcolato dimostrando un andamento non lineare.

La determinazione dei parametri sopra citati ha permesso la costruzione di un modello agli elementi finiti che tiene conto delle deformazioni residuali di quelle termiche e igroscopiche.

L'ambiente di invecchiamento imposto induce la rottura del rinforzo e la progressiva rottura dell'interfaccia tra resina e fibra. La rottura della fibra è analizzata attraverso la meccanica della frattura lineare elastica e la teoria dello shear lag. Mentre la propagazione di una cricca all'interfaccia è simulata integrando elementi coesivi, le cui proprietà dipendono dalla concentrazione d'acqua all'interfaccia, nel modello completo menzionato precedentemente.

**Parole chiave:** cella elementare, micromeccanica, invecchiamento idromeccanico, deformazioni residue, elementi coesivi.



## Résumé

En raison de leurs excellentes propriétés mécaniques et de légèreté les matériaux composites sont de nos jours de plus en plus utilisés dans les domaines à haute technologie, comme par exemple l'aéronautique et le secteur automobile. Grâce à ces caractéristiques, les alliages légers qui constituaient les structures principales sont progressivement remplacés par des composites à matrice polymérique. Toutefois, l'accroissement de la durée en service de ces structures entraîne des doutes sur leur comportement à long terme, vu la sensibilité de ces matériaux aux environnements agressifs.

En effet, les rayons UV, les hautes températures, la présence de dissolvants et d'humidité agissent d'une façon synergétique avec les charges mécaniques dans le sens d'une réduction de la résistance de ces matériaux.

En général, deux types d'approche sont utilisés pour l'analyse de cette problématique. D'un point de vue macromécanique, la fiabilité à long terme est caractérisée par des tests de vieillissement rapide qui reproduisent les conditions de service. Par contre, l'approche micromécanique est dédiée à l'analyse des facteurs de dégradation interne causés par l'environnement auquel les structures sont soumises. L'objectif de cette deuxième approche est atteint par la réduction de la complexité microstructurale du composite et sa subdivision en cellules élémentaires.

Dans cette étude, l'environnement de vieillissement choisi est représenté par la combinaison de températures modérément élevées et d'humidité. L'effet que ce vieillissement hygrothermique a sur les propriétés de la résine époxy a été étudié grâce à l'utilisation d'une cellule élémentaire monofibre du composite (SFC, single fiber composite). Le renfort d'une telle cellule est constitué par une fibre optique sur laquelle a été gravé un capteur à réseau de Bragg (FBG, fiber Bragg grating) capable de mesurer le champ de déformation à l'intérieur de la cellule même. Cette configuration particulière permet l'étude de l'évolution des contraintes internes pendant le processus de réticulation, à hautes températures et durant le processus de vieillissement.

Le champ de déformation résiduelle dans la cellule élémentaire est étudié grâce à une méthode mixte expérimentale-numérique. Une série de rainures radiales sont introduites en plusieurs endroits de la cellule et le changement de l'état de déformation est enregistré par le FBG. Les données recueillies sont utilisées dans le contexte d'une identification pour obtenir l'expression de la fonction de retrécissement associée.

L'étude de la réponse thermomécanique du SFC permet la détermination du

coefficient de dilatation thermique de la résine. Cette méthodologie est validée dans le cas d'une matrice époxy renforcée par différents pourcentages de nanoparticules d'oxyde de silicium et de macroparticules de caoutchouc.

La réponse de la résine à un environnement chaud et humide est déterminée premièrement par une analyse gravimétrique et par l'établissement successif de la cinématique de la diffusion. Deuxièmement, l'évolution des propriétés mécaniques en fonction de la température et de l'humidité est obtenue par des tests de traction, de relaxation et de macro-indentation. Le coefficient d'extension à l'humidité est aussi extrait et son comportement non linéaire clarifié.

La détermination des paramètres susmentionnés a permis la construction d'un modèle d'éléments finis qui tient compte des déformations résiduelles ainsi que des déformations thermique et hygroscopique.

L'environnement de vieillissement imposé conduit à la rupture du renfort et à la détérioration progressive de l'interface fibre-matrice. La rupture de la fibre est analysée par la mécanique de la rupture élastique linéaire et par la théorie du shear lag. Par contre, la propagation d'une fissure interfaciale est étudiée par l'introduction dans le modèle numérique susmentionné d'éléments cohésifs, dont les propriétés dépendent de la concentration d'eau à l'interface.

**Mots clés:** cellule élémentaire, micromécanique, vieillissement hygrothermique, déformations résiduelles, éléments finis cohésifs.

## Acknowledgements

I would like to thank, in first place, Prof. John Botsis who gave me the unique opportunity to work in his laboratory and who encouraged and guided me throughout the whole project. His weekly supervision and confidence on my work were extremely helpfull during these four years. In second place, a really special thank goes to Dr. Joël Cugnoni for sharing his knowledge in almost every scientific field, and especially for being always there, even late in the evening, answering to tons of questions and proposing ideas and possibles solutions. I want also to thank Prof. Thomas Gmür for his suggestions and infinite patience in explaining the secrets of french.

Furthermore, many thanks go to the incredible staff of the workshop: Marc Jeanneret, Nicolas Favre and Stéphan Haldner. Their collaboration and effort during these long years were precious not only because of the huge amount of pieces I was asking for but also for the interest in my project and the availability in performing very difficult and unusual machining.

At this point, I would like also to thank the members of the jury for having undertaken the reading of this document and for having shared comments and opinions that made this final version a better work. I also grateful acknowledge the financial support of the Swiss National Science Foundation that has enabled this research work.

I want also to thank all the present and past staff of the LMAF for having created a really enjoyable environment. In particular, a special thank goes to Samuel and Jeannot who started their thesis right before me and that helped me a lot sharing these years of work with enthusiasm.

A really grateful thank is due to Matteo that introduced me to laboratory life and, above all, for his friendship even during the hard times. On the same line, I want to thank Riccardo for all the long and interesting discussions walking back home and the whole “Italian speaking group” with which I passed a lot of really enjoyable time taking profit of this fantastic place.

Finally, many thanks go to my family and close relatives for their permanent support, for their encouragement and understanding since when I took

the decision to start this experience and, later on, during my stay here in Lausanne. Grazie di cuore!

# Contents

<b>1</b>	<b>Introduction</b>	<b>1</b>
1.1	Objectives . . . . .	6
<b>2</b>	<b>Methods</b>	<b>9</b>
2.1	Optical measurement of strains . . . . .	9
2.1.1	Fiber optic sensing: general principles . . . . .	10
2.1.2	Multiplexed sensing . . . . .	13
2.1.3	Optical low coherence reflectometry: OLCR . . . . .	14
2.2	Single fiber composites advantages . . . . .	20
2.2.1	Isostrain justification . . . . .	21
2.3	Inverse methods . . . . .	30
2.3.1	Mixed FEM-Experimental Identification . . . . .	30
<b>3</b>	<b>Specimen preparation</b>	<b>35</b>
3.1	Materials and specimen preparation . . . . .	35
3.2	Specimens' geometries . . . . .	36
<b>4</b>	<b>Resin consolidation analysis</b>	<b>39</b>
4.1	Degree of curing determination . . . . .	40
4.2	Determination of the resin's CTE . . . . .	42
4.3	Application: Particle reinforced resin . . . . .	44
<b>5</b>	<b>Water diffusion analysis</b>	<b>49</b>
5.1	Theory of diffusion . . . . .	49
5.2	Fick's law of diffusion . . . . .	51
5.3	Experimental characterization . . . . .	53
5.4	Diffusion identification . . . . .	54

5.5	Diffusion characteristic time . . . . .	60
<b>6</b>	<b>Material properties evolution</b>	<b>63</b>
6.1	Introduction . . . . .	63
6.2	Tensile and Relaxation tests . . . . .	65
6.3	Indentation tests . . . . .	69
6.3.1	Indentation methodology development . . . . .	70
6.4	Glass transition temperature evolution . . . . .	80
<b>7</b>	<b>Ageing of single fiber composites</b>	<b>83</b>
7.1	Residual stress field determination . . . . .	83
7.1.1	Crack compliance method . . . . .	84
7.1.2	Inverse method approach . . . . .	88
7.2	Hygroscopic deformation . . . . .	93
7.2.1	Coefficient of moisture expansion . . . . .	96
7.2.2	Hygroelastic model . . . . .	99
7.3	Residual-thermo-hygric model . . . . .	103
7.3.1	Elastic model results . . . . .	105
7.3.2	Elastoplastic model . . . . .	106
<b>8</b>	<b>Ageing induced damage</b>	<b>109</b>
8.1	Fiber fracture . . . . .	109
8.1.1	Shear lag analysis . . . . .	111
8.1.2	Linear elastic fracture mechanics approach to interfacial cracks . . . . .	114
8.2	Fiber matrix debonding . . . . .	117
8.2.1	Cohesive-elements approach . . . . .	118
<b>9</b>	<b>Ageing of composites</b>	<b>123</b>
9.1	Specimens preparation . . . . .	123
9.2	Residual deformation and thermal response . . . . .	125
9.3	Diffusion identification . . . . .	126
9.4	composite CME . . . . .	127
<b>10</b>	<b>Conclusions and future work</b>	<b>129</b>
10.1	Synthesis and Conclusion . . . . .	129

---

10.2	Connected problems not directly examined . . . . .	131
10.3	Perspectives . . . . .	132
10.4	Small diameter FBG . . . . .	133
10.4.1	Fiber Bragg grating sensors . . . . .	133
10.4.2	Sample preparation . . . . .	134
10.4.3	Measurement of embedded gratings . . . . .	135
	<b>Bibliography</b>	<b>139</b>





# List of Figures

1.1	Schematic of the mutual interaction among the physics involved in hygrothermal ageing. . . . .	4
2.1	Optical fiber scheme. . . . .	10
2.2	General FBG working principle: a) FBG characteristic response, b) FBG response to a homogeneous fiber stretch. . . . .	11
2.3	Normal strains along a fiber. . . . .	12
2.4	FBG interrogation setup. . . . .	13
2.5	General scheme of multiplexing technique: (a) Serial multiplexing (b) Parallel Multiplexing. . . . .	15
2.6	FBG response to non homogeneous strain field. . . . .	16
2.7	FBG complex impulse conversion to axial strains. . . . .	17
2.8	OLCR setup . . . . .	18
2.9	Middle plane simplification in two cylinders in parallel. . . . .	22
2.10	Total strain evolution as function of the cylinder's stiffness ratio. . . . .	23
2.11	Absolute difference between total strains and $(\alpha_m - \alpha_f)\Delta T$ . . . . .	24
2.12	Shear Lag Model sketch, longitudinal cross section. . . . .	25
2.13	Axial and Shear Stress distribution along the $z$ direction. . . . .	27
2.14	Fiber strains evolution as function of the stiffness ratio $K$ for different values of $R^*$ . . . . .	28
2.15	Error evolution as function of stiffness ratio $K$ and for different values of $R^*$ . . . . .	28
2.16	Axial deformation $\varepsilon_z$ at $z=20$ as function of the normalized radius. . . . .	29
2.17	Mixed FEM-Experimental general identification scheme . . . . .	31
3.2	Specimens' thermal treatments. . . . .	36

3.1	(a) Single fiber specimen vertical mould, (b) dogbone mould. . . . .	37
3.3	Single Fiber Composite scheme. . . . .	38
3.4	Dogbone specimen technical drawing. . . . .	38
4.1	Residual strains evolution during processing. . . . .	41
4.2	fiber strains after post curing and at drying plateau after thermal equilibrium. . . . .	43
4.3	Curing program for epoxy and the modified compounds. . . . .	46
4.4	Residual strains evolution as function of the axial coordinate $z$ for different filler content and type. . . . .	46
4.5	Thermal cycle for CTE measurement. . . . .	46
4.6	Thermal strains at different temperature for the 0_0 configuration. . . . .	47
4.7	Incremental thermal strains for all available fillers compositions. . . . .	48
5.1	Ageing setup. . . . .	53
5.2	Absorption curves for dogbone and single fiber composite cell. Error bars are calculated on the basis of the standard deviation of ten consecutive measurements. . . . .	55
5.3	Details of the FE models: a) details of the mesh at the fiber insertion, b) SFC , c) dogbone specimen. . . . .	57
5.4	Dogbone diffusion identification results: a) calculated and experimental absorption curves, b) relative error. . . . .	58
5.5	SFC diffusion identification results: a) calculated and experimental absorption curves, b) relative error. . . . .	59
5.6	SFC iso-concentration profiles calculated using the concentration dependent diffusion law. Isoconcentration lines at 10%, 25%, 50%, 75%, 90% of the saturation. . . . .	60
5.7	Concentration profiles for the single fiber cell at the specimen middle plane along the radius as function of the diffusion time. . . . .	61
6.1	Tensile and relaxation setup. . . . .	66
6.2	Epoxy stress-strain curve as function of temperature and water concentration. Circles indicate the yield stress. . . . .	67

6.3	Short and long term moduli as function of water volume content, all data points obtained at 50°C. . . . .	68
6.4	Relaxation test profile. . . . .	69
6.5	Detail of the indentation setup. . . . .	71
6.6	Concentration profiles as function of the radius at the SFC cell middle plane. Black crosses indicate the indentation nominal coordinates whereas the green and red ones indicate the maximum positioning error. . . . .	72
6.7	Mesh detail of the indentation model. . . . .	73
6.8	Reaction force evolution as function of the indentation depth as predicted by the indentation model. The Young's modulus of the material is varied linearly with concentration. Extremes cases are represented by the dry resin a room temperature, elastic modulus 2400 MPa, and by an estimation of the maximum drop of the property in fully saturated condition at room temperature (1200 MPa). . . . .	75
6.9	Indentation general scheme. . . . .	76
6.10	Load-indentation depth curve: raw data and correction due to indentation setup stiffness. . . . .	78
6.11	Young's modulus as function of local water concentration at room temperature. . . . .	79
6.12	Comparison of local and averaged E. . . . .	80
6.13	DSC analysis. . . . .	81
7.1	Radial cuts description: (a) Determination of $S_f$ in Colpo et al., determination of $S_f$ close to the edge using identification scheme (b). . . . .	86
7.2	Axial strains evolution after 3 sequential cuts at 2mm 4mm and 9.5mm from the edge. . . . .	89
7.3	Strain difference after each cut. . . . .	90
7.4	$S_f$ identification results. . . . .	92

7.5	Identified shrinkage function. The subscripts in the indicated parameters have the following meanings: $R_6$ indicates that the parameter refers to $r = 6$ mm, $Z_0$ and $Z_{20}$ indicate that the corresponding parameter is calculated at $z = 0$ mm or $z = 20$ mm respectively, $_{0d9}$ indicates that the values correspond to 90% of the horizontal asymptote of the arctan function. . . . .	94
7.6	Local Bragg wavelength and the corresponding evolution of hygroscopic strains. . . . .	95
7.7	Hygroscopic strains as function of water concentration. . . . .	97
7.8	Micrometer measurement locations. . . . .	98
7.9	Evolution of the hygroscopic strain predicted by the coupled hydroelastic model as function of the different hygroscopic expansion laws. . . . .	100
7.10	Comparison of the predicted hygroscopic strains evolution with the experimental micrometer data. . . . .	102
7.11	UEXPAN subroutine description. . . . .	105
7.12	Experimental fiber strains and prediction obtained with the residual-thermal-hygro model. . . . .	106
7.13	Comparison between elastic and elasto-plastic model predictions. . . . .	107
8.1	Fiber failure evidence. . . . .	110
8.2	Fiber strains evolution: a) right before fracture and just after, b) long time exposure. . . . .	112
8.3	Evolution of the stress-efficiency as function of the ageing time. . . . .	113
8.4	Shear lag stress plateau evolution as function of the exposure time. . . . .	113
8.5	Shear stress distribution as function of the distance from the fiber failure at the early stage of diffusion and close to saturation. . . . .	114
8.6	Fiber fracture and fiber-matrix debonding locations. . . . .	116
8.7	Evolution of the $\Psi$ angle with the exposure time. . . . .	117
8.8	Cohesive law evolution with concentration at the interface: quadratic dependency. . . . .	120

---

8.9	Fiber matrix debonding propagation: comparison between experimental data and predictions. (a) right after fracture, (b) long time exposure. . . . .	121
8.10	Debonding length evolution of the interface crack at the specimen edge. Comparison with FE prediction. . . . .	122
8.11	Influence of plasticity on the propagation rate. . . . .	122
9.1	Composite plate processing cycle inside autoclave. . . . .	124
9.2	Composite preparation details. . . . .	124
9.3	Composite specimen geometries for longitudinal strain deformation (a), and transverse strain deformation (b). . . . .	125
9.4	Composite absorption curves: experimental data and identification predictions. . . . .	127
9.5	Composite hygroscopic expansion: longitudinal and transverse deformation. . . . .	128
10.1	Wavelength shift as a function of the applied axial stress for (a) standard single-mode fiber (SMF-28 125 $\mu\text{m}$ ) and (b) for a small-diameter fiber (SF-50, 50 $\mu\text{m}$ ). . . . .	134
10.2	Rectangular epoxy sample (10x10x40 mm) with embedded FBG (a) and mould for specimen preparation (b): RB: rubber stripes; PL: plane to support the fiber; CP: cap with openings. . . . .	135
10.3	Reflection spectra (a) and OLCR phase measurement (b) for FBGs written in SFM-28 before (black) and after embedding (red). The reflectivity was normalized to 0 dB. . . . .	136
10.4	Reflection spectra (a) and OLCR phase measurement (b) for FBGs written in small diameter fibers from SILITEC SA (SF-50) before (black) and after embedding (red). The reflectivity was normalized to 0 dB. . . . .	136
10.5	Distribution of the non-homogeneous internal strain along the FBG length inside epoxy specimen measured (a) and numerical simulation with 1°C decrease on the matrix, (b) for SMF-28 and small diameter fibers. . . . .	138



# List of Tables

2.1	Evolution of the total deformation for the two cylinders approximation of the stress-strain state in the middle plane of the single fiber composite. . . . .	24
4.1	Evolution of the degree of conversion with the progression of the processing cycle. . . . .	42
4.2	Resin coefficient of thermal expansion. . . . .	43
4.3	Compositions of the nanocomposites and hybrid compounds in vol.%, and their designations. . . . .	45
4.4	Coefficients of thermal expansion for all the materials considered. . . . .	48
5.1	Identified parameter: Fick's law of diffusion. . . . .	56
5.2	Identified parameters: Concentration dependent diffusion. . . . .	56
7.1	$S_f$ identified parameters. . . . .	93
9.1	Composite longitudinal and transverse coefficient of thermal expansion. . . . .	126
9.2	Identified diffusion parameters. . . . .	126
9.3	Composite coefficients of moisture absorption. . . . .	128





# Chapter 1

## Introduction

The desire of producing new and more performant materials is one of the powerful motivation that led, and leads today, the science and engineering community to invest in material research. Simultaneously, the same effort is put in extending the limits of existing materials regarding their mechanical performance, low weight and resistance to environmental effects and wear. Fiber reinforced materials are designed to combine components in such a way to obtain composites that, in spite of their lightweight, maintain high strength and stiffness. In view of these characteristics, the aerospace industry began to build the aircraft's primary-structures utilizing these materials. In addition, the actual design philosophy foresees to keep structures in service for an increasingly long time range and to reduce the number of the periodic inspections so to lower the maintenance costs.

For these reasons, a precise understanding of the long term effects, that the synergistic combination of the service environments and mechanical loads have on the residual properties of the structure, is necessary. In fact, it is well known that high temperatures, UV-radiation, solvents, fuel, humidity and water are the principle causes for composites deterioration. Without an adequate protection, the composite constituents can be attacked by these aggressive environments generating an inexorable decrease of their synergistic performance.

To address this problem, pertinent accelerated ageing methodologies were developed to estimate the long term response of composites. Moreover, investigating the ageing of such class of materials requires the development of three different competences. Firstly, the understanding of the chemical processes

that take place during fabrication, secondly the identification of a preferred ageing environment and the interplay between the physics involved, thirdly the mastering of the chemical-physical changes that drive the development of the damage in the material. These three topics and their importance are summarized as follows:

1. Composite manufacturing introduces a non homogeneous distribution of residual stresses that, depending on the constituents, the imposed thermal cycles and the geometry, can become relevant in generating local failure in the material. In particular, internal stresses induce a contraction of the failure envelop of the structure especially when it is subjected to complex load states like biaxial transverse loading or combined shear and normal loading [1].
2. Furthermore, the selection of a reasonably simple, but still representative, ageing environment is somehow difficult because of the complexity of the coupling between the involved parameters. However, it is highlighted in [2] that the most common ageing factors are high temperature and moisture. (For this reason, the present work is dedicated to the hygrothermal ageing.) A general schematic of the interaction between the parameters involved in this specific case is reported in Fig.1.1. It can be noticed that heat and moisture diffusion are strongly related since the diffusion kinetic and the saturation level depend exponentially on the temperature and on the concentration itself [3]. By its nature the concentration field evolves in time during the ageing process and can be calculated on the basis of an appropriate diffusion law. Usually, the Fick's law of diffusion is assumed although, for composites materials, experimental evidence has shown that it is not always the correct model [4–6]. In addition, temperature and moisture have an additive detrimental influence on the mechanical properties of the resin [7–9]. This has repercussions on the matrix dominated properties of the composites as reported by [10–12].
3. The ageing effects listed above influence the durability of the composite and the rate at which the mechanical properties decrease [13]. In fact, the composite's dominant failure modes are directly related to the specifics

of the environment and to the constituents that are the most susceptible. For example, a laminate failure, caused by the fracture of the reinforcements, is common in E-glass reinforced composites when subjected to humidity. In fact, moisture is able to degrade the strength of glass fibers that suffer from chemical decomposition and stress corrosion cracking [14]. In this case, the appropriate choice of the glass used in the filaments can reduce considerably the fibers' susceptibility [14–17]. For what concerns the matrix, swelling plasticization and hydrolysis are the primary responsible for degradation of its mechanical properties [18–24]. In addition, microcracking accelerates the diffusion process since it opens new water penetration paths. Moreover, swelling of the matrix induces shear stresses along the interfaces. Thus, it causes interfacial debonding when the maximum stress exceeds the interfacial shear strength (IFSS) [25–27]. The magnitude of the latter parameter is found to decrease with the water content and reduces the ability of the interfaces to sustain and transfer mechanical loads [12].

On the light of the above discussion, the broadness and richness of the ageing process in composites is clear. At present, two main approaches towards this problem are established in the scientific community: a macromechanical and a micromechanical one.

The first one involves the study of the composite as a whole and the determination of its long-term response to pertinent ageing environments. This approach is absolutely necessary in the way that it constitutes a process of material characterization and becomes extremely helpful in the context of structural design. In fact, depending on the foreseen service environment, the composite with the more appropriate characteristics can be successfully selected. In this case, there is no attention to the mechanisms that generate the decrease of the material properties, conversely this approach focuses on the determination of their maximum drop and to the rate at which it takes place.

The second approach is aimed at understanding the intimate nature of the mechanisms that produce the progressive degradation of the composite. In this framework, the composite is considered as an ensemble of elementary constituents that are characterized separately and tested together using a sim-

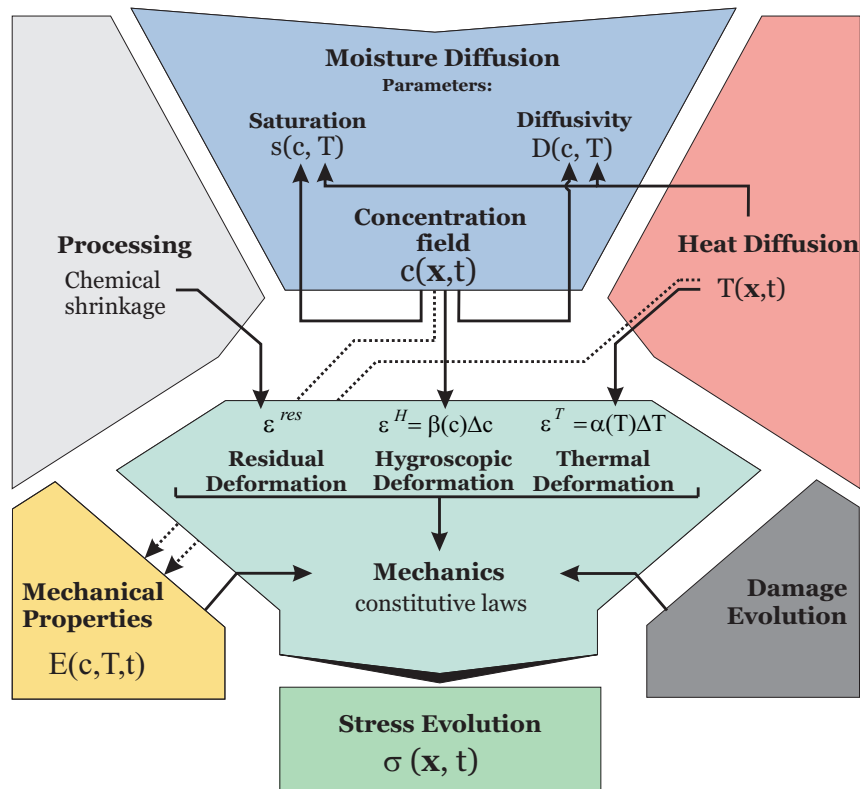


Figure 1.1: Schematic of the mutual interaction among the physics involved in hygrothermal ageing.

plified geometrical assembly called composite unit cell. As the complexity of the unite cell increases, different mechanisms and quantities can be studied.

The simplest unit cell is the single fiber composite (SFC). It has been used in multiple configurations for the determination of the strength of the interface. In particular, fiber pull-out [28–34] and push-out [35–37] tests as well as single fiber fragmentation tests (SFFT) [38–42] are the most common procedures for interface characterization and they have been used to determine the effectiveness of fiber sizing. The Silane additive, for example, enhancing the strength of the interface, displaces the fracture locus from the interface to the matrix [43, 44]. Moreover, especially for what concerns the SFFT, the negative influence of water concentration and temperature on the interfacial strength was addressed in [12, 45].

The increase of the number of reinforcement positioned in a regular array allows to study the fiber to fiber interaction in the case of the failure of one of the reinforcements [46–48]. Furthermore, non regular fiber distribution, randomly generated or determined by real micrographs of composites, can be used to determine the influence of fibers bundles on the mechanical response [49].

A further insight on the interface characterization is given by the combination of the micromechanical tests reported above and methods for the direct measurements of fiber deformation during testing. In this context, the use of the Raman spectroscopy [23, 24, 50, 51] and X-ray diffraction [52, 53] open the possibility to determine the interfacial shear strength based on the shear lag approach and on the experimentally determined deformation of the filament.

This point is further developed in this work with the use of embedded optical sensors that allow to determine the deformation of the fiber with a greater accuracy in comparison with the previous methods. In particular, distributed sensing on long fiber Bragg gratings (FBG) is performed using the optical law coherent reflectometry (OLCR). With this technique, the redistribution of stresses around a fiber failure can be reconstructed and the fiber-matrix debonding can be also monitored.

## 1.1 Objectives

The objective of this work is to establish a complete methodology for the characterization of the hygrothermal ageing of single fiber composites. The proposed methodology exploits the advantages of embedding an optical fiber with a long FBG sensors in a single fiber composite. The optical fiber replaces the reinforcement and allows to follow the internal state of the elementary cell during the ageing process starting from fabrication.

The research work includes the following tasks:

- determination of the residual stress state developed during processing
- development and control of an appropriate ageing environment
- determination of the material properties evolution of the matrix during the hygrothermal exposure
- development of a coupled residual-thermo-hygro FE model
- analysis of the ageing induced damage

The document is divided according to the reported main topics into 10 chapters. In Chapter 2, an overview of the experimental and numerical methods used in this work is presented. It contains a review of the principal methodologies for optical strain sensing, demonstration of the advantages of a single fiber composite, and the description of the mixed FEM-experimental identification procedure.

Afterwards, the process of production of the single fiber composite is described in Chapter 3.

Chapter 4 is dedicated to the analysis of the resin consolidation by means of the determination of the degree of curing. In addition, the thermo-mechanical response of the resin is characterized by the determination of its coefficient of thermal expansion. The methodology is then validated in the case of nano-micro particle reinforced epoxy.

In Chapter 5, the ageing environment is presented and the kinetic of water diffusion determined by gravimetric analysis and the identification procedure.

In Chapter 6, the evolution of the short and long term modulus of the resin as function of water content at 50°C is investigated firstly by means of tensile

and relaxation tests and secondly using a semi-developed indentation procedure. Finally, the evolution of the glass transition temperature as function of the water content is conducted by means of DSC measurements performed on the resin in dry and full saturated conditions.

The development of the residual-thermal-hygric FE model is reported in Chapter 7. The residual deformation field is determined by introducing a series of radial cracks in the SFC and by using the identification procedure. Next the resin coefficient of moisture expansion is determined and used in the development of the pure hygroscopic FE model. Finally, a model that couples the residual and the thermo-hygric contribution is built by means of a UEXPAN subroutine coded for the Abaqus FE software.

The damage produced during the ageing process is characterized in Chapter 8. The analysis is conducted firstly on the basis of the linear elastic fracture mechanics (LEFM) approach and the shear lag theory. Secondly, cohesive elements are introduced in the coupled model. The properties of the cohesive elements are varied with the water content at the interface.

In Chapter 9, the developed methodology is used to determine the coefficients of moisture expansion of unidirectional laminates.

Lastly, Chapter 10 summarizes the experimental work and the simulation results and presents also the author's conclusions and recommendation for future works.





# Chapter 2

## Methods

This chapter is dedicated to the general methods of investigation used throughout the work. In the following pages the basic concepts of strain sensing using fiber Bragg grating and low coherence reflectometry are reviewed. The identification of materials properties using a mixed numerical-experimental scheme is also presented since its general approach is used extensively in different parts. In this context, the use of a single fiber composite is fully exploited because of its characteristics as it is explained in section 2.2.

### 2.1 Optical measurement of strains

Deformation measurement has always had a vital role in monitoring structures under service conditions or during the testing phase at laboratory level. The preferred means to accomplish this task has always been identified in strain-gauges due to their relative ease of use and affordable price. On the other hand the information they provide is referred to the external surface of the object under study. If this characteristic is unavoidable for metal components, for composite based structures there are attempts of embedding strain gauges among the plies with the aim of retrieving strain information inside the laminate. Beside the instrumentation problems that arise from such an approach, the influence that such relative big inclusions have on the strain field need to be addressed. In this framework, interferometric optical sensors like fiber Bragg gratings (FBG) have earned increasing relevance because of the relatively small diameter of the fibers, characteristic that permit them of being

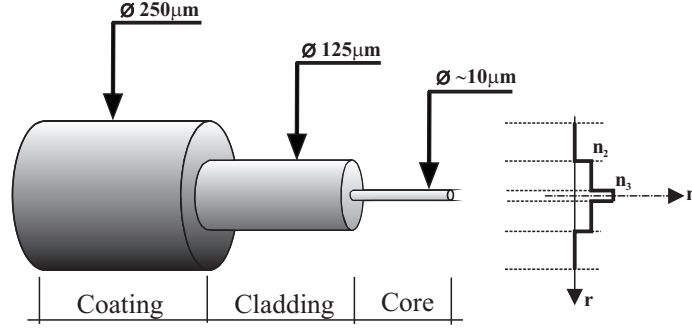


Figure 2.1: Optical fiber scheme.

embedded with minimal intrusiveness, high strain resolution (up to  $50\mu\epsilon$ ), self reference property, due to encoding in the wavelength domain and long life time. The ensemble of these characteristics makes FBGs very useful in experimental mechanics and in structural monitoring.

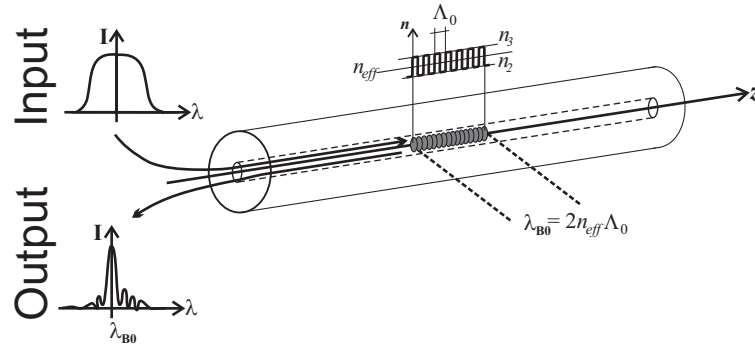
### 2.1.1 Fiber optic sensing: general principles

The optical fiber used in this work is a standard single mode (SM) telecommunication fiber whose basic structure is composed of an external coating, generally made of polyimide or polyacrylate, preserving the bare glass fiber from environmental attacks and accidental damages, and the proper glass fiber that is subdivided in cladding and core (Figure 2.1). The latter, having a higher refractive index in comparison with the cladding, is dedicated to the transmission of the light signal whereas the cladding reduces losses of light from the core into the external environment.

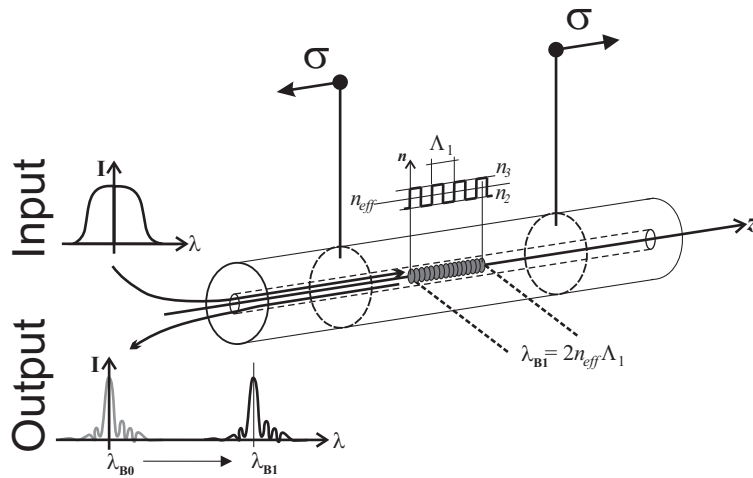
The exposure to ultraviolet radiation of the germanium doped core of the SM fiber alters its refractive index. This periodic modulation is called Fiber Bragg Grating (FBG) and the evolution of the effective refractive index of the core, as function of the axial coordinate  $z$ , can be described as:

$$\begin{aligned} n(z) &= n_2 + \Delta n_{ac}(z) \cos\left(\frac{2\pi}{\Lambda_0}z + \theta(z)\right) + \Delta n_{dc}(z) \\ &= n_{eff} + \Delta n_{ac}(z) \cos\left(\frac{2\pi}{\Lambda_0}z + \theta(z)\right) \end{aligned} \quad (2.1)$$

Here  $\Delta n_{ac}(z)$  is the amplitude index change,  $\Lambda_0$  is the period of the induced modulation,  $\Delta n_{dc}(z)$  is the mean index change and  $\theta(z)$  is the grating chirping. If after production  $\Delta n_{ac}(z)$ ,  $\Delta n_{dc}(z)$  and  $\theta(z)$  are independent of  $z$  the grating



(a) FBG characteristic response



(b) FBG response to a uniform fiber stretch.

Figure 2.2: General FBG working principle: a) FBG characteristic response, b) FBG response to a homogeneous fiber stretch.

is called uniform. All the gratings used in this work satisfy these conditions. The irradiated zone of the fiber acquires the capability of reflecting a narrow band of light around a specific wavelength once a broadband light is coupled into it. This wavelength, called Bragg wavelength, is proportional to the effective refractive index of the core  $n_{eff}$  and the period of the induced modulation  $\Lambda_0$  according to  $\lambda_{B0} = 2n_{eff}\Lambda_0$  (Figure 2.2a).

Every external action, that introduces a variation in  $\Lambda_0$  and  $n_{eff}$ , results in a modification of the reflected spectrum. For example, if a constant deformation  $\varepsilon_z$  and a temperature difference are imposed to the fiber the change in the Bragg wavelength is proportional to the axial strain on the sensor (Figure 2.2b). In this case a simple relationship between peaks wavelength and strain holds:

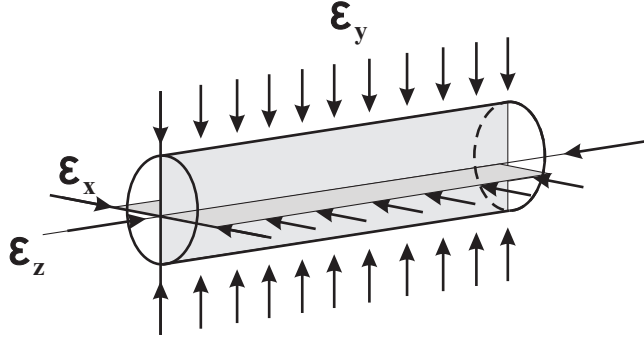


Figure 2.3: Normal strains along a fiber.

$$\frac{\lambda_{B1} - \lambda_{B0}}{\lambda_{B0}} = (1 - p_e) \varepsilon_z + (\alpha_f + \xi) \Delta T \quad (2.2)$$

where  $p_e$  is the optomechanical parameter having the value of 0.215 [54],  $\alpha_f = 0.5 \times 10^{-7} C^{-1}$  is the fiber coefficient of thermal expansion,  $\xi = 8.916 \times 10^{-6} C^{-1}$  [55] is the thermo-optic constant and  $\Delta T$  expresses the temperature difference between two measurements.

Note that the use of (2.2) for strain calculation assumes that the fiber is loaded axisymmetrically (Fig.2.3), so that the transverse deformations of the fiber are small compared to axial one and the following approximation holds:

$$\varepsilon_x = \varepsilon_y = -\nu_f \varepsilon_z \quad (2.3)$$

where  $\nu_f = 0.19$  is the fiber Poisson's ratio. If this conditions are not respected the parameter  $p_e$  loses its significance invalidating the (2.2). In this case (2.2) is replaced by:

$$\frac{\lambda_{B1} - \lambda_{B0}}{\lambda_{B0}} = \varepsilon_z - \frac{n_{eff}^2}{2} [p_{11} \varepsilon_x + p_{12} (\varepsilon_y + \varepsilon_z)] + (\alpha_f + \xi) \Delta T \quad (2.4)$$

where  $p_{11} \approx 0.113$  and  $p_{12} \approx 0.252$  [56] are the Pockel's strain optic constants. In particular substituting (2.3) in (2.4) it is found that

$$p_e = \frac{n_{eff}^2}{2} [p_{12} - \nu_f (p_{11} + p_{12})] \quad (2.5)$$

Considering the characteristics of the specimen used in this work, the condi-

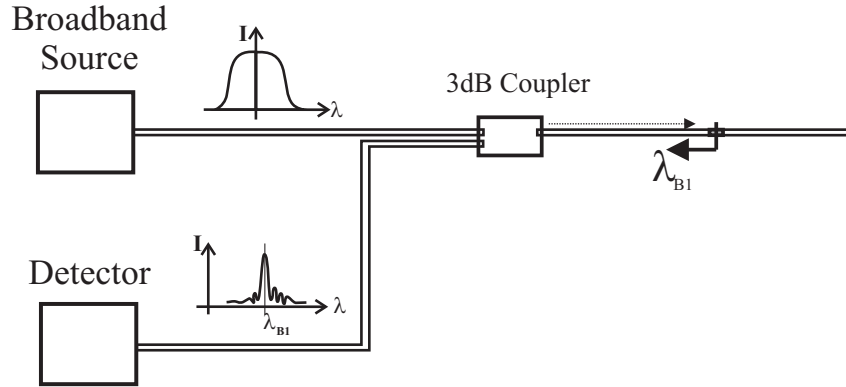


Figure 2.4: FBG interrogation setup.

tions (2.3) are always assumed to hold in this work. The working principle illustrated above is exploited in reality by the use of a simple wavelength measurement setup illustrated in Fig.2.4.

It consists of a broad band source, with a Gaussian profile centered at 1300nm (or 1500nm), and a photodetector that measures the intensity of the light back reflected from the FBG as function of the wavelength. The maximum intensity of this reflected spectrum corresponds to the Bragg wavelength. Monitoring the shift of this wavelength and using (2.2) the fiber deformation can be determined if the  $\Delta T = 0$  or if information on the temperature difference between the reference measurement and the actual one are known.

This implies that, since deformation and temperature induce coupled effects on the FBG response, two distinct measurements are necessary for the determination of both quantities. This is usually done in two principle ways:

- Temperature compensation is provided by an auxiliary temperature measurement, usually a close embedded thermocouple.
- A second grating is isolated from the structure thus sensing only the temperature field.

Other means, based on the same principle are possible [57, 58] .

### 2.1.2 Multiplexed sensing

The characteristics underlined in Section 2.1.1 make the use of FBGs as point sensor for measurements of strain and temperature very attractive in composite

materials.

However the first and immediate limitation of point sensing for large structures is that normally is desirable to know simultaneously the deformation at different locations of the structure. It is here that the idea of multiply the number of the sensors gives birth to the multiplex sensing. Two general schemes are the most common: *serial* and *parallel multiplexing* [59]. In the serial multiplexing (2.5a) a series of FBG sensors can be inscribed in a single fiber at different locations whereas in the parallel multiplexing (2.5b) the array of FBG sensors is distributed in multiple fibers. The working principle is the same as in the case of one single FBG and the experimental setup is quite similar: a unique broad band light source is used to interrogate all the sensors and all the reflected spectra are read by a photodetector. The only necessary adroitness is varying the Bragg wavelength of each sensor during the manufacturing in such a way that the responce will not overlap in the reference state nor in each of the possible loaded state when the Bragg wavelengths change. Moreover, the total length of the grating is kept as small as possible. Infact, a non uniform strain field at the FBG location can still be considered quasi constant over a small gages length keeping unaltered the reflected spectrum shape and thus the validity of (2.2)

The serial multiplexing has the advantage of the use a single fiber and thus a single defect line is introduced on the composite. The distance between the sensors can be reduced up to 2 mm giving the opportunity of sensing strain gradients in a very small region. On the other hand in large structures the parallel multiplexing is more common since a judicious planning of the sensor positioning allows for sensing at different locations that can be very distant among each other.

### 2.1.3 Optical low coherence reflectometry: OLCR

When non-homogeneous strains are applied on a long FBG the shape of the reflected spectrum is not conserved and multiple peaks and broadening of the peaks are observed (Fig.2.6).

This happens when a uniform FBG is subjected to a non homogeneous strain field. In this case, different parts of the grating reflect light at different wavelengths creating peaks whose intensity is related to the extension of

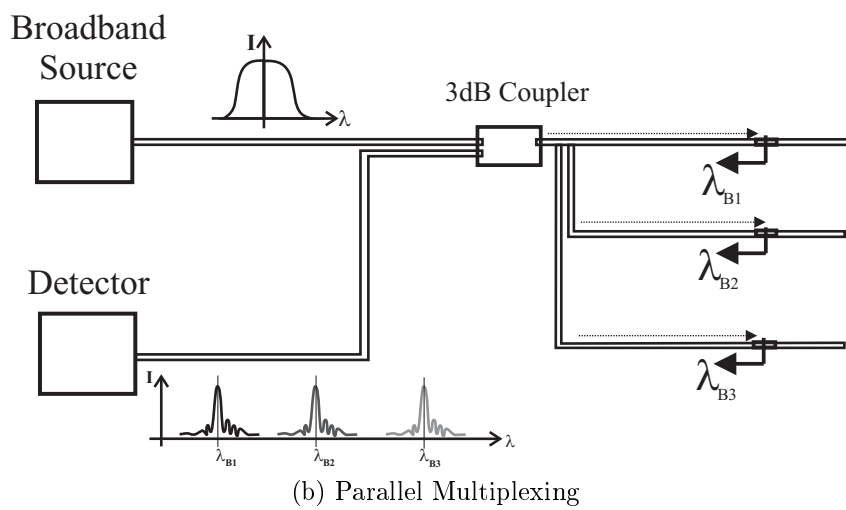
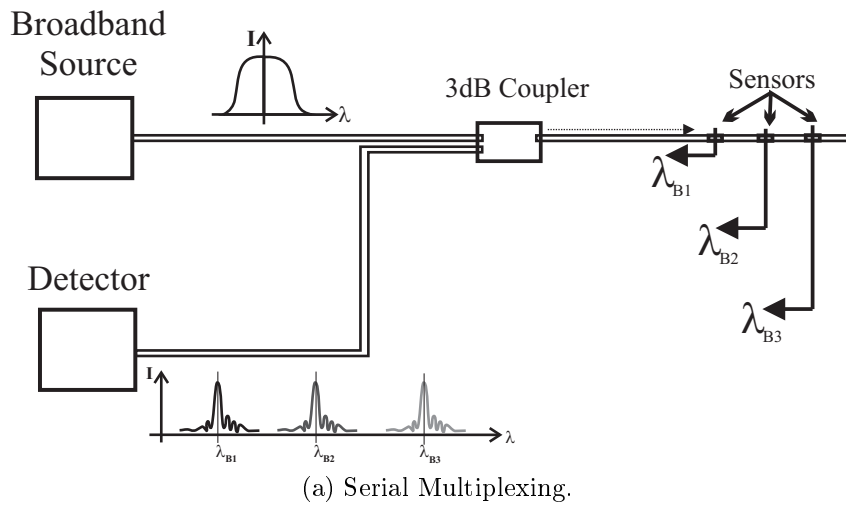


Figure 2.5: General scheme of multiplexing technique: (a) Serial multiplexing (b) Parallel Multiplexing.

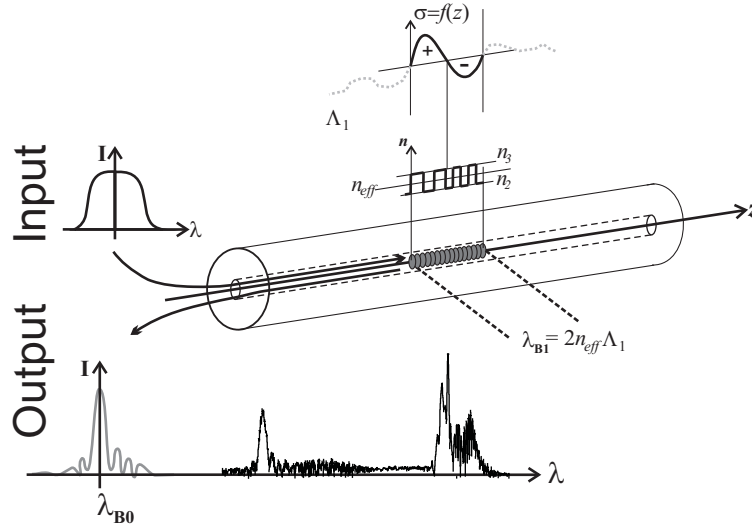


Figure 2.6: FBG response to non homogeneous strain field.

the grating portion having same deformation. The larger the zones equally stretched the stronger the signal back reflected from those parts. Since the reflected spectrum is a cumulative quantity, in the sense that it represents the sum of all the light intensities reflected by each partion of the grating, it appears broadened when the strain gradient is high since a wide range of wavelength are excited. On the other hand multiple narrow peaks are the result of different parts of the grating subjected to practically constant but different deformations. Moreover, because of its integral characteristic the reflected spectrum does not contain spatial information on where the different deformation levels are applied along the fiber axis. For all these reasons, the spectral response is not easy to interpret and (2.2) or (2.4) cannot be used for strain calculation. In this case, a different type of analysis is required in order to reconstruct the strain field as function of the position: the Optical Low Coherence Reflectometry (OLCR).

It is known that the FBG response can be characterized in three different domains [60]: *space domain*, *frequency domain* and in *time domain*. Each of these representations is equivalent and, depending on which information is looked for, it is possible, but not always easy, to measure one of the response and calculate the others.

In the next few paragraphs the link between the periodic modulation of the refractive index in the FBG and the reflected spectrum will be explained.



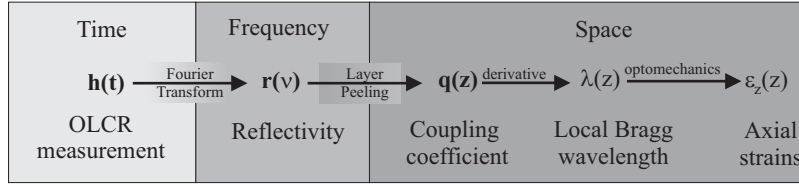


Figure 2.7: FBG complex impulse conversion to axial strains.

The OLCR setup necessary for the precise measurement of the FBG complex impulse response is illustrated and the local Bragg wavelength definition is introduced.

The back propagating spectrum envelope  $u$  and the transmitted one  $v$ , generated by the modulation (2.1) of the refractive index at the FBG position, can be expressed, according to the coupled mode theory [61], in terms of the complex coupling coefficient  $q(z)$ :

$$\frac{du(z, \delta)}{dz} = i\delta u + q(z) v \quad (2.6)$$

$$\frac{dv(z, \delta)}{dz} = -i\delta v + \bar{q}(z) u \quad (2.7)$$

where  $\delta$  is the wave number detuning and  $\bar{q}(z)$  is the complex conjugate of  $q(z)$ . The amplitude  $|q(z)|$  and phase  $\phi(z)$  of  $q(z)$  are given by:

$$|q(z)| = \frac{\eta\pi\Delta n_{ac}(z)}{\lambda} \quad (2.8)$$

$$\phi(z) = \frac{\pi}{2} + \theta(z) - \frac{4\pi}{\lambda}\eta \int \Delta n_{ac}(z) dz \quad (2.9)$$

where  $\eta$  is the fraction of modal power completely contained in the fiber core. From (2.6) and (2.7) and knowing the amplitude and phase of the complex coupling coefficient it is possible to find  $u$  and  $v$ . The optical low coherence reflectometry and the layer peeling algorithm measure the FBG complex impulse response  $h(t)$  in the time domain which allows for the calculation of the complex coupling coefficient  $q(z)$ , by Fourier transform, and the local Bragg wavelength reconstruction. The algorithm is schematically illustrated in Fig.2.7.

The core of the OLCR setup is the Michelson interferometer whose arms

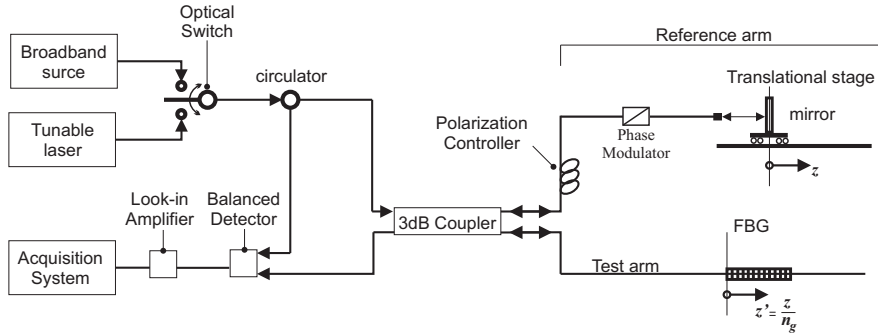


Figure 2.8: OLCR setup

are labeled test and reference arm (Fig.2.8). Light from the broadband source and tunable laser are alternatively injected using the optical switch. The transferred signal passes through an optical circulator and then is splitted into the test and the reference arm using a 3dB directional coupler. The tunable laser provides the reference for the phase measurement. Light from the reference and test arm is reflected back and interferes inside the coupler only if the optical length difference of the two arms is smaller than the coherence length  $L_c \simeq 25\mu m$  of the light source.

The resulting interference signal corresponds to the impulse response  $h(t)$  smoothed over a few micrometers corresponding to half of the coherence length. Moving the mirror in the reference arm, the optical distance is artificially varied causing light, reflected from the mirror, to interfere with the light coming from different FBG positions. An induced displacement  $\Delta z$  of the mirror in the reference arm “selects” the light back reflected from the FBG in the test arm at a distance  $\Delta z' = \Delta z/n_g$  from the previous point. Note that  $n_g$  is the fiber refractive group index. The FBG in the test arm is then completely scanned with a maximum spatial resolution given by half the coherence length of the light source.

The light is detected using two photodiodes in a balanced detection scheme and a lock-in amplifier which extracts phase and amplitude of the interference signal, i.e, of the complex impulse response  $h(t)$ . For every position of the translation stage, i.e, for each grating point, amplitude and phase difference between the Bragg reflected broadband light and the tunable laser light are measured. More details on the OLCR setup and procedures can be found in reference [60].

At this point, knowing  $h(t)$  the spectral response  $r(\nu)$  in the frequency domain is calculated by Fourier transform. Next the complex coupling coefficient  $q(z)$  is determined by the layer peeling procedure [62,63]. Finally the local Bragg wavelength  $\lambda_B(z)$  is obtained in terms of the derivative of the phase of the complex coupling coefficient:

$$\lambda_B(z) = 2n_{eff}\Lambda \left( 1 + \frac{\Lambda}{2\pi} \frac{d\phi(z)}{dz} \right)^{-1} \quad (2.10)$$

The local Bragg wavelength (LBW)  $\lambda_B(z)$  is the wavelength belonging to each FBG interval probed with the mirror displacement and thus it is a function of the axial coordinate  $z$ . In this case, the optomechanical equation (2.2) takes the following form:

$$\frac{\lambda_B(z) - \lambda_{B0}(z)}{\lambda_{B0}(z)} = (1 - p_e) \varepsilon_z(z) + (\alpha_f + \xi) \Delta T \quad (2.11)$$

where the non homogeneous strain field  $\varepsilon_z(z)$  is fully reconstructed as function of the  $z$  position in the grating. Note that, in the case where an equivalent unidimensional deformation field is known to take place along the grating the general equation (2.11) can be specialized expressing the term  $\varepsilon_z(z)$  according to its source. In fact, the axial deformation can originate from the progressive shrinkage during the curing process, from coefficient of thermal expansion mismatch between fiber and matrix, or from the swelling of the surrounding medium due to humidity absorption. The (2.11) takes the following form:

$$\begin{aligned} \frac{\lambda_{B1} - \lambda_{B0}}{\lambda_{B0}} = & \underbrace{(1 - p_e) (\alpha_m - \alpha_f) \Delta T}_{\text{thermal strains}} + \underbrace{(1 - p_e) \alpha_{chem} \Delta \gamma}_{\text{chemical curing shrinkage}} + \\ & \underbrace{(1 - p_e) \beta \Delta c}_{\text{moisture absorption swelling}} + \underbrace{(\alpha_f + \xi) \Delta T}_{\text{temperature compensation}} + \dots \end{aligned} \quad (2.12)$$

Note that in (2.12) the spatial coordinate has been removed since its validity refers to a homogeneous stress state. In the section (2.2) it is demonstrated that such zone is indeed present in the inner part of the SFC. Moreover, the range of validity of Eq.(2.12) is explored in the case of thermal strains using simplified analytical models. The same principle can be extended to all the components in equation (2.12).

## 2.2 Single Fiber Composite (SFC): description and advantages

Composite materials result from the combination of the best characteristics of two or more components generating a new material with innovative properties. The coexistence of these materials gives the origin to residual strains during processing and non homogeneous repartition of stresses during service condition whose great part is sustained by the component with better mechanical properties. Moreover, the load transfer efficiency among the reinforcements, ensured by the interfaces and the matrix, is a key parameter in composites making its study priority field of research. In this frame, the investigation on the mutual exchange of stresses between matrix and reinforcement was addressed in the past by reducing the geometrical complexity of the problem. Elementary unit cells, presenting a reduced amount of components, were considered in order establish the influence that different parameters, like elastic properties of the constituents, their spatial distribution, strength of the interfaces etc..., have on the final properties of the global composite. In general multiple fibers cells are considered in order to obtain homogenized properties of the composites using the volume fraction of the constituents and/or their real distribution obtained from micrographs. For what concerns single fiber unit cells they have been employed especially in the study of the fiber/matrix interfacial shear strength in fragmentation tests.

In this study, the single fiber composite, whose geometry is reported in Section 3.2, presents the advantage of having in the optical fiber an active component. In fact the optical fiber contains a long FBG sensor allowing for distributed strain measurement. This unique capability is fully exploited in Chapters 4 and Chapter 7 for the determination of important material properties of the surrounding matrix like the coefficient of thermal expansion and the coefficient of moisture expansion. Moreover, it is used for the determination of the degree of conversion after the different processing phases.

These analyses are based on the characteristic of a sufficiently long unit cell of reproducing a predominant uniaxial stress state in the central part of the specimen. This assumption is verified in the next few pages by means of simple mechanical analysis of two cylinders in parallel, using the Shear Lag

approach and finally by finite element modeling.

The strain monitoring capability is then fully exploited in terms of damage detection and damage analysis. It is shown in Chapter 8 that due to the increasing ageing process fiber matrix debonding is characterized as a function of the water concentration field.

### 2.2.1 Isostrain justification

As already mentioned the strain sensing capability of the optical fiber embedded in the SFC is used for the determination of the material properties of the bare resin. The whole analysis is based on the condition that in the central zone of the SFC a simplified stress-strain state is reproduced thanks to the slenderness of the SFC itself and to the symmetry conditions. This assumption is analyzed in details in the next few sections as function of the relative stiffness ratio of the two components: the matrix and the fiber cylinder. It is well known in fact that polymer materials properties are widely changing with temperature and humidity. This characteristic can reduce the stiffness of the matrix cylinder significantly leading the ratio between the two approaching the unity. In order to establish the stiffness range for which the validity of the approximations used is guaranteed, the influence of the resin properties on the stress-strain state in the center of the specimen is addressed using two analytical solutions and then confirmed by finite element modeling.

#### 2.2.1.1 Concentric cylinders

Considering the central of the SFC subjected to a temperature change  $\Delta T$ , and representing the associated stress-strain state by two concentric cylinders with different materials properties, the following assumptions can be made:

1. for symmetry reasons the total deformation in the matrix and in the fiber should be equal  $\varepsilon_f^{Tot} = \varepsilon_m^{Tot}$ ,
2. shear transfer along the interface is not present.

In this case, the force equilibrium of the section A-A gives:

$$\sigma_f A_f + \sigma_m A_m = 0 \quad (2.13)$$

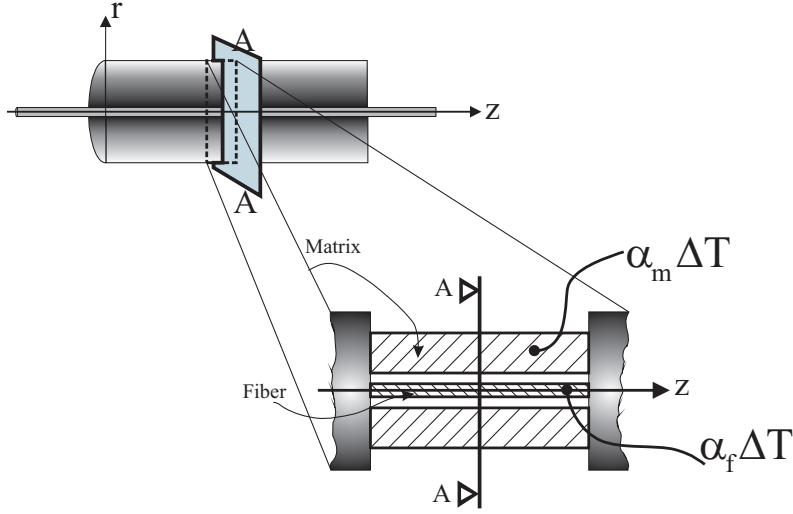


Figure 2.9: Middle plane simplification in two cylinders in parallel.

where  $A_f$  and  $A_m$  are the cross sectional areas of the fiber and matrix respectively. The elastic deformation of the matrix is given by:

$$\varepsilon_m^{el} = \varepsilon_m^{Tot} - \alpha_m \Delta T \quad (2.14)$$

similarly for the fiber:

$$\varepsilon_f^{el} = \varepsilon_f^{Tot} - \alpha_f \Delta T \quad (2.15)$$

where  $\alpha_m = 11 \times 10^{-5}$  and  $\alpha_f = 8 \times 10^{-7}$  are the coefficient of thermal expansion of the matrix and fiber respectively and a  $\Delta T = 25^\circ\text{C}$  is assumed. Substituting (2.14) and (2.15) in the Hooke's law:

$$\sigma_f = E_f (\varepsilon_f^{Tot} - \alpha_f \Delta T) \quad (2.16)$$

and for the matrix:

$$\sigma_m = E_m (\varepsilon_m^{Tot} - \alpha_m \Delta T) \quad (2.17)$$

Substituting (2.16) and (2.17) in the (2.13):

$$\varepsilon_f^{Tot} - \alpha_f \Delta T = -\frac{E_m A_m}{E_f A_f} (\varepsilon_m^{Tot} - \alpha_m \Delta T) \quad (2.18)$$

considering condition 1), i.e,  $\varepsilon_f^{Tot} = \varepsilon_m^{Tot}$  and introducing the stiffness ratio  $K$ :

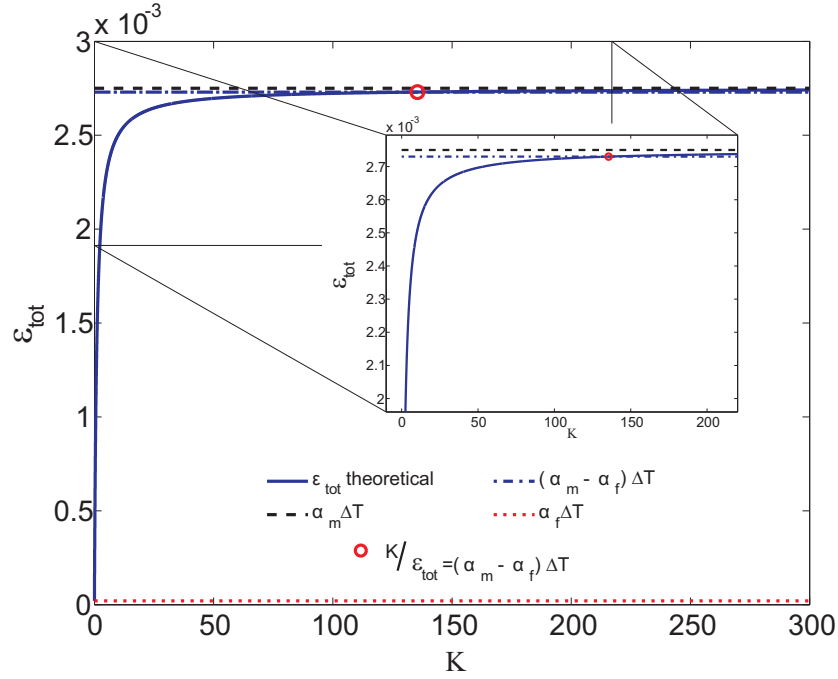


Figure 2.10: Total strain evolution as function of the cylinder's stiffness ratio.

$$K = \frac{E_m A_m}{E_f A_f} \quad (2.19)$$

the total deformation can be expressed as:

$$\varepsilon_{Tot} = (\alpha_m K + \alpha_f) \Delta T \left( \frac{1}{K + 1} \right) \quad (2.20)$$

considering fixed the geometry of the SFC cell so that  $A_m \approx 113.097 \text{mm}^2$ ,  $A_f \approx 0.012 \text{mm}^2$  and the material properties of the fiber ( $E_f = 72 \text{GPa}$  and  $\alpha_f = 8 \times 10^{-7} \text{C}^{-1}$ ), but varying, as will be clear later on, the Young's modulus of the matrix the evolution of  $\varepsilon_{Tot}(K)$  is reported in Fig. 2.10:

For high values of  $K$ , i.e, for large values of the matrix stiffness, it is clear that the deformation in the fiber and then in the matrix are approaching the value of  $\alpha_m \Delta T$ , while for  $K$  approaching zero, so for large values of the fiber stiffness, the deformation in the matrix and in the fiber approaches  $\alpha_f \Delta T$ . The difference  $\varepsilon_{Tot} - (\alpha_m - \alpha_f) \Delta T$  is reported in Fig.2.11 showing that this simplified model establishes that a ratio  $K = 90$  is required to bound the error committed by approximating the  $\varepsilon_{Tot}$  with  $(\alpha_m - \alpha_f) \Delta T$  in the order of

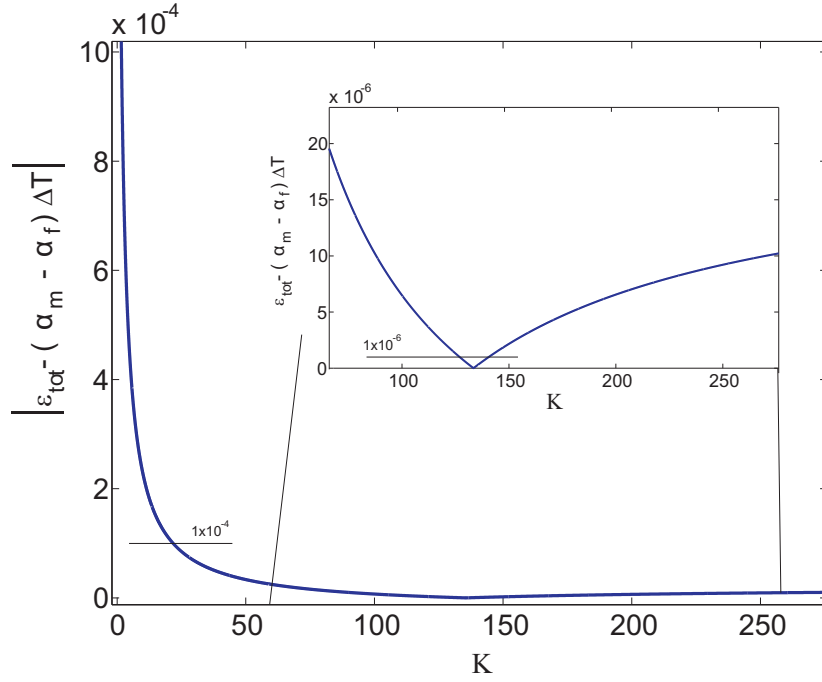


Figure 2.11: Absolute difference between total strains and  $(\alpha_m - \alpha_f)\Delta T$ .

Table 2.1: Evolution of the total deformation for the two cylinders approximation of the stress-strain state in the middle plane of the single fiber composite.

$E_m$ [MPa]	$K = \frac{E_m A_m}{E_f A_f}$	$\varepsilon_{Tot}$	$ \varepsilon_{Tot} - (\alpha_m - \alpha_f) \Delta T $
2400	307.2	$2.741 \times 10^{-3}$	$1.114 \times 10^{-5}$
1200	153.6	$2.732 \times 10^{-3}$	$2.339 \times 10^{-5}$
600	76.8	$2.715 \times 10^{-3}$	$1.509 \times 10^{-5}$
200	25.6	$2.647 \times 10^{-3}$	$0.826 \times 10^{-4}$
50	6.4	$2.381 \times 10^{-3}$	$0.348 \times 10^{-3}$

$1 \times 10^{-5}$ .

For particular values of  $E_m$  the results are summarized in Table 2.1 where the values for the Young's modulus of the matrix corresponds to the Young's modulus of the resin in the reference state, at  $50^\circ\text{C}$ , and in relaxed conditions but at different water content. The last value  $E_m = 50\text{MPa}$  has been added just as extension and for illustrative purpose.



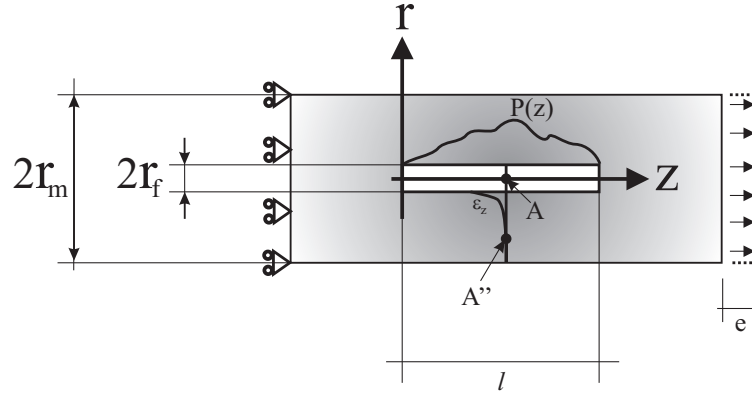


Figure 2.12: Shear Lag Model sketch, longitudinal cross section.

### 2.2.1.2 Shear lag approach

The Shear lag theory has been developed by Cox in 1952 [64] for the analysis of the strength of fibrous materials. The complete development can also be found in [65].

The loading conditions and the main hypotheses behind the model can be depicted in Fig.2.12 and summarized as follows:

1.  $u$  is the displacement of the fiber in the  $z$  direction
2.  $v$  the displacement of the matrix in the  $z$  direction
3. The matrix is strained uniformly at infinity  $\frac{\partial v}{\partial z} |_{z \rightarrow \infty} = e = const.$
4. Matrix and fiber are elastic materials
5. The increment of the load  $P$  on the fiber is proportional to the difference of the displacement of point  $A$  in the fiber and the point  $A''$  at the same  $z$  but at radius where the deformation  $\epsilon_z$  can be considered not perturbed by the presence of the fiber.

Condition (5) can be expressed as follows:

$$\frac{\partial P}{\partial z} = H(u - v) \quad (2.21)$$

where  $H$  is the proportionality constant that must be determined. Differentiating with respect to the  $z$  coordinate, the following second order differential equation governs the problem:

$$\frac{\partial^2 P}{\partial z^2} = H\left(\frac{P}{E_f A_f} - e\right) \quad (2.22)$$

whose solution is:

$$\sigma_f = E_f e \left\{ 1 - \frac{\cosh\left(\gamma\left(\frac{l}{2} - z\right)\right)}{\cosh\left(\gamma\frac{l}{2}\right)} \right\} \quad (2.23)$$

where the parameter  $\gamma$  is expressed by:

$$\gamma = \sqrt{\left\{ \frac{\pi}{(1 - \nu_m) A_m} \left(\frac{E_m A_m}{E_f A_f}\right) \left(\frac{1}{\ln\left(\frac{R^*}{r_f}\right)}\right) \right\}} \quad (2.24)$$

the corresponding solution for the shear distribution along the  $z$  direction can be determined by the equilibrium condition of a fiber element subjected to axial stress and sheared by the matrix:

$$\tau_f = E_f e \sqrt{\left(\frac{G_m}{2E_f \ln\left(\frac{R^*}{r_f}\right)}\right) \left(\frac{\sinh\left(\gamma\left(\frac{l}{2} - z\right)\right)}{\cosh\left(\gamma\frac{l}{2}\right)}\right)} \quad (2.25)$$

The parameter  $R^*$  is usually taken as a multiple of the fiber radius and depending on the materials and the relative dimensions assumes different values, however, no univocally agreement exist in literature. For this reason a parametric study in  $R^*$  is conducted and its value is clarified in section 2.2.1.3 by means of a finite element analysis.

Equations (2.23) and (2.25) are depicted in Fig. 2.13.

If, instead of a mechanical load, a temperature change is imposed, it can be demonstrated that the differential equation governing the problem is formally equal to (2.22) when  $e = (\alpha_m - \alpha_f) \Delta T$  is substituted in the equation. In this case the fiber deformation takes the form:

$$\varepsilon_f = (\alpha_m - \alpha_f) \Delta T \left\{ 1 - \frac{\cosh\left(\gamma\left(\frac{l}{2} - z\right)\right)}{\cosh\left(\gamma\frac{l}{2}\right)} \right\} \quad (2.26)$$

Similar to the case of the two concentric cylinders the deformation of the fiber is plotted as function of the stiffness ratio  $K$ , contained in the  $\gamma$  parameter, and in this case also as function of the parameter  $R^*$  (Fig.2.14). Comparing Fig.2.14

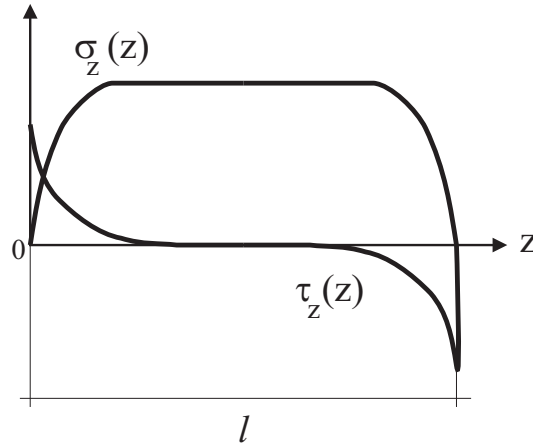


Figure 2.13: Axial and Shear Stress distribution along the  $z$  direction.

with Fig.2.10 it is clear that the fiber strains cross the level  $(\alpha_m - \alpha_f) \Delta T$  for lower values of stiffness ratios. Moreover, if the absolute difference between  $(\alpha_m - \alpha_f) \Delta T$  and the fiber strains is plotted (Fig. 2.15), it can be seen as the error, committed approximating the fiber deformation with the difference of the thermal expansion of the two components, is lower than  $1 \times 10^{-5}$  for stiffness ratios  $9 < K < 22.5$  depending of the  $R^*$ . This  $K$  range is at least one fourth smaller than the case where no shear is transferred from the matrix to the fiber, i.e, the case of the two concentric cylinders.

It must be noted that for the chosen geometry of the SFC the external matrix radius is 96 times bigger than the fiber radius. Considering  $R^* = 96r_f = r_m$  means that the whole matrix radius is affected by the influence of the fiber. The influence of the shear transmission across the interface is remarkable if compared to table 2.1 and it is beneficial in extending the validity of equation (2.12).

### 2.2.1.3 Finite Element investigation

In order to have an insight on the stress field at the middle plane of the specimen and on the entity of the parameter  $R^*$ , a parametric study of the SFC subjected to a temperature rise  $\Delta T = 25^\circ C$  has been conducted. As in the previous cases the stiffness ratio  $K$  has been varied only by reducing the Young's modulus of the matrix. The axial deformation at the middle plane of the SFC is reported in Fig. 2.16 as function of the radius. It can be seen as

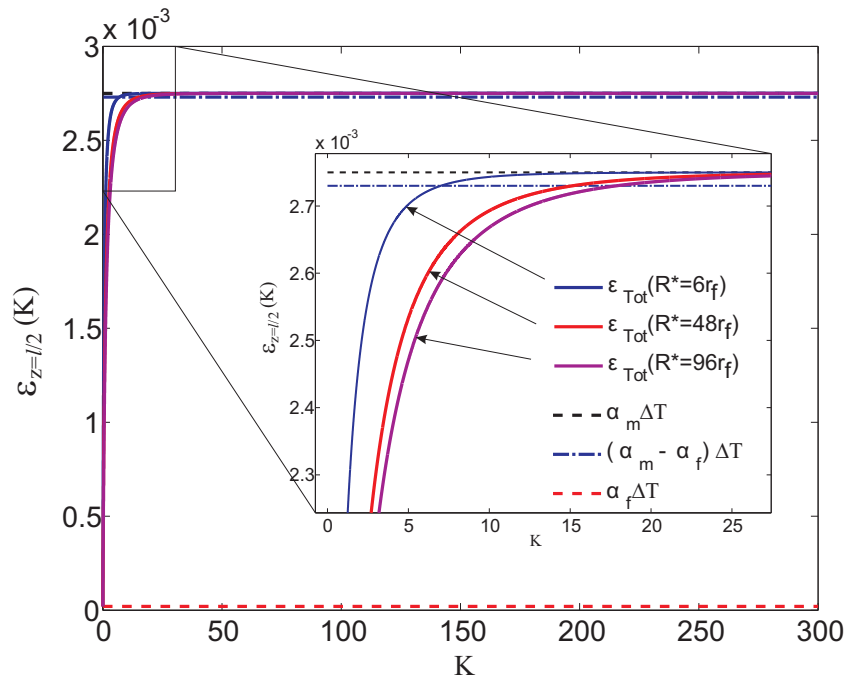


Figure 2.14: Fiber strains evolution as function of the stiffness ratio  $K$  for different values of  $R^*$ .

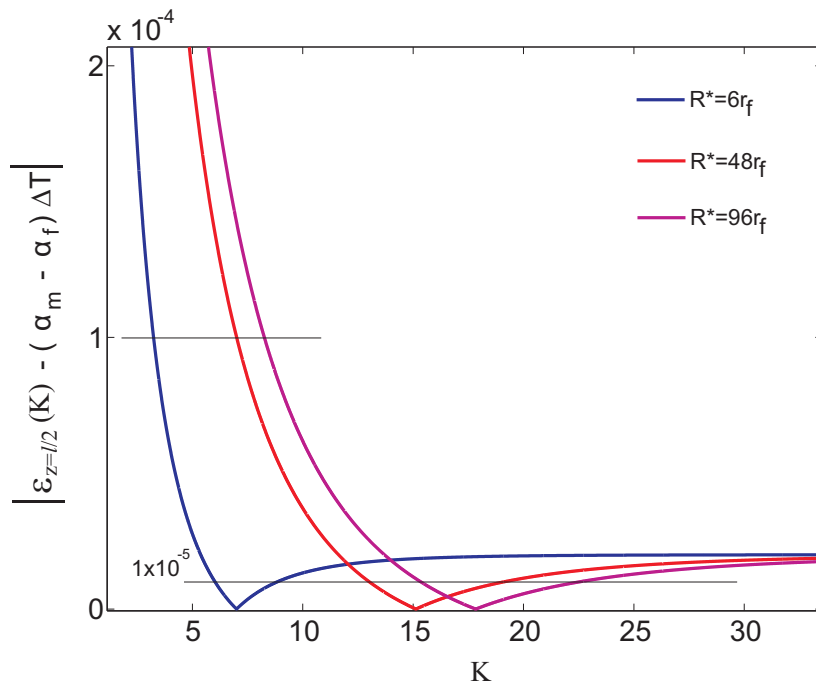


Figure 2.15: Error evolution as function of stiffness ratio  $K$  and for different values of  $R^*$ .

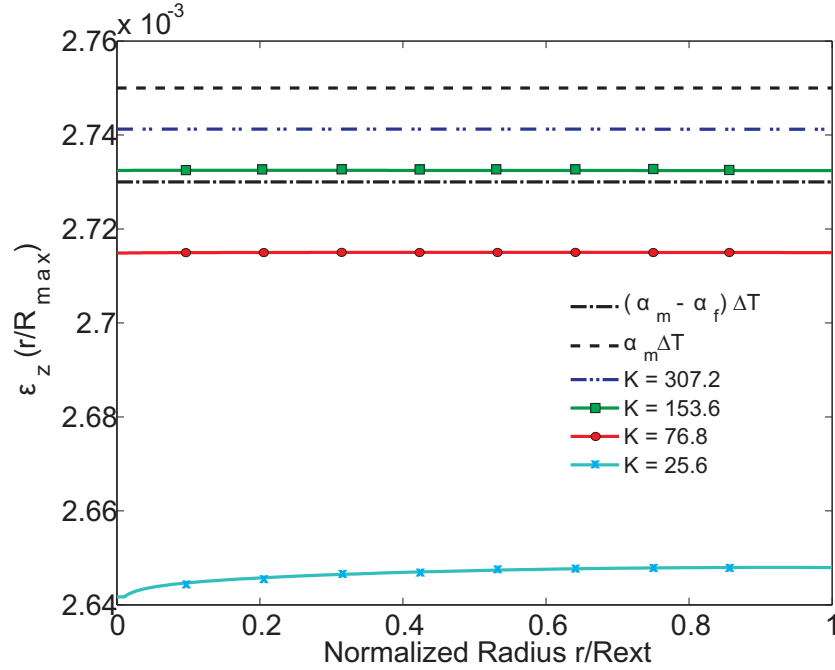


Figure 2.16: Axial deformation  $\varepsilon_z$  at  $z=20$  as function of the normalized radius.

the stiffness ratio corresponding to  $K = 25.6$  generates a noticeable variation of the axial strains along the radius. Nevertheless, the difference between the deformation on the fiber and the maximal deformation on the matrix is small in magnitude even in this case corroborating what found in the shear lag analysis. In all the other cases the influence of the presence of the fiber is not remarkable meaning that an  $R^* = r_f$  is largely sufficient to redistribute the shear variation due to the presence of the fiber. On the other hand, in the case of  $K = 25.6$ ,  $R^*$  can be evaluated to be equal to half of the radius of the matrix, i.e, corresponding to  $R^* = 48r_f$ .

It can be concluded that for  $K > 12$ , i.e, the value found from the shear lag analysis for  $R^* = 48r_f$  the error committed considering the strain on the fiber equal to  $(\alpha_m - \alpha_f)\Delta T$  is less than  $1 \times 10^{-5}$ .

A final comment is that a variation in the radius of the epoxy matrix has a quadratic influence on the stiffness ratio whereas the reduction of its Young's modulus has only a linear effect. In this case, the fixed geometry of the SFC cell reduces the problem only to the investigation on the material properties change of the matrix but care must be taken in reducing the radius of the

matrix since this parameters influences to greater extent the validity of Eq. (2.12).

## 2.3 Inverse methods

Inverse methods allow for the determination of model parameters starting from observed data that describe the behavior of the system under study during testing conditions. From a mathematical stand point the technique is often ill-conditioned meaning that the chosen mathematical representation could violate one or all the Hadamrd condition for a well-posed problem:

1. existence of the solution
2. uniqueness of the solution
3. the solution depends continuously on the data

Even if the problem result to be well-posed it can suffer from the influence of small errors in the experimental data that lead to large error in the answer [66]. To solve these issues generally the problem is reformulated including additional assumptions on the solution such as hypothesis on its derivatives leading to a smoother solution.

### 2.3.1 Mixed FEM-Experimental Identification

The Mixed FEM-experimental identification technique offers the advantage of reducing the cases in which the solution diverges since an appropriate finite element model assures that the solution respects the physics of the problem. In this case the solution is always globally convex if the input parameters are physically consistent. In order to ensure the latter point, constraints on the parameters can also be imposed.

On the other hand, the sensitivity of the parameters with respect to the verification data points is not ensured and, depending on the problem considered, it can vary by orders of magnitude. In fact, it could happen that one or few parameters dominate the global behavior of the model response, and that the influence of the others is so small not to induce appreciable changes

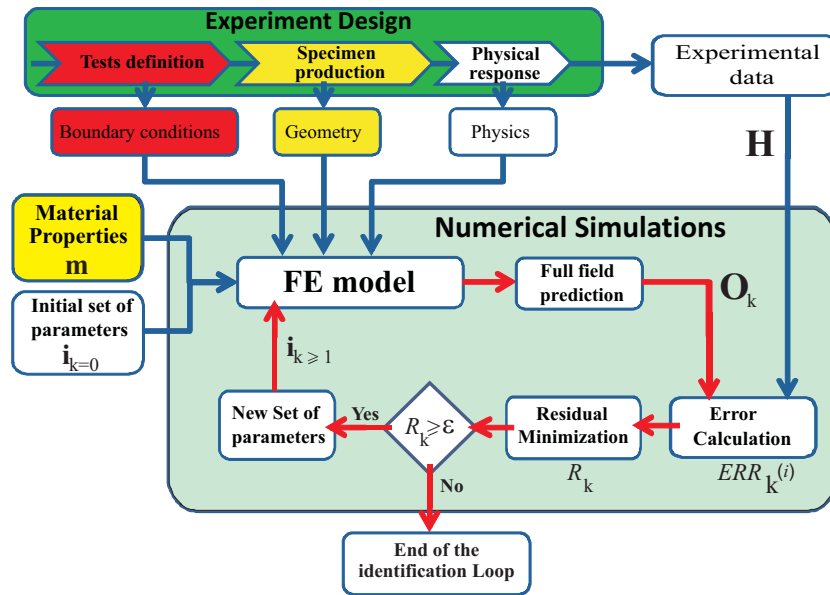


Figure 2.17: Mixed FEM-Experimental general identification scheme

in the solution. In this case, an identification in two steps is required: initially the more sensitive parameters are determined with the other fixed with an initial guess, and successively the less influent ones are determined keeping the formers fixed.

It must be highlighted that the choice of the mathematical description for the observed phenomena influences the possibility of their good reproducibility in the simulations. In particular, if the geometry of the specimen is almost always well known, the boundary conditions, imposed during the tests, are in general difficult to be reproduced accurately. Moreover, the interaction among the parameters at the basis of the physical model formulation can only be supposed *a priori*.

The general scheme of the procedure is illustrated in Fig. 2.17. It will be specialized in the forthcoming chapters as different FE models, identification parameters and the verification experimental data are considered.

Conducting an experimental test on a particular specimen generates a series of information recorded before, during and right after the testing procedure. Single point or full field observations can be arranged in the matrix  $\mathbf{H}$  of the reference data. This reference matrix can contain distributed information belonging to a particular part of the domain, its evolution in time during the

test, as well as single point evaluations of the response in time or at the end of the test. It takes the following general form:

$$\mathbf{H} = \begin{bmatrix} \mathbf{x} & \mathbf{t} & \mathbf{h} \\ (n \times m) \times 3 & (n \times m) \times 1 & (n \times m) \times 1 \end{bmatrix}$$

$$= \begin{bmatrix} \begin{pmatrix} x_1 & y_1 & z_1 \\ \dots & \dots & \dots \\ x_n & y_n & z_n \end{pmatrix} \begin{pmatrix} t_1 \\ \dots \\ t_1 \end{pmatrix} \begin{pmatrix} h(\mathbf{x}_1, t_1) \\ \dots \\ h(\mathbf{x}_n, t_1) \end{pmatrix} \\ \begin{pmatrix} x_1 & y_1 & z_1 \\ \dots & \dots & \dots \\ x_n & y_n & z_n \end{pmatrix} \begin{pmatrix} t_2 \\ \dots \\ t_2 \end{pmatrix} \begin{pmatrix} h(\mathbf{x}_1, t_2) \\ \dots \\ h(\mathbf{x}_n, t_2) \end{pmatrix} \\ \dots \\ \begin{pmatrix} x_1 & y_1 & z_1 \\ \dots & \dots & \dots \\ x_n & y_n & z_n \end{pmatrix} \begin{pmatrix} t_m \\ \dots \\ t_m \end{pmatrix} \begin{pmatrix} h(\mathbf{x}_1, t_m) \\ \dots \\ h(\mathbf{x}_n, t_m) \end{pmatrix} \end{bmatrix} \quad (2.27)$$

As indicated in (2.27) the  $\mathbf{H}$  matrix can be subdivided in 3 sub-matrices:

- The matrix  $\mathbf{t}$  contains the time of each measurement,
- the matrix  $\mathbf{h}$  the value of the measured quantities at each point and at each time
- the matrix  $\mathbf{x}$  contains the coordinates of the  $n$  positions in space where the values of the monitored quantities  $h(\mathbf{x}, \mathbf{t})$  are recorded at the  $m$  time points in  $\mathbf{t}$ .

The reference matrix  $\mathbf{H}$  will have dimensions  $(n \times m) \times 5$  and the value  $i = n \times m$  represents the total number of experimental evaluation points that are used in a given identification process. The matrix  $\mathbf{H}$  is used as term of comparison in the construction of the error vector (Eq. (2.29)).

The FE model, reproducing the geometry of the specimens, the appropriate boundary conditions and a mathematical description of the observed phenomenon, is able to predict correctly the specimen response if appropriate knowledge of the material properties is available. In most cases, only a partial knowledge of the material properties is available and thus, the objective of the identification process is to retrieve the ones that are missing. With reference



to Fig. 2.17 the vector of known material properties is called  $\mathbf{m}$  whereas the rest of the unknown material properties plus other parameters that must be identified constitute the vector  $\mathbf{i}_k$ , where the index  $k$  represent the iteration number. For the first analysis, i.e  $k = 0$ , the values contained in  $\mathbf{i}_k$  are based on appropriate guesses or on previous estimations. The vector  $\mathbf{i}$  will be continuously updated in the optimization process. In fact, after the first run, on the basis of the given  $\mathbf{m}$  and  $\mathbf{i}_0$ , the FE model calculates the pertinent fields on each point of the model. This output contains the predictions of all the quantities that were measured during the experiment which are collected in the output matrix  $\mathbf{O}_k$  that is composed by the first four columns of the matrix  $\mathbf{H}$  and, as fifth column, contains all the corresponding predictions  $o_k(\mathbf{x}, \mathbf{t})$ . For this reason  $\mathbf{O}_k$  and  $\mathbf{H}$  have the same dimensions as reported in (2.28).

$$\mathbf{O}_k = \left[ \begin{array}{ccc|ccc} \mathbf{x} & \mathbf{t} & \mathbf{o}_k & & & & \\ \hline & & & & & & \end{array} \right] = \left[ \begin{array}{ccc|ccc} \left( \begin{array}{ccc} x_1 & y_1 & z_1 \\ \dots & \dots & \dots \\ x_n & y_n & z_n \end{array} \right) & \left( \begin{array}{c} t_1 \\ \dots \\ t_1 \end{array} \right) & \left( \begin{array}{c} o_k(x_1, t_1) \\ \dots \\ o_k(x_n, t_1) \end{array} \right) \\ \left( \begin{array}{ccc} x_1 & y_1 & z_1 \\ \dots & \dots & \dots \\ x_n & y_n & z_n \end{array} \right) & \left( \begin{array}{c} t_2 \\ \dots \\ t_2 \end{array} \right) & \left( \begin{array}{c} o_k(x_1, t_2) \\ \dots \\ o_k(x_n, t_2) \end{array} \right) \\ \dots & \dots & \dots \\ \left( \begin{array}{ccc} x_1 & y_1 & z_1 \\ \dots & \dots & \dots \\ x_n & y_n & z_n \end{array} \right) & \left( \begin{array}{c} t_m \\ \dots \\ t_m \end{array} \right) & \left( \begin{array}{c} o_k(x_1, t_m) \\ \dots \\ o_k(x_n, t_m) \end{array} \right) \end{array} \right] \quad (2.28)$$

The error committed at each iteration and for each evaluation points is then determined as the ratio between the difference of the fifth column of the matrix  $\mathbf{H}$  and  $\mathbf{O}_k$  and the average over all the experimental points:

$$ERR_{k=0}(i) = \frac{\mathbf{O}_{k=0}(i, 5) - \mathbf{H}(i, 5)}{\langle \mathbf{H}(i, 5) \rangle} \quad (2.29)$$

The sum of the squares of the committed errors, called residual, for the given vector of initial parameters  $\mathbf{i}_0$  is defined as:

$$R_{k=0} = \sqrt{\sum (ERR_{k=0}(i))^2} \quad (2.30)$$

A new set of parameters  $\mathbf{i}_{k=1}$  is proposed by means of the minimization of the residual using the Leveberg-Marquard algorithm already implement in Matlab<sup>©</sup>. Subsequently the simulation is rerun with  $\mathbf{m}$  and  $\mathbf{i}_k$  as input up until the point the  $R_k$  is found to be less then, or equal to, a specified value colled identification tolerance  $\epsilon$ . In general, 0.1% of error is accepted leading to  $\epsilon = 0.001$ . If this condition is met the identification loop is terminated and the identified parameters are contained in the last  $\mathbf{i}_k$  vector.

# Chapter 3

## Specimen preparation

In this chapter the materials used in the fabrication process are presented as well as details regarding the processing itself and the final geometries of the specimens produced.

### 3.1 Materials and specimen preparation

The epoxy under investigation is a mixture of two resins DER330<sup>©</sup>, DER732<sup>©</sup> and the hardener DEH26<sup>©</sup> provided by the DOW chemical company. This mixture, in fixed weight proportion of 70 : 30 : 10, respectively, is stirred in vacuum in order to eliminate the presence of bubbles.

The DER330 is a low viscosity Bisphenol-A based epoxy resin which is stiffer with respect to the DER732. The latter is a long chain molecule polyglycol di-epoxide resin. The hardener DEH 26 is a general purpose room temperature curing agent based on Tetraethylenepentamine (TEPA).

Two types of specimens are produced: cylindrical ones with centrally located optical fibers (i.e, single fiber composite (SFC) and cylindrical dog-bone like specimens (DGB). The mixture is casted into the respective moulds (Fig.3.1) which have been previously treated with the mould release agent Frekote 770.

The curing step is then performed at 30°C for 24 hours, in an oven. Afterwards, the specimens are removed from their moulds in order to avoid the formation of high level of residual strains in the postcuring phase. The latter phase is composed by a ramp in temperature of 0.5°C/min up to 70°C where

a dwell of 9 hours is imposed. Subsequently the specimens are allowed to cool in the oven until room temperature is reached (Fig.3.2).

Lastly, a drying phase is imposed to ensure complete dryness of specimens before water immersion. The drying temperature is taken at 50°C, equal to the temperature of the ageing bath and lasts one week. During this time weight measurements are carried out periodically in order to verify that after 7 days no weight loss is discernible.

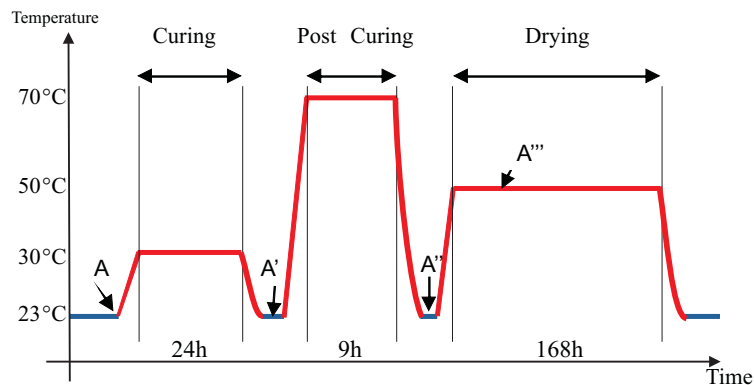
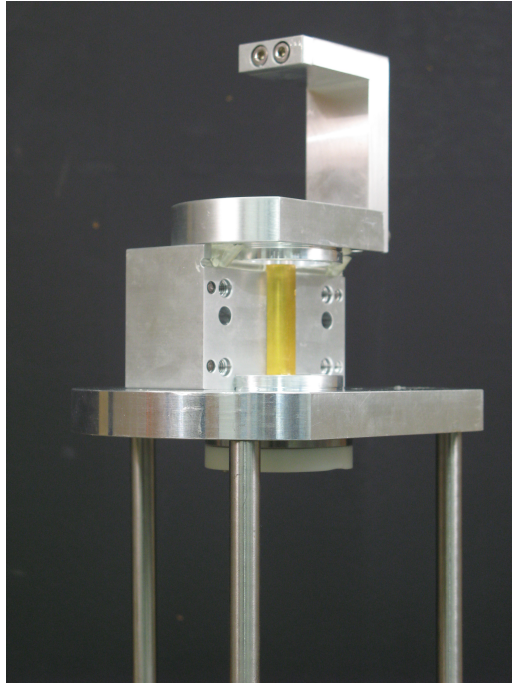


Figure 3.2: Specimens' thermal treatments.

## 3.2 Specimens' geometries

A schematic of the single fiber composite is reported in Fig.3.3. The epoxy cylinder is 12mm in diameter and 40mm long. The optical fiber has been stripped of its coating along the FBG sensor in such a way that the uncoated part extends few millimeters beyond the sensor's extremities in order not to influence the deformation field. The sensor position, with respect to the specimen's edge, has been chosen in such a way to keep a part of it outside of the specimen itself and the remaining part still able to reach the middle plane of the cylinder. This particular positioning provides the capability of monitoring temperature during the measurement since the external part of the grating senses only thermal strains. In the following, the system of coordinates reported in Fig.3.3 is used. The specimen is considered symmetric with respect to the middle plane since the remaining coated part on the right side of the optical fiber is considered not to have a strong influence on the stress-strain state of the region. Concerning the dogbone specimens a technical drawing is



(a)



(b)

Figure 3.1: (a) Single fiber specimen vertical mould, (b) dogbone mould.

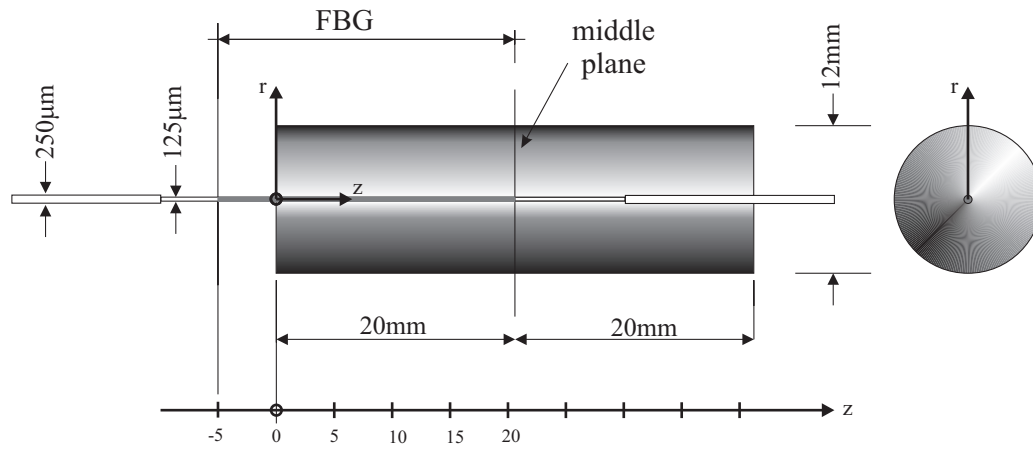


Figure 3.3: Single Fiber Composite scheme.

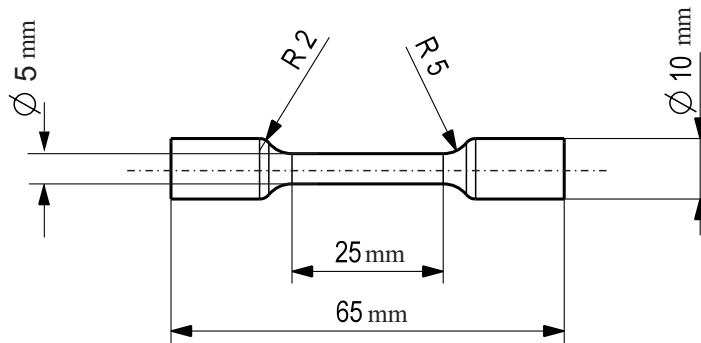


Figure 3.4: Dogbone specimen technical drawing.

reported in Fig. 3.4.

# Chapter 4

## Resin consolidation analysis

During processing the resin undergoes radical chemico-physical changes. In fact, the crosslinking process increases the viscosity of the resin that, solidifying, shrinks and reduces its volume. The kinetic of the reaction can be described in terms of degree of cure that, ranging from 0, not reacted resin, to 1, fully reacted resin, identifies the completeness of the reaction.

During the chemical process, the resin thermo-mechanical properties evolve continuously. In particular, the elastic properties increase as the chains mobility decreases. As result of this complex evolution and of the interaction with the mould, residual deformation is generated and stored at ambient temperature during the cooling process.

In this chapter, the degree of cure for the resin under investigation is calculated taking advantage of the correspondence between its progression and the resin volume reduction. The resin coefficient of thermal expansion in the after postcuring conditions is also determined.

Finally, the developed methodology is validated in the case of micro- and nano-particles reinforced epoxy.<sup>1</sup>

---

<sup>1</sup>The latter section is the result of a fruitful collaboration with Institute for Composite Materials (IVW GmbH), Technical University of Kaiserslautern, and in particular with prof. Klaus Friedrich, whose help and guidance are gratefully acknowledged.

## 4.1 Degree of curing determination

The FBG sensor embedded in the SFC cell allows for monitoring the deformation induced on the fiber by the volumetric shrinkage of the matrix. Considering an infinitesimal cube of epoxy subjected to a uniform contraction the change in volume is associated to the applied deformation as follows [67]:

$$\Delta\varepsilon = \sqrt[3]{\frac{\Delta V}{V_0} + 1} - 1 \quad (4.1)$$

where  $\Delta V$  is the change in volume and  $V_0$  is the initial volume of uncured material. The progressive change in volume is supposed to be proportional to the total volume reduction at full cure,  $V_{tot}$ , by means of the degree of cure  $\Delta\gamma$  [68]:

$$\Delta V = \Delta\gamma V_{tot} \quad (4.2)$$

Moreover, the resin used in this work is a low shrinkage resin. For such a material, the range of relative volumetric change  $\left(\frac{\Delta V}{V_0}\right)_{max}$  is typically 1 – 3% [67]. Therefore, in this small range of variation, Eq.(4.1) can be developed in Taylor series leading to:

$$\Delta\varepsilon = \sqrt[3]{\frac{\Delta V}{V_0} + 1} - 1 \simeq \frac{1}{3} \frac{\Delta\gamma V_{tot}}{V_0} \quad (4.3)$$

Assuming the following relationship to hold  $\left(\frac{\Delta V}{V_0}\right)_{max} = \frac{V_{tot}}{V_0} = 2.4\%$ , a linear relationship between the deformation and the degree of curing is established:

$$\varepsilon^{chem} = \alpha_{chem} \Delta\gamma \quad (4.4)$$

where  $\alpha_{chem} \approx \frac{1}{3} \frac{V_{tot}}{V_0} = 0.008$ . Note that Eq.(4.4) is associated with the 2<sup>nd</sup> term in Eq.(2.12) [69]. Measuring the evolution of the deformation, as the processing cycle progresses, leads to the determination of the degree of curing.

With reference to Fig.3.2, reported in section 3.1, three points during processing are identified. Point A, corresponds to the before-casting conditions, Point A', after the curing phase and Point A'' in after post-curing conditions. In each of those conditions the local Bragg wavelength is recorded and reported in Fig.4.1.



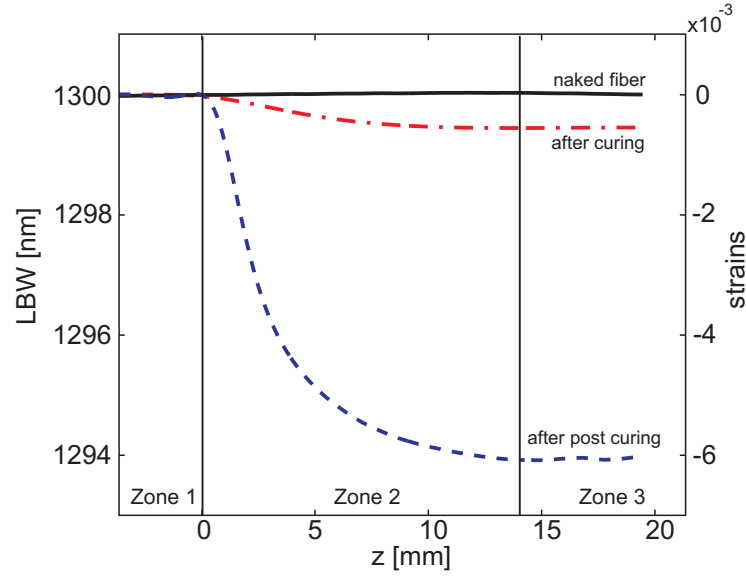


Figure 4.1: Residual strains evolution during processing.

Point A provides the reference local Bragg distribution along the grating (naked fiber), whereas the following measurements establish the progression of the cure process. On the right hand side axis of Fig.4.1, the conversion from wavelengths to strains is reported using Eq.(2.11), where the temperature dependent term is not taken into account since all these measurements are conducted at room temperature. Notice also that along  $z$  three zones can also be distinguished:

- Zone 1 corresponds to the part of the grating that is outside of the specimen,
- Zone 2 where a strain gradient is present due to the presence of the specimen edge,
- Zone 3 where the afore mentioned isostrain condition holds.

Considering the latter region, Eq.(2.12) can be used. In particular, the only term that plays a role is the one related to the chemical shrinkage:

$$\frac{\lambda_{B1} - \lambda_{B0}}{\lambda_{B0}} = (1 - p_e) \alpha_{chem} \Delta\gamma \quad (4.5)$$

As stated earlier, the reference wavelength  $\lambda_{B0}$  is determined considering the curve  $\lambda_B(z)$  in the zone 3, i.e for  $z = 19mm$ . On the other hand, the  $\lambda_{B1}$  used

Table 4.1: Evolution of the degree of conversion with the progression of the processing cycle.

	SFC1	SFC2
position	$\Delta\gamma$ [%]	$\Delta\gamma$ [%]
A'	7.14	3.89
A''	73.72	70.78

for the after-curing and after-postcuring conditions is calculated by means of their corresponding curves at the same  $z$ . The degree of cure  $\Delta\gamma$  is then easily calculated from Eq.(4.5) and the results are reported in Table 4.1. It can be noticed that, for both the specimens tested, the degree of cure in after postcuring condition is very reproducible and consistent with other findings for similar materials [70]. In contrast a difference of  $\sim 50\%$  is noticed in the after curing condition. The discrepancy is believed to be due to some difficulties in starting the polymerization at the beginning of the curing step because of its relatively low temperature plateau. This analysis is corroborated by the fact that, after post-curing, the resin exhibits the same degree of cure for both the samples.

## 4.2 Determination of the coefficient of thermal expansion

A procedure similar to the one described in section 4.1 is used for the determination of the coefficient of thermal expansion. In particular, the points A'' and A''' in Fig.3.2 are taken into consideration. Note that in the point A''' the specimen is assumed to be in isothermal conditions. The time necessary for this condition to be established has been evaluated using a FE transient heat model. Natural convection is applied on the specimen external surface and the material properties of the resin has been selected in such a way that the calculated equilibrium time is a conservative estimation. The equilibrium temperature is reached after 3 hours, since the beginning of the drying phase, the latest. It is assumed that, since the drying phase takes place at  $50^\circ\text{C}$ , no additional curing is possible during this step making possible to attribute every wavelength change in zone 3 only to the thermal expansion of the resin.

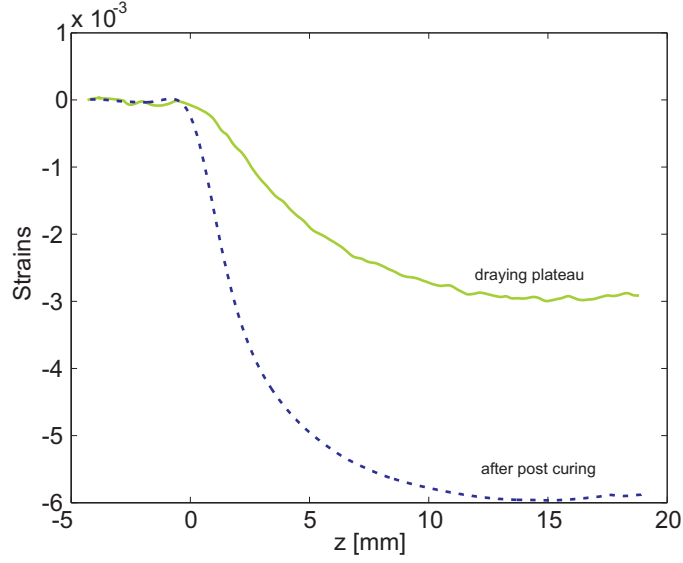


Figure 4.2: fiber strains after post curing and at drying plateau after thermal equilibrium.

Table 4.2: Resin coefficient of thermal expansion.

CTE		
	SFC1	SFC2
23-50°C	$11.61 \times 10^{-5}$	$11.00 \times 10^{-5}$

The evolution of strains obtained using Eq.2.11 is reported in Fig.4.2. Note that LBW are not plotted this time because of the vertical shift imposed in the conversion between the two scales by the term  $(\alpha_f + \xi) \Delta T$  in Eq.2.11 making impossible to represent both quantities in the same figure.

Considering the wavelength in zone 3, as explained in the previous section, the Eq. 2.12 is used to determine the coefficient of thermal expansion of the resin  $\alpha_m$ . In fact, the latter equation, reduces to:

$$\frac{\lambda_{B1} - \lambda_{B0}}{\lambda_{B0}} = (1 - p_e) (\alpha_m - \alpha_f) \Delta T + (\alpha_f + \xi) \Delta T \quad (4.6)$$

where  $\lambda_{B1}$  is taken from the curve at 50°C ( $z = 19mm$ ),  $\lambda_{B0}$  is, in this case, the wavelength at the same location but belonging to the after postcuring curve. Therefore, in Eq. 4.6 everything is known except  $\alpha_m$  that can be easily calculated. The results for two specimens are reported in Table 4.2 showing very good reproducibility with a maximum difference from the average of 2.7%.

### 4.3 Application: Epoxy resin reinforced with micro and nanoparticles <sup>2</sup>

The method presented in Section 4.2 is used to measure the CTE of a series of epoxy reinforced with different micro and nano-particles. The main motivation that led to this work has its root on the necessity of improving the fracture toughness of epoxies which, especially in the highly cross-linked version, are very fragile. In this frame, the addition of second phases of rubber particles has been found to lead to a remarkable increases of fracture toughness. On the other hand, this improvement is accompanied by a significant loss in elastic modulus, strength and glass transition temperature. The addition of a third rigid phase has been indicated as the best compromise between good material properties and excellent toughness.

From an industrial stand point, it is of vital importance to understand how the addition of these fillers influences the processing and thermal behavior of such composites. In particular, this section addresses the change in the coefficient of thermal expansion as well as the different residual stresses development associated to different fillers contents introduced in the neat resin.

The three materials used in this study are:

1. *CeTePox VP 823-30R*, neat epoxy resin (EP), delivered by Chemicals and Technologies for Polymers GmbH [26].
2. *CeTePox VP 823-33R*: This master batch epoxy resin is a suspension containing  $SiO_2$  nanoparticles (Chemicals and Technologies for Polymers GmbH). The dispersed phase consists of surface-modified, spherical nano- $SiO_2$  with diameters under 50nm and an extremely narrow particle size distribution, obtained from a sol-gel chemical process.
3. *Albidur EP 2240 A*: Master batch epoxy resin, modified with reactive silicone rubber (SR) micro-particles by Nanoresins GmbH. The elastomer fraction is a special silicon rubber addition with a particle size of 0.1–3 $\mu$ m, finely distributed as a separate phase in the liquid resin.

---

<sup>2</sup>In this section relevant parts of the article “*Evaluation of residual strains in epoxy with different nano/micro-fillers using embedded fiber Bragg grating sensor*” published in 2010 in the journal “Composites Science and Technology” are reported.

Nanocomposites and hybrid compounds, with variable content of ceramic and rubber, were produced by dilution or mixing/dilution of the corresponding master batches with neat epoxy. The compositions of the mixtures are shown in Table 4.3.

Table 4.3: Compositions of the nanocomposites and hybrid compounds in vol.%, and their designations.

<i>Siliconrubber</i>	<i>Nano – SiO<sub>2</sub></i>		
	0	3	8
0	0_0	0_3	0_8
3	3_0	3_3	3_8
5.5	5.5_0	5.5_3	

The mixtures were prepared using a dissolver (Wilhelm Niemann GmbH, Germany), operating at 200 rpm, 60°C and vacuum during 1h and finally casted in moulds identical to the one reported in Fig.3.1(a). Optical fibers with long FBG were positioned as shown in Fig.3.3.

After the curing program (Fig.4.3), OLCR measurements were conducted allowing to highlight the differences in the development of residual deformation. For each particle content the fiber deformation as function of the position is reported in Fig.4.4. It can be noted that the introduction of rubber particle generates a reduction of the residual strains developed with respect to the neat resin. Moreover, every attempt to produce samples with *SiO<sub>2</sub>* particles as only reinforcement produced a very weak interface. In fact, every specimens with these configurations showed extensive debonding towards the end of the FBG sensor. However a remarkable increase of deformation can be suspected by comparing the curve relative to the specimen 0\_8 and the one with neat resin.

The intact samples were then subjected to a successive thermal cycle, depicted in Fig.4.5, composed of a series of two similar heating profiles, themselves consisting of four temperature plateaus with: P1 = 31.5°C, P2 = 39°C, P3 = 48°C and P4 = 58°C, with a maximum oscillation of  $\pm 0.3^\circ\text{C}$ . The range of these temperatures was chosen so that the highest temperature was below the glass transition temperature of the epoxy and an identical second cycle is carried out to verify that effectively no additional curing has occurred.

The temperature was recorded, during the whole test, using K-type thermocouples placed underneath the specimens, in direct contact with them. Once

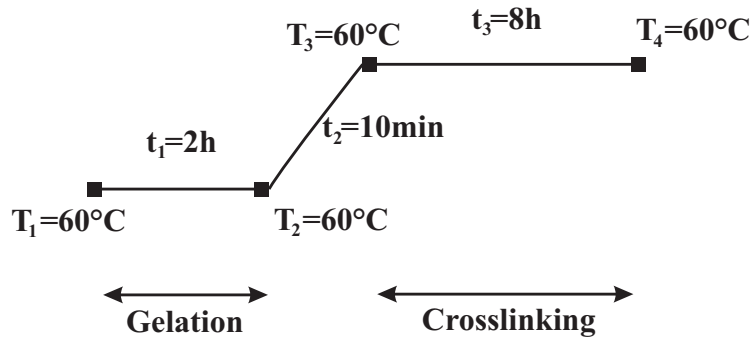


Figure 4.3: Curing program for epoxy and the modified compounds.

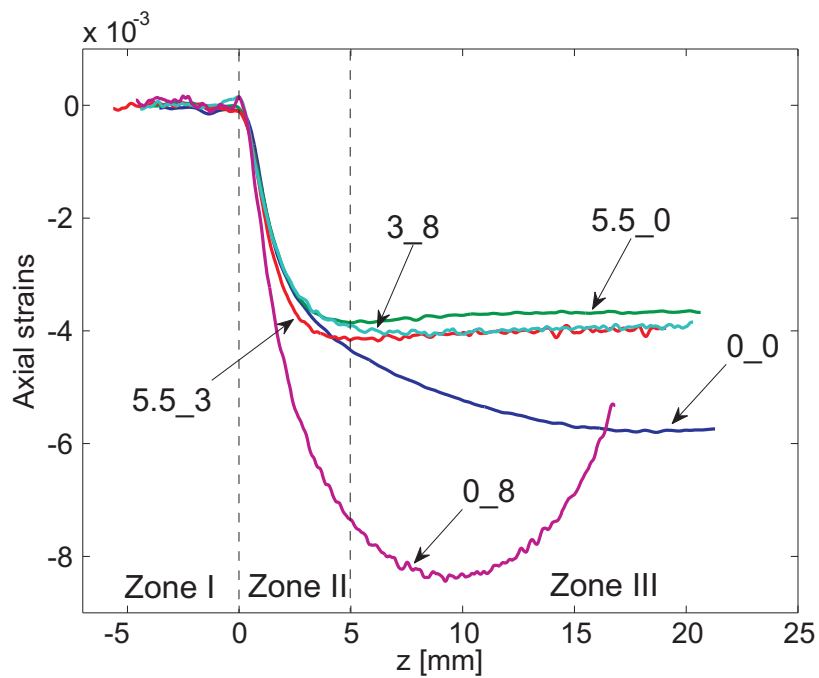


Figure 4.4: Residual strains evolution as function of the axial coordinate  $z$  for different filler content and type.

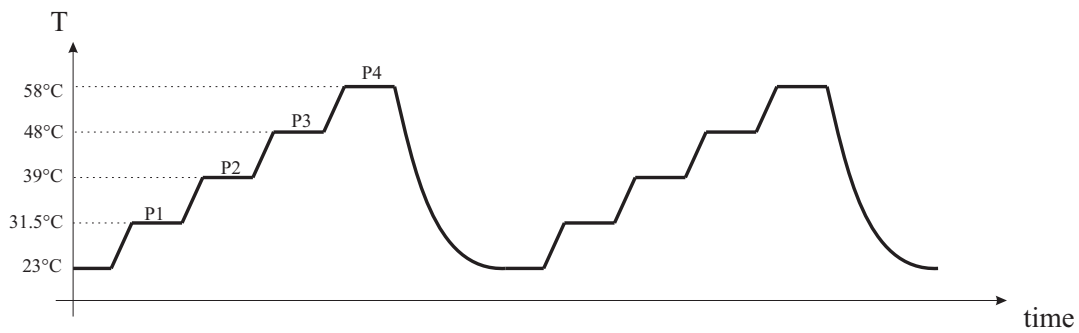


Figure 4.5: Thermal cycle for CTE measurement.

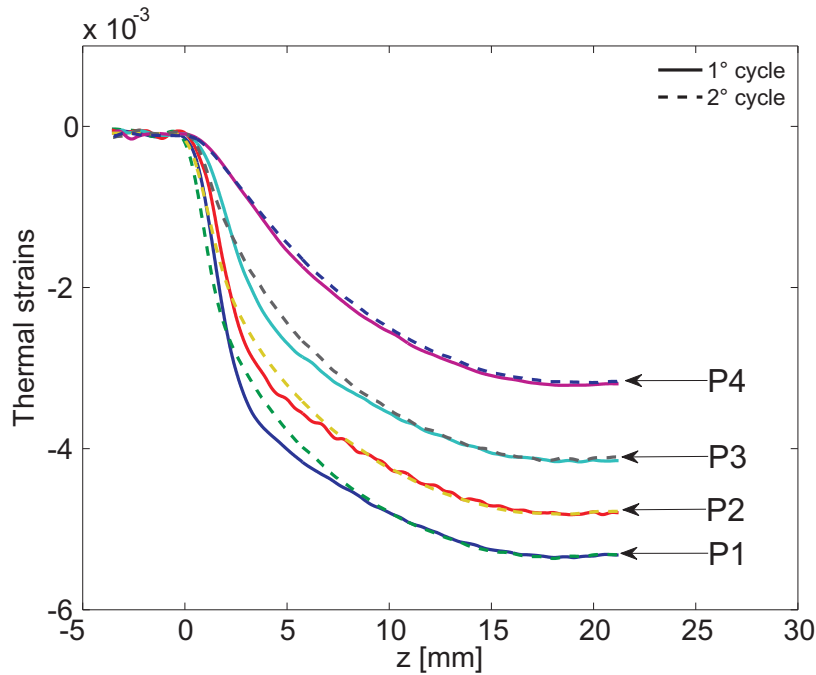


Figure 4.6: Thermal strains at different temperature for the 0\_0 configuration.

the temperature in the furnace was stabilized at each plateau, the specimens were allowed to reach equilibrium for more than 1h. Afterwards, at least five OLCR measurements were recorded at each temperature. An example of the fiber deformation recorded for one of the samples is reported in Fig. 4.6. It can be noticed that the deformation recorded in the second run is indeed identical to the one recorded in the first run allowing to verify the adopted assumptions.

Using a similar procedure as in Section 4.2, zone 3 of each specimen is considered thus  $\lambda_{B1}$  belongs to the curve at each temperature dwell  $P_i$  ( $i = 1, \dots, 4$ ) and the reference wavelength,  $\lambda_{B0}$ , corresponds to the curve belonging to the temperature plateau immediately below. Using Eq.4.6 the incremental thermal strains can be calculated and are plotted in Fig.4.7 as function of the temperature. The slope of the lines represents the CTE of the matrix for each fillers composition.

The results are summarized in Table 4.4 where are also reported the CTEs determined independently by TMA analysis on small beams of the same materials. The results indicate that, for the range of temperatures investigated, the composites behave linearly and that the influence of the fillers is small. These

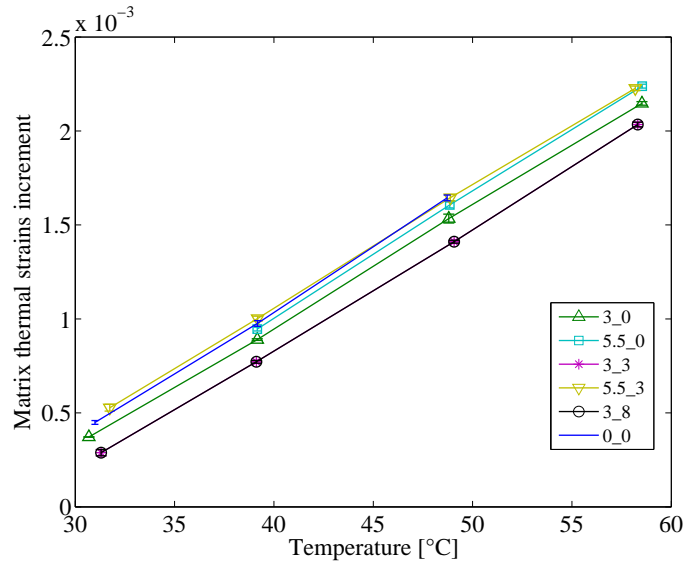


Figure 4.7: Incremental thermal strains for all available fillers compositions.

Table 4.4: Coefficients of thermal expansion for all the materials considered.

	CTE $\times 10^{-5} \text{ } ^\circ\text{C}^{-1}$		Nano-SiO <sub>2</sub>					
			0		3		8	
			OLCR	TMA	OLCR	TMA	OLCR	TMA
silicon rubber	0		6.74	6.12	/	5.85	/	6.00
	3		6.38	6.73	6.46	6.58	6.46	6.70
	5.5		6.67	6.79	6.43	7.45	/	/

results are globally confirmed by both methods used herein. The introduction of  $\text{SiO}_2$  and or silicon rubber particles results in practically no changes in the CTE. The changes in the TMA results are attributed to the method itself since the TMA strain-temperature data did not follow a straight line.



# Chapter 5

## Water diffusion analysis

This chapter is dedicated in first place to the basic physics of diffusion and its experimental characterization. Second, the data retrieved are used in the last section to determine the diffusion parameters that best represent the global behavior of the system under study.

### 5.1 Theory of diffusion

According to Crack [71] “diffusion is the process by which matter is transported from one part of a system to another as a result of random molecular motions” . In organic solids in general, and in polymeric materials in particular, this process is governed by concentration gradient (Fickian diffusion) and by the chemical potential gradient [72]. The former driving force is the prime responsible of the diffusion process when no interaction between the diffusant and the medium is established. Conversely, as generally happens in polymers, a more or less pronounced interaction of the penetrant with the polymer intra- and inter-chain bonds generates the necessity of introducing the chemical potential in order to describe correctly the diffusion mechanisms. However, in the current practice, the use of this latter more refined method of describing the diffusion process is left aside as long as the deviation from the Fickian diffusion is small. Furthermore, when important discrepancies are evident in the absorption behavior, when compared to the expected pure Fickian representation, modifications on the diffusion law are introduced. In most of the cases the diffusion coefficient is not considered constant and a dependency on

the concentration itself [73, 74] or on the applied stress is imposed [75]. This phenomenological representation of the diffusion law is able to well reconstruct the global “anomalous” absorption behavior, i.e., the absorption curve, independently of the causes that generated it. A deeper understanding of the chemical interactions that take place at the molecular level is out of the scope of this work since a macroscopic description is looked for. Nevertheless, a brief survey of the factors influencing the diffusion process is presented.

Numerous studies are available in literature on the possible epoxy-water interactions. The preferred tools of analysis are Nuclear Magnetic Resonance (NMR) spectroscopy [76, 77], Fourier Transform Infrared (FTIR) spectroscopy [78–81], X-ray Photoelectron Spectroscopy (XPS) [82], Dielectric Relaxation Spectroscopy (DRS) [81].

The NMR spectroscopy is used to identify types of chemical bonds since the width of the absorption peaks is linked to the strength of the bonding. Jelinsky et al. [76] found that there is no evidence of water free to move in the polymeric network, a result that is in agreement with the findings of Zhou [77]. Furthermore, the two authors disagree on the possibility that the water can establish strong links and that it can play an active role in disrupting the interchain hydrogen bonds. In particular, Zhou supported the assumption that two types of bonding can be established: Type I bonding, having lower energy, brakes the interchain Van der Waals links, whereas type II, requiring higher activation energy, plays the role of a “pseudo-cross linking agent” since multiple hydrogen bonds are established. With similar objectives, the FTIR spectroscopy links the evolution of absorbance spectrum during the water diffusion to the type of bonding between water and polymer. Mijovic et al. [81], reported the development of three type of bonding  $S_0$ ,  $S_1$ ,  $S_2$ , where the subscript indicates the number of hydrogen atoms participating in the bond. They also reported the possibility that the oxygen in the water could establish direct interaction with the polymer backbone. The quantitative XPS analysis, reported for instance in [82], allowed the authors to address the problem of the degradation of the polymer network by progressive hydrolysis and leaching out of part of the polymer segments.

At the macroscopic level, analysis of the absorption behavior has let Apicella et al. [83] to propose three different absorption modes: i) bulk dissolution

of water in the polymer network, ii) moisture absorption in the free space of the glass structure, iii) hydrogen bonding between polymer hydrophilic groups and water.

It is clear that a unique consensus cannot be found on the influence that water has on polymeric materials. However, the reported discrepancies can be attributed to the wide range of the epoxies used, the type of hardeners, relative weight percents, types of thermal treatments used during the preparation, etc..

For all these reasons, each degradation action, produced by water absorption, is particular to the system under study and can produce various effects at a mechanical, thermal or physical level.

In order to characterize the hygrothermal ageing of polymer based materials, the kinetic of the diffusion, treated in this chapter, the influence of the water content on the materials properties and the variation of physical properties, like the glass transition temperature (and thus its repercussions on the chosen mechanical model) must be addressed.

In this chapter a concentration dependent diffusion is considered because of its capability to reproduce the recorded behavior in a very accurate manner. Firstly the mathematical description is recalled, secondly the identification of the parameters involved is conducted.

## 5.2 Fick's law of diffusion

The analogy between heat transfer and mass diffusion was first recognized by Fick (1855) who adopted the mathematical description made by Fourier to describe the phenomenon. The basic assumption is that the rate of transfer of the diffusing substance through the unit area of a section is proportional to the concentration gradient measured normal to that section. This statement is known as the Fick's first law of diffusion:

$$J = -D \frac{\partial c}{\partial x} \quad (5.1)$$

where  $J$  is the flux across a surface perpendicular to the  $x$  direction,  $D$  is the diffusion coefficient and  $c$  is the concentration. The rate of increase of concentration is given by:

$$\frac{\partial c}{\partial t} = \frac{\partial}{\partial x} \left( D \frac{\partial c}{\partial x} \right) \quad (5.2)$$

known as the Fick's second law of diffusion. If  $D$  is constant during the diffusion process it can be taken out from the derivative sign of Eq.(5.2) simplifying the expression. The maximum achievable concentration supported by the solid, called also saturation point since it represents the equilibrium concentration at infinite time, it is introduced by the definition of normalized concentration:

$$c^* = \frac{c}{s} \quad (5.3)$$

Replacing Eq.(5.3) in Eq.(5.2) and extending in three dimensions the Fick's second law of diffusion for isotropic material assumes the following form:

$$\frac{\partial c^*}{\partial t} = \frac{\partial}{\partial x} \left( D \frac{\partial c^*}{\partial x} \right) + \frac{\partial}{\partial y} \left( D \frac{\partial c^*}{\partial y} \right) + \frac{\partial}{\partial z} \left( D \frac{\partial c^*}{\partial z} \right) = \text{div} (D \text{grad} c^*) \quad (5.4)$$

The process of diffusion is then fully characterized by two parameters: the diffusion coefficient  $D$  and the saturation point  $s$ . Both parameters have a strong temperature dependence following an equation of Arrhenius type [3]:

$$D = D_0 e^{-\frac{E_D}{RT}} \quad (5.5)$$

$$s = s_0 e^{-\frac{E_s}{RT}} \quad (5.6)$$

where  $E_D$  and  $E_s$  are the activation energies,  $T$  is the temperature in Kelvin and  $R = 8.314 \frac{\text{Joule}}{\text{Mole}\cdot\text{K}}$  is the universal gas constant. In this case 4 more parameters must be determined experimentally.

It has also been reported by Rogers in [3] that the coefficient of diffusion is dependent on the concentration. Usually this dependency is found to be linear. Therefore the diffusion process is controlled by three parameters: the diffusivity at zero concentration  $D(c^* = 0) = D_1$ , the diffusivity at saturation  $D(c^* = 1) = D_2$ , and the saturation level.

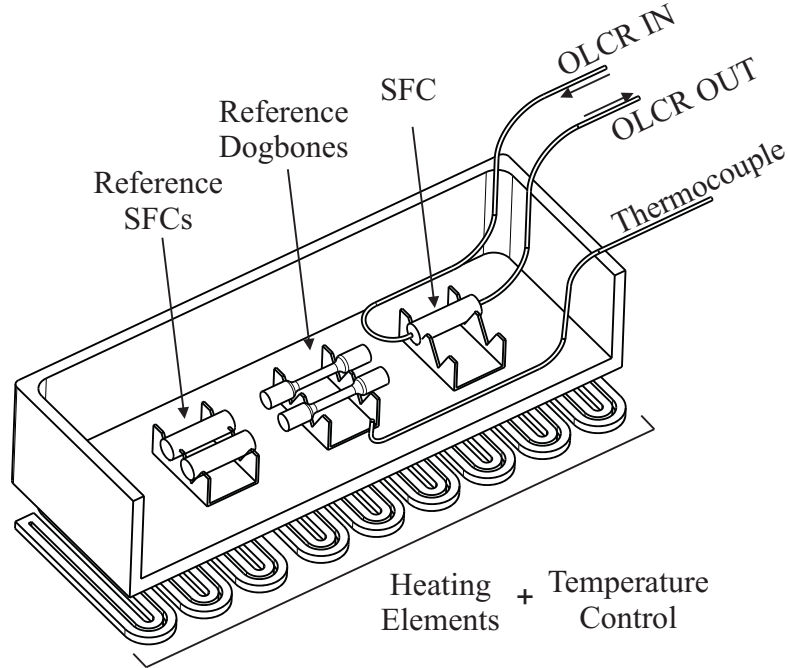


Figure 5.1: Ageing setup.

### 5.3 Experimental characterization

The specimens are immersed in a bath of deionized water constantly kept at  $50^{\circ}\text{C}\pm 0.5^{\circ}\text{C}$  using a heating element placed in contact with the bottom surface of the container. The ageing setup is depicted in Fig.5.1 where SFC cells are monitored using the OLCR apparatus and reference specimens of the same geometry, having a bare optical fiber embedded on their axes, are used to monitor the evolution of the absorbed water. Moreover, dogbone specimens are also aged with same procedure and their evolution of weight is also recorded.

The experimental characterization of the parameters governing the diffusion process requires the record of the absorption curve. The absorption curve is defined as the evolution in time of weight gained by the material. The weight gain is expressed as follows:

$$w_g(t) = \frac{w(t) - w_d}{w_d} \quad (5.7)$$

where  $w_d$  is specimen's weight at the dry state and  $w(t)$  is its weight at time  $t$ .

In the present study 3 SFC unit cells and 5 dogbones specimens were im-

mersed in water, periodically removed from the bath, wiped up with a lint free tissue and allowed to stand free at room temperature for 5 minutes so that all the excessive surface water evaporate before the weight measurement. A digital balance with a resolution of 0.01mg is used for the determination of  $w_d$  and  $w(t)$ .

In the case of water as the diffusing substance, the data can be converted to the average volume concentration of moisture in the following manner:

$$\bar{c}(t) = \frac{\rho_e}{\rho_w} w_g(t) \quad (5.8)$$

in which  $\rho_e = 1.2g/cm^3$  and  $\rho_w = 1g/cm^3$  are the densities of epoxy and water respectively. The absorption curves for the two specimens are reported in Fig.5.2. It can be noted that both the curves coincide for long absorption times indicating that the saturation is a material constant for the tested ageing conditions. Moreover, the difference in the intermediate times is due to the difference in geometry of the coupons since the dogbones, having lower mass and bigger exposed surface, reach the saturation level faster than the SFC cell.

## 5.4 Diffusion identification

The identification process is dedicated in first place to the determination of the type of diffusion law that best represents the behavior recorded in Fig.5.2. In particular, the Fick's diffusion law and a diffusion law having the diffusivity parameter dependent on the concentration are considered. Afterwards, the parameters for each law are determined.

Two finite element models with the following characteristics have been implemented in the software Abaqus:

For what concerns the SFC one half of the geometry has been modeled using 25783 axial symmetric, mass diffusion, 8 nodes quadratic elements (DCAX8). On the other hand, the dogbone geometry has been approximated with 11445 elements of the same type. In both cases, normalized concentration  $c^* = 1$  at the free surfaces has been imposed for times  $t \geq 0$ , whereas in the volume  $c^* = 0$  at  $t = 0$ . The glass fiber in the SFC has been considered to not absorb water thus its diffusivity has been set equal to zero. Details of the mesh and

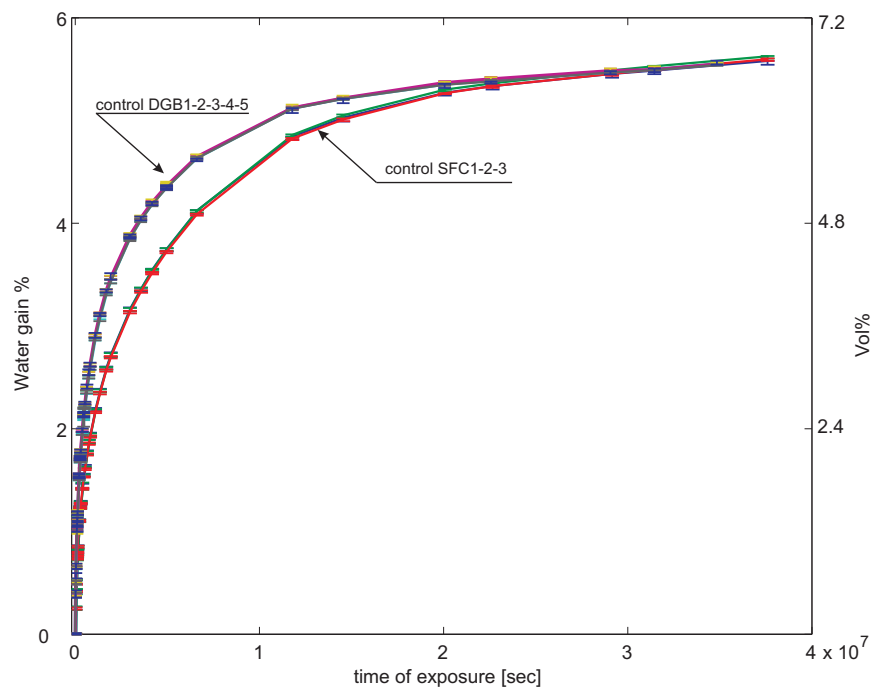


Figure 5.2: Absorption curves for dogbone and single fiber composite cell. Error bars are calculated on the basis of the standard deviation of ten consecutive measurements.

Table 5.1: Identified parameter: Fick's law of diffusion.

Fick's law of diffusion			
SFC		Dogbone	
D [ $mm^2/s$ ]	s [vol.%]	D [ $mm^2/s$ ]	s [vol.%]
$9.208 \times 10^{-7}$	6.55	$8.7046 \times 10^{-7}$	6.51

Table 5.2: Identified parameters: Concentration dependent diffusion.

Concentration dependent diffusion		
SFC		
$D_1[mm^2/s]$	$D_2[mm^2/s]$	s [vol.%]
$2.1471 \times 10^{-6}$	$2.7561 \times 10^{-7}$	6.91
Dogbone		
$D_1[mm^2/s]$	$D_2[mm^2/s]$	s [vol.%]
$2.7432 \times 10^{-6}$	$5.0 \times 10^{-8}$	6.91

boundary conditions can be found in Fig.5.3.

From the data presented in Fig. 5.2 two  $\mathbf{H}$  matrices must be constructed. The column 1 to 3 are meaningless in the present case since the weight gained is an integral quantity, thus only the 4<sup>th</sup> and 5<sup>th</sup> are introduced. In particular, in the case of the SFC the solution is controlled in 134 time points (leading to  $\mathbf{H}_{134 \times 2}$ ) whereas for the dogbone specimen in 32 (leading to  $\mathbf{H}_{32 \times 2}$ ). The discrepancy in the number of check points is in part due to the relatively fast water uptake of the dogbone specimens.

The model calculates the total amount of solute for each time point so to fill the matrix  $\mathbf{O}$  accordingly. The error is then calculated using (2.29) as follows:

$$ERR_k(i) = \frac{\bar{c}^{FE}(t_i) - \bar{c}^{EXP}(t_i)}{\langle \bar{c}^{EXP}(t_i) \rangle} \quad (5.9)$$

In first place the Fick's law is considered. The 2 parameters,  $D$  and  $s$ , are set free of constrains allowing the Livemberg-Marquard solver able to find the values that minimize the error within the given identification tolerance  $\epsilon$ . The results are reported in Table 5.1. As expected, the identified values are very close for both the geometries.

Lastly, the concentration dependent diffusion is considered. In this case



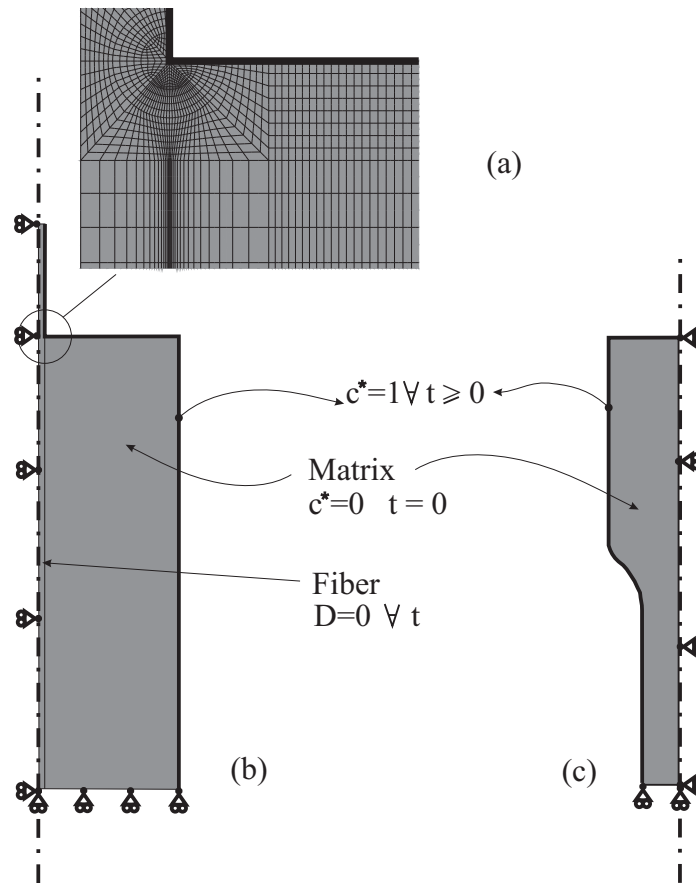


Figure 5.3: Details of the FE models: a) details of the mesh at the fiber insertion, b) SFC, c) dogbone specimen.

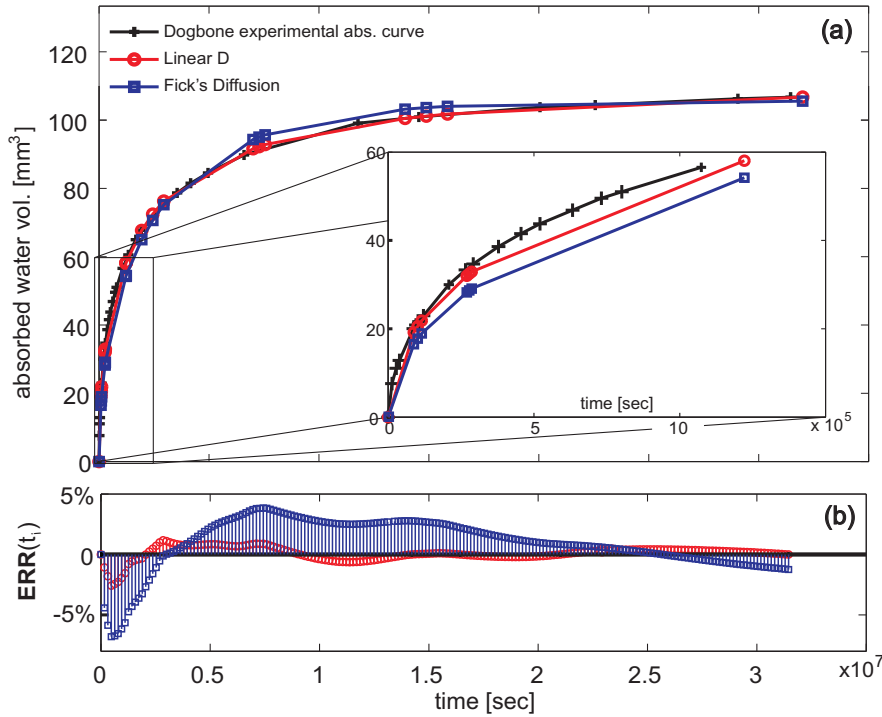


Figure 5.4: Dogbone diffusion identification results: a) calculated and experimental absorption curves, b) relative error.

the identification procedure is divided in two steps.

First step: the 3 parameters for the two geometries are identified without constraints. It is found that the saturation level has a higher convergence sensitivity with respect to the two diffusivity parameters  $D_1$  and  $D_2$ . Considering the experimental data and the fact that, even for this diffusion law, the discrepancy in the identified saturation levels for the two geometries is small, the  $s$  parameter was fixed with a value equal to the average of the two, i.e  $s = 0.0691$ .

Second step: the identification procedure is restarted with the  $\mathbf{i}$  vector composed solely by  $D_1$  and  $D_2$  whereas the  $s$  parameter is given in the  $\mathbf{m}$  vector. The results are reported in Table 5.2. In order to quantify the goodness of each predictions with respect to the identified values, the comparison between the experimental and calculated absorption curves is proposed in Fig. 5.4, for the dogbone geometry, and in Fig.5.5 for the SFC geometry.

It can be noticed that, for both geometries, the concentration dependent diffusion most accurately reproduces the recorded experimental behavior. In

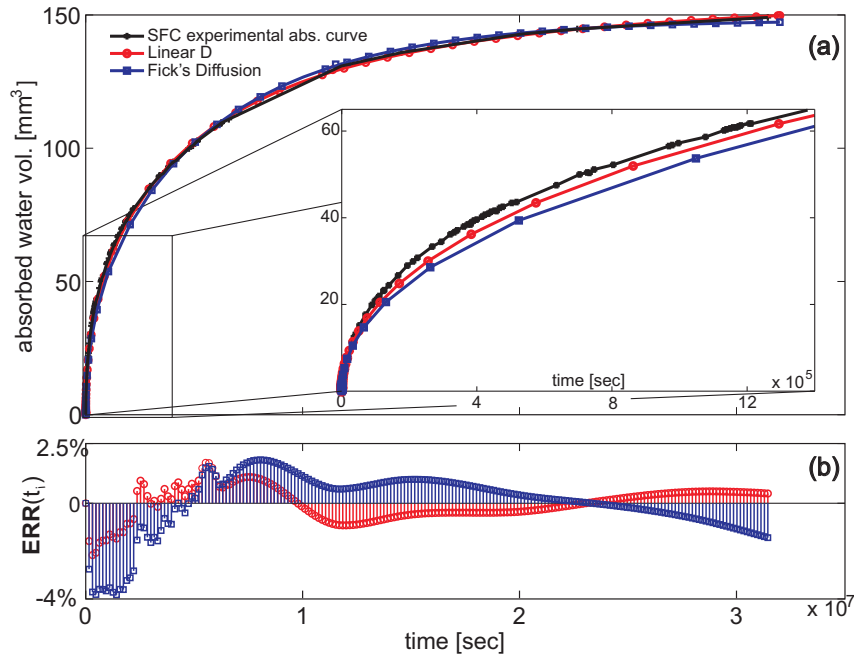


Figure 5.5: SFC diffusion identification results: a) calculated and experimental absorption curves, b) relative error.

particular, it is more capable of capturing the initial steep gradient of absorbed water. Moreover, in the long time range, it shows a better accuracy in predicting the saturation level. In fact, the error, in the corresponding zone, appears to be bounded and close to zero whereas, in the Fick's diffusion law, the error appears to be increasing at long times suggesting that the determined saturation value may be underestimated.

In the following, the concentration dependent diffusion is assumed to control the water absorption and the values reported in Table 5.2 are used. The predicted concentration field  $c(r, z)$  inside the SFC geometry is illustrated in Fig. 5.6 where iso-concentration lines, calculated on the basis of the adopted law, are reported for few representative times. The deformation of the specimen is calculated using the coefficient of moisture expansions described in section 7.2.1.

Furthermore, the concentration profile calculated along the radius at  $z = 20\text{mm}$  for the two diffusion models is reported in Fig. 5.7. As can be seen, the concentration dependent law generates a noticeable steeper gradient close to the external surface. The difference between the two diffusion laws in the

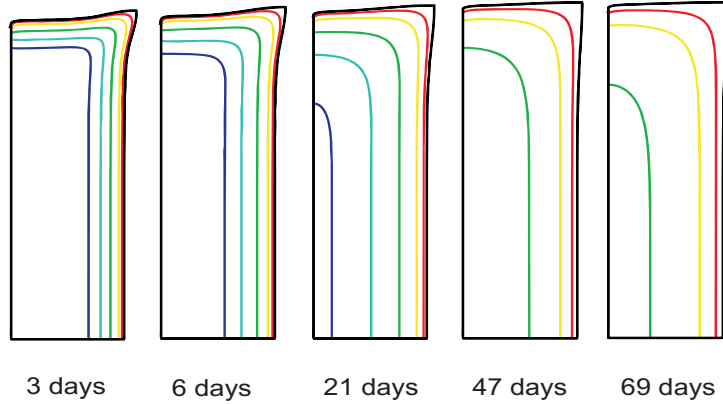


Figure 5.6: SFC iso-concentration profiles calculated using the concentration dependent diffusion law. Isoconcentration lines at 10%, 25%, 50%, 75%, 90% of the saturation.

mid-term, i.e.  $\sim 220$  days, is noticeable even if the error in the absorption curve is around 5%. The gap is then progressively reduced as the saturation level approaches.

## 5.5 Diffusion characteristic time

The solution of the Fick's diffusion equation in the case of a hollow cylinder exposed to moisture at its external surface can be expressed as an infinite series in terms of the Bessel function of zero and of the first kind [84] :

$$\frac{c(r, t)}{c_0} = 1 - 2 \sum_{k=1}^{\infty} e\left(-\frac{M_k^2}{R^2} Dt\right) \frac{J_0\left(\frac{M_k r}{R}\right)}{M_k J_1(M_k)} \quad (5.10)$$

where  $M_k$  are the positive roots of the equation  $J_0(M_k) = 0$ ,  $r$  and  $R$  are the internal and external radii respectively and  $D$  is diffusivity parameter. For large times and for  $r \ll R$  the series converges rapidly to the expression

$$c(t) = c_0 \left[ 1 - 1.6e^{-\frac{t}{\theta_c}} \right] \quad (5.11)$$

where

$$\theta_c = \frac{R^2}{D} 0.1736 \quad (5.12)$$

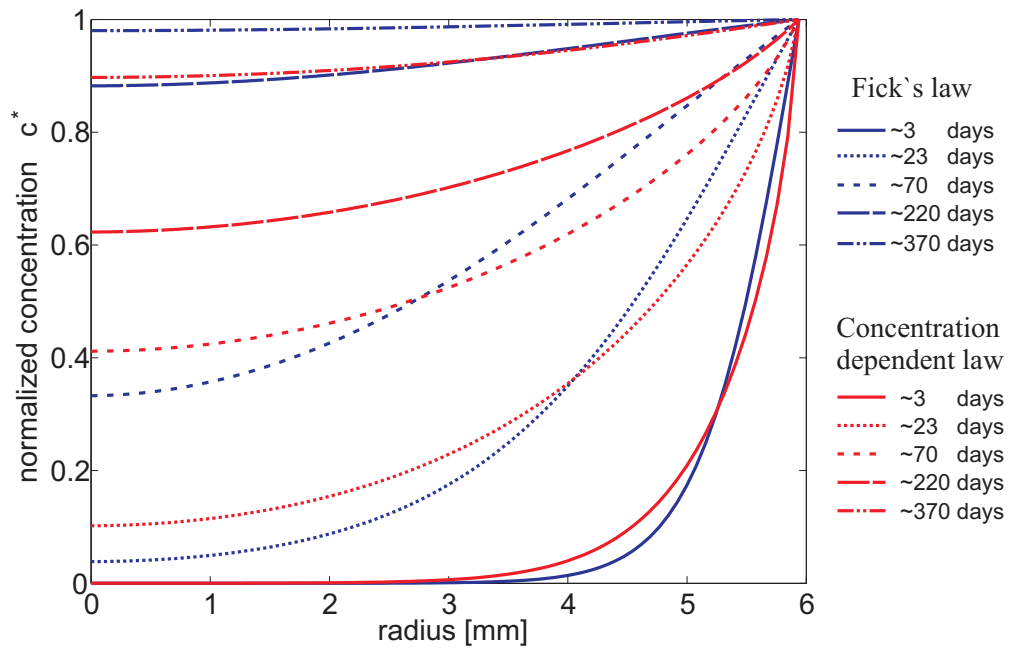


Figure 5.7: Concentration profiles for the single fiber cell at the specimen middle plane along the radius as function of the diffusion time.

is the characteristic time for the moisture diffusion process. In order to have a first conservative approximation of  $\theta_c$ , the larger identified value of  $D$ , i.e. for the concentration dependent diffusion law the one at  $c = 0$ , is used in Eq. 5.12 leading to  $\theta_c \simeq 2.91 \times 10^6 \text{sec}$ .



# Chapter 6

## Material properties evolution

The resin mechanical properties are known to widely vary with the environmental conditions. In fact, service conditions in which the temperature is close, or beyond, the glass transition temperature are detrimental for the mechanical performances. Moreover, the presence of humidity decreases even more these properties as it diffuses through the components. For this reason the evolution of the resin mechanical characteristics are investigated at room temperature, at 50°C (the ageing temperature), and with increasing water content by means of tensile, relaxation and indentations tests.

### 6.1 Introduction

The problem has been investigated in the past highlighting the detrimental influence of wet-hot environment on the mechanical performances of resin based materials. In general the scientific effort was divided in analyzing directly the influence that water has on the bare matrix or in analyzing its repercussions on final products, e.g., on composites. Although the latter type of analysis is more interesting from a production stand point, it inherently has the drawback of not identifying the reasons that create the decrease of properties because of the large number of parameters involved. In fact, stacking sequence, residual stresses, differences in interfacial properties, in reinforcement sizing, voids percent etc. can lead a nominally identical composite to suffer at a greater or lower extent the hygrothermal ageing. On the other hand, the micromechanical analysis places the emphasis on the parameters responsible for the reduction

of the composite properties. It must be taken into consideration that, in this latter case, an additional effort has to be carried out since homogenization analysis and/or micromechanics simulations are needed to compare the results with the one obtained at the composite scale. It is in this framework that both the type of studies lead to a complete understanding of all the physico-chemical mechanisms that are involved in the ageing process of composites.

Concerning the evolution of the material properties of the neat resin, the first parameter studied was the glass transition temperature ( $T_g$ ). Among others, Ellis reported in [85] that  $T_g$  decreases roughly by 10°C per one weight percent of absorbed water. More recently, Zhou and Lucas in [86] linked this decrease to the morphological change induced by the water on the epoxy polymeric chains. In particular they reported that not only the water content but also the hygrothermal history of the specimens determines the evolution of this property. In fact, if a sudden drop was found to occur at the beginning of the diffusion process, a certain recovery of the property was recorded, depending on the temperature of the ageing environment, since a “secondary cross linking” effect can be established by the water molecules bridging separated polymeric chains. The latter analysis is partially corroborated by Papanicolaou et al. [87] who showed, for a DGEBA-DETA system, the importance of the temperature at which the diffusion takes place in the drop of material properties. In fact, using three point bending tests and tensile tests conducted at room temperature, they showed that at saturation the Young’s modulus decreased by 10% for diffusion at 60°C whereas at 80°C they recorded a decrease of 20%. Similar trends were found for tensile strength and fracture stress. The variation of viscoelastic properties with water is often investigated using DMA analysis. Among others, Nogueira et al. [8] described the plasticization process induced by water absorption showing an important shift of the  $\tan\delta$  towards lower temperatures. This behavior indicates an increase of relaxation time constants for a viscoelastic material. Nevertheless this behavior is not universally valid for all the systems since the opposite behavior is also reported by Papanicolau [87].

These macroscopical property changes have repercussions on the behavior of epoxy based composites. As could be expected, it is found that the matrix dominated composite properties are affected by moisture. In particular, according to Browning et al. [10], transverse and in-plane shear stress-strain



curves shows practically the same decrease as the neat resin. It is also underlined that the strength loss in unidirectional composites is found more severe with respect to the neat resin because of possible degradation of the interphase properties. Moreover, they found, in the case of quasi isotropic laminates ( $[0, \pm 45, 90]_s$ ) subjected to tension, a change in fracture mode. In fact, the reduced load bearing capacity of the  $\pm 45^\circ$  plies, because of moisture presence, led to a matrix dominated fracture instead of failure of the reinforcement [10]. The interlaminar delamination-toughness is also affected by moisture content. In particular Asp in [11] reported how the mode II energy release rate is more affected by water content than that of mode I. Furthermore, the synergistic effect between temperature and moisture is also capable of changing the propagation behavior from instable to stable [11].

Concluding this brief survey some remarks can be made. First, each polymeric system is more or less sensitive to hot-water environments leading to the necessity for appropriate testing of the material under study. Second, a complex relationship is often reported between temperature and humidity making imperative to test the combination of the two. Third, properties reported in literature are usually expressed as function of the average moisture/water content while the diffusion process generates a gradient of concentration through the thickness of the samples and thus a gradient of properties. This concept will be discussed in more details in Section 6.3.

## 6.2 Tensile and Relaxation tests

To assess the influence of the progressive water uptake on the mechanical properties of the epoxy, tensile and relaxation tests were conducted on 6 sets of at least 5 dogbone (DGB) specimens each. The base line properties of the epoxy were measured on dry specimens at room temperature whereas, for dry samples at  $50^\circ\text{C}$ , a climatic chamber with forced hot air circulation was used. The influence of the absorbed water was investigated by testing the DGB specimens aged at different time periods thus, containing increasing average water content.

These latter tests were performed in water at  $50^\circ\text{C}$  using a specially designed bath mounted on an Instron traction machine (MicroTester 5848), the

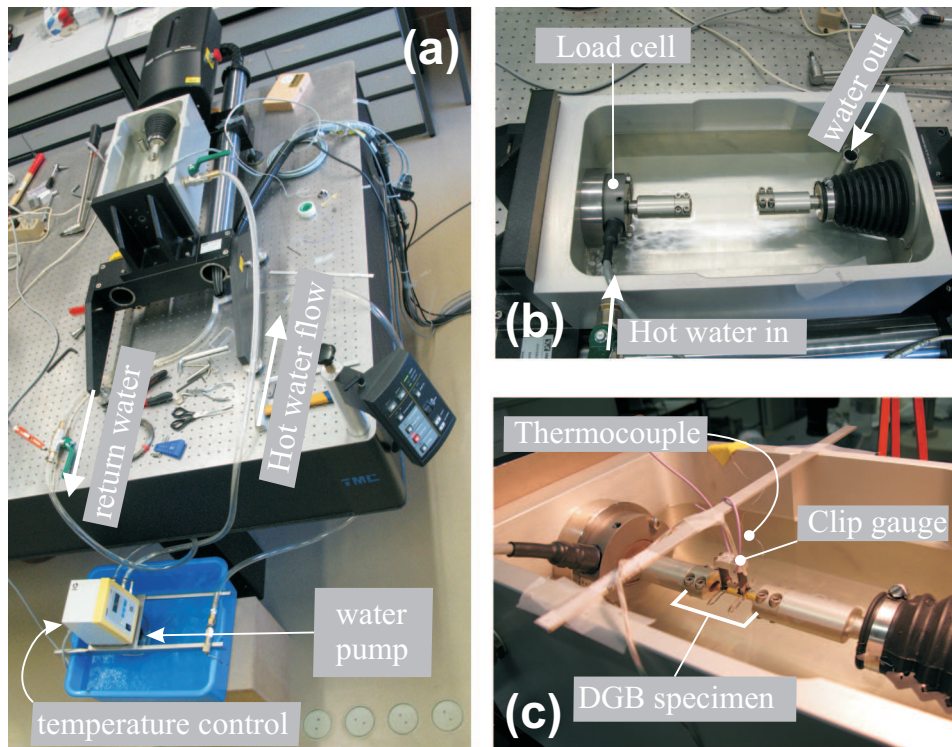


Figure 6.1: Tensile and relaxation setup.

setup is shown in Fig. 6.1. A water flow was generated using a thermostatic pump and, in order to prevent moisture desorption from the specimens, the water level was kept constant in such a way to completely cover the specimen's gage length. The bath was furthermore equipped with a submersible load cell of  $\pm 2\text{kN}$ , the elongation in the specimen's central part was measured with a clip gage and a thermocouple acquisition system recorded the effective bath temperature during the test. Considering the characteristic time of diffusion as compared to the testing time, additional absorption during the mechanical tests was considered negligible.

Each specimen was removed from the ageing bath right before testing, weighted in order to establish the water content, placed in the testing bath, attached to the traction machine and allowed to reach thermal equilibrium at  $50^\circ\text{C}$  for 15 minutes.

The tensile-test specimens were pulled to fracture with a crosshead displacement rate of  $1\text{mm}/\text{min}$  to obtain the stress-strain curve (Fig.6.2). The short term (ST) modulus (Fig.6.3) is calculated as the linear regression of the

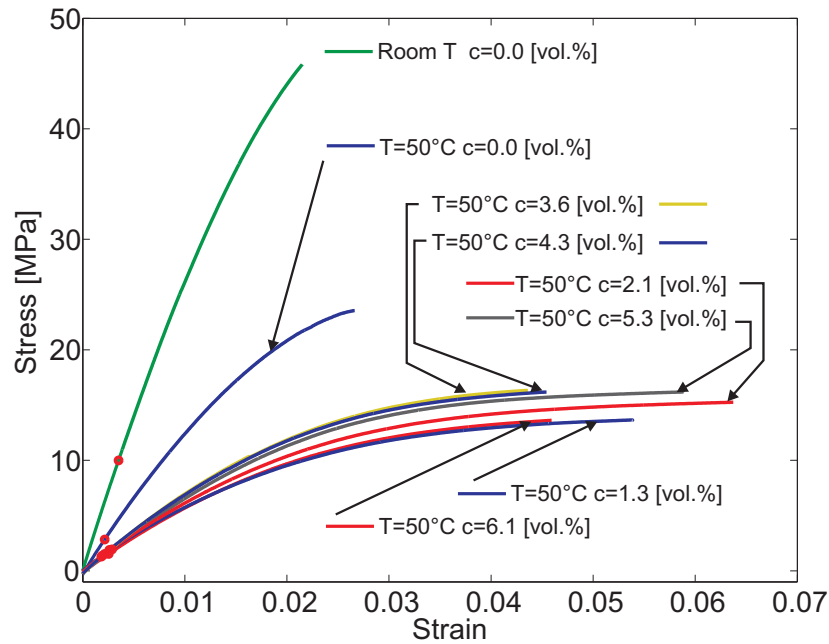


Figure 6.2: Epoxy stress-strain curve as function of temperature and water concentration. Circles indicate the yield stress.

first part of each curve. (a maximum difference of 5% is tolerated from the very initial slope)

The plasticization effect of temperature and moisture is noticeable in Fig.6.2 where the plastic-strain range is 3 times widened by moisture content with respect to the epoxy at room temperature and at 50°C. On the other hand, the effect of temperature is remarkable in the decrease of the yield stress whereas the water seems not to introduce a dramatic change. Moreover, the influence of the water content on the ST modulus is reported in Fig.6.3 where, after the first drop at  $\sim 1.2$  vol.% that reduces the ST modulus by 45%, an almost constant value is found. Note that the initial value, at zero water content and at 50°C, is half the value of the modulus at room temperature in dry condition (2400 MPa).

To shed light on the time scale of the elastic modulus, relaxation tests are also carried out as follows: with the same setup and loading rate used for the ST modulus, tests are performed by imposing 4 successive levels of deformation, held for 30 min each, and separated by a complete discharge to zero-force, where they are maintained for 10 minutes for the specimen to stabilize. For each level of water content, the first strain level is chosen in the

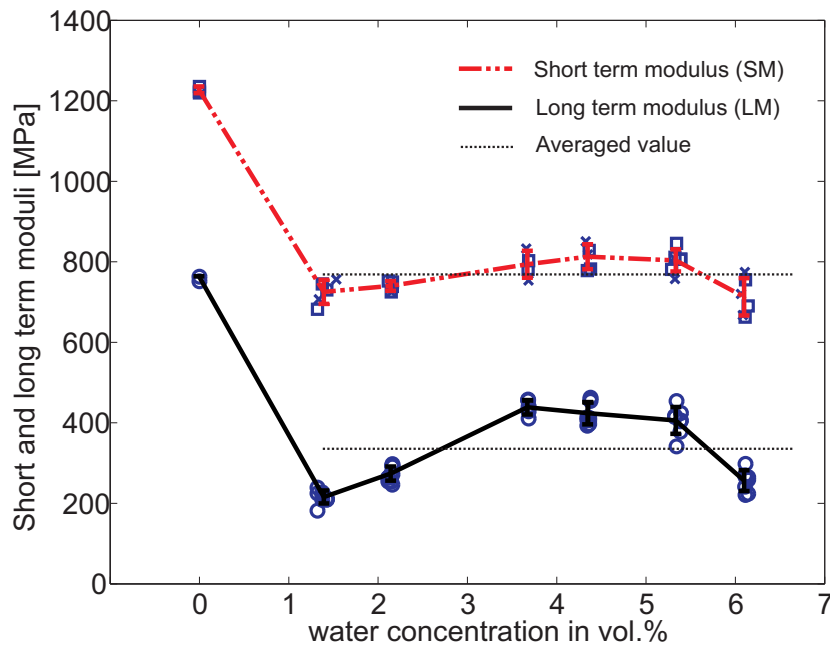


Figure 6.3: Short and long term moduli as function of water volume content, all data points obtained at 50°C.

linear elastic range (determined with the tensile tests) whereas the three other levels are chosen increasingly higher and close to the early irreversible region of the stress-strain curve afterwards the specimens are pulled to fracture. The typical response curve of the relaxation tests is reported in Fig.6.4.

The stress relaxation evolution is fitted with a 3-term Prony series and the relative characteristic times are calculated by a non linear least square regression analysis using Matlab. The average relaxed modulus is calculated by dividing the asymptotic stress, from the Prony series, with the applied strain. The so-calculated modulus is referred to as a long term (LT) modulus. Its evolution as function of water concentration is reported in Fig.6.3 where it is possible to notice that a partial recover of the property is present after the sudden drop at  $\sim 1.2$  vol.%.

The relaxation times ( $i = 1,2,3$ ), calculated by fitting the data with a 3 term Prony series, vary from  $\sim 500$  sec. at 0vol.% and  $\sim 2000$  sec at about 3.7vol.%. Compared to the characteristic time of the diffusion process, which is in the order of  $10^6$ sec, the characteristic times of the visco-elastic response of the resin are much smaller. Due to this large difference, the viscous relaxation and the moisture diffusion processes can be considered practically decoupled in

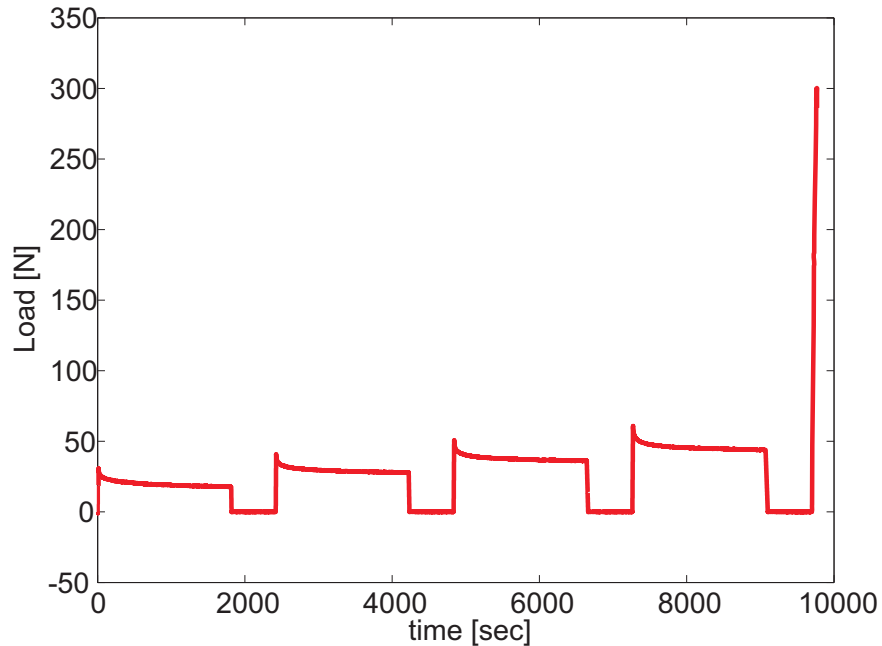


Figure 6.4: Relaxation test profile.

the particular ageing experiment leading to the assumption that the resin can be considered as a fully relaxed visco-elastic material with a Young's modulus equal to the LT modulus. However, the trend of the LT moduli in Fig.6.3 is not fully understood and, in the following, the evolution of this parameter is considered flat after the initial drop and equal to the average of the measured values at the different water content. It is worth mentioning that the trend of the data in Fig.6.3 could be qualitatively explained if one considers the possibility that water acts not only as polymer chain disruptor but also as “pseudo cross linking agent” establishing hydrogen bonds among polymeric chains as reported in [86].

## 6.3 Indentation tests

The material properties in Section 6.2 are reported as function of the average concentration of the specimen expressed in volume percent. Although this way of reporting the data is common practice in literature because it gives the global trend of the water influence on the mechanical properties, it presents a conceptual drawback if these values, as it is the case in this work, are used

in FE simulations. In fact, the following implicit assumption is made: the change in the overall response of the material as function of its average water content is assumed formally equal to the punctual response as function of the local concentration. In other words, the diffusion process generates a concentration gradient that evolves in time. For a given time, a gradient of properties along the diffusion path is created, meaning that an equivalent continuous distribution of series of slightly different materials is produced. The mechanical response of the total volume of matter, for example to a uniaxial tensile test, will be a weighted average of the properties of each material, where, the weights are functions of the local concentration. Since only the global response of the material and the average concentration can be experimentally measured the correspondence between the local material properties and the local concentration cannot be established experimentally. Hence, in a FE model, where the material properties are assigned in a local way, an element with a given local concentration, because calculated by a diffusion law, would have material properties corresponding to the global behavior of the volume measured at a concentration value that corresponds to the average concentration. This implies an error in the calculations that is linked to the magnitude of the concentration gradient: the steeper the gradient the greater the error. To address the severity of the problem a different approach capable of retrieving the evolution of the material properties is needed.

In the past years, a lot of work has been carried out on the development of micro- and nano-indentation tests and apparatuses. They are nowadays widely used to characterize the hardness of materials and, especially in biomechanics, to identify gradient of properties for instance in bones and cartilages. On the basis of the more up to date findings on the indentation technique a custom setup is developed (Fig. 6.5) and calibrated, and a modified testing procedure is established.

### **6.3.1 Indentation methodology development**

Considering the SFC cell the first problem to face is the identification of an indentation region that presents a gradient of properties. Evidently, no free surfaces are available with these characteristics since the whole external surface is in fully saturated condition. For this reason, a radial cut is introduced with

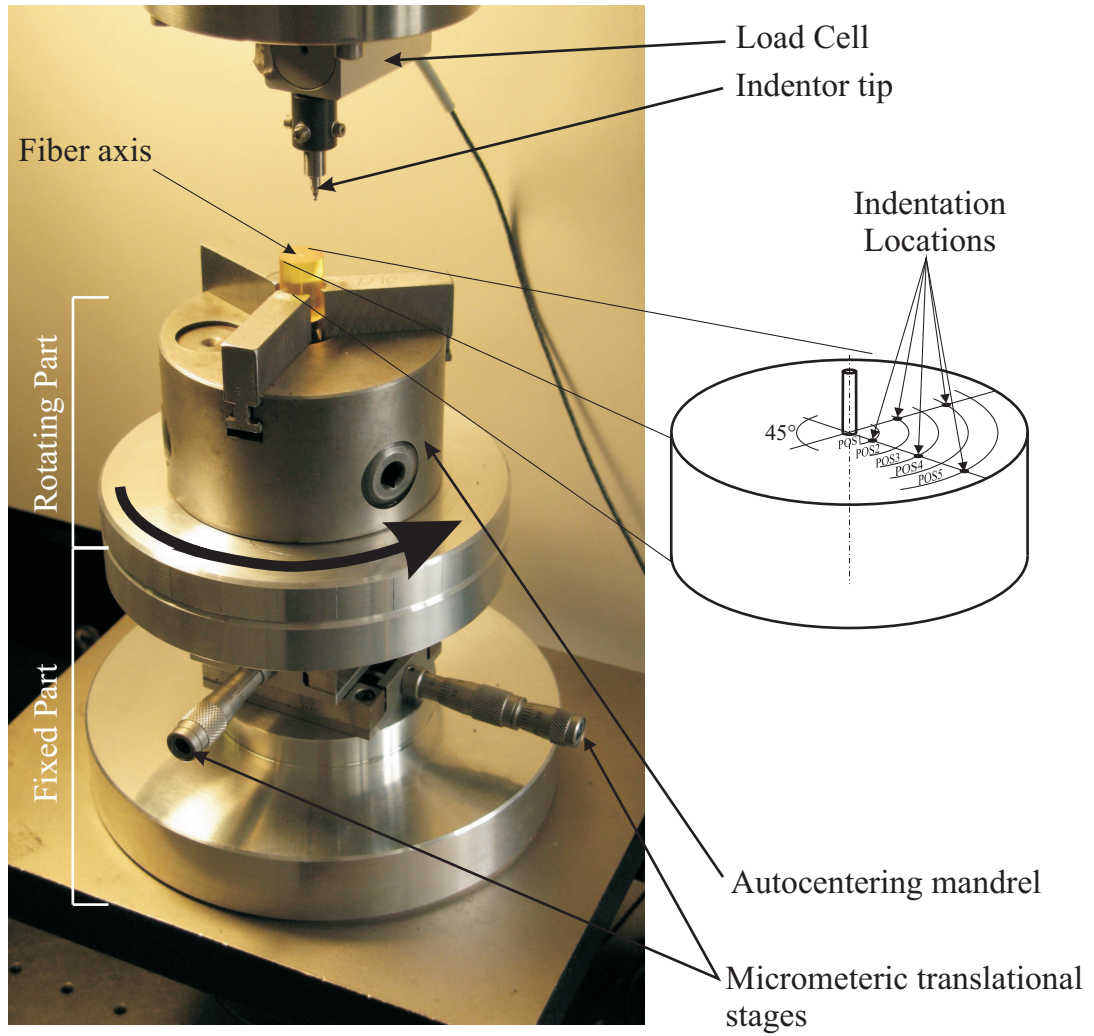


Figure 6.5: Detail of the indentation setup.

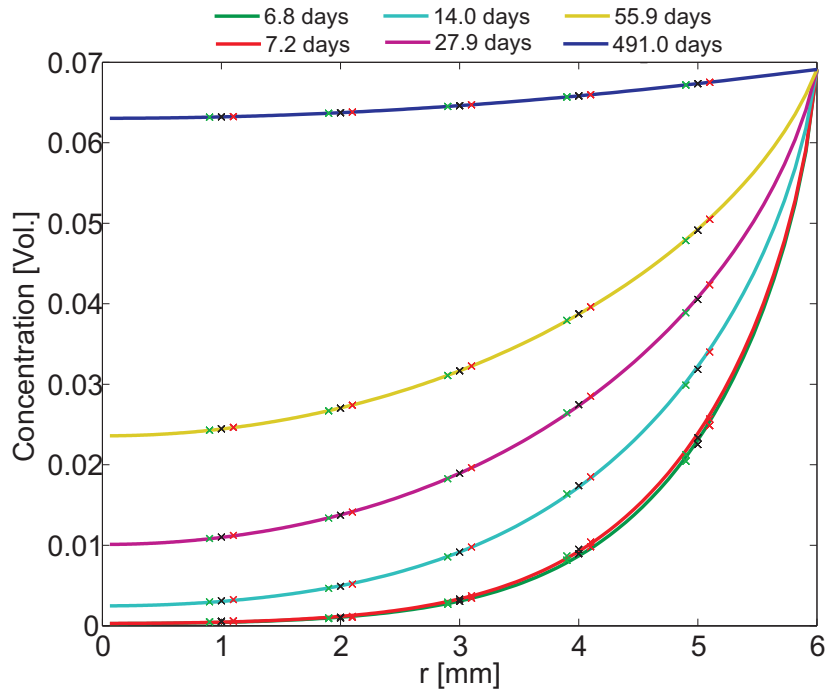


Figure 6.6: Concentration profiles as function of the radius at the SFC cell middle plane. Black crosses indicate the indentation nominal coordinates whereas the green and red ones indicate the maximum positioning error.

a lathe at the middle plane of the SFC subdividing the specimen in two parts. The two new obtained-surfaces have a radial concentration distribution since, in that zone, diffusion can be considered essentially radial and not influenced by the diffusion through the edge as shown in Fig.5.6.

On the basis of the diffusion model identified in Chapter 5, the local concentration in the whole SFC specimen is known at any time and in particular at the specimen middle plane. Seven specimens were aged for 5 different periods of time in such a way that the gradients produced were sufficiently different to be distinguished. In Fig. 6.6 calculated concentration profiles for the selected ageing times are reported as function of the SFC radius.

Five indentation positions were identified with respect to the distance from the specimen axis: at 1, 2, 3, 4, 5mm from the fiber and labeled *POS1*, *POS2*,... . Because the planned indentations are off axis, the specimens need to be clamped with a mandrel as illustrated in Fig.6.5. Moreover, in order to limit the amount of plasticity developed during the test a spherical indenter tip was used.



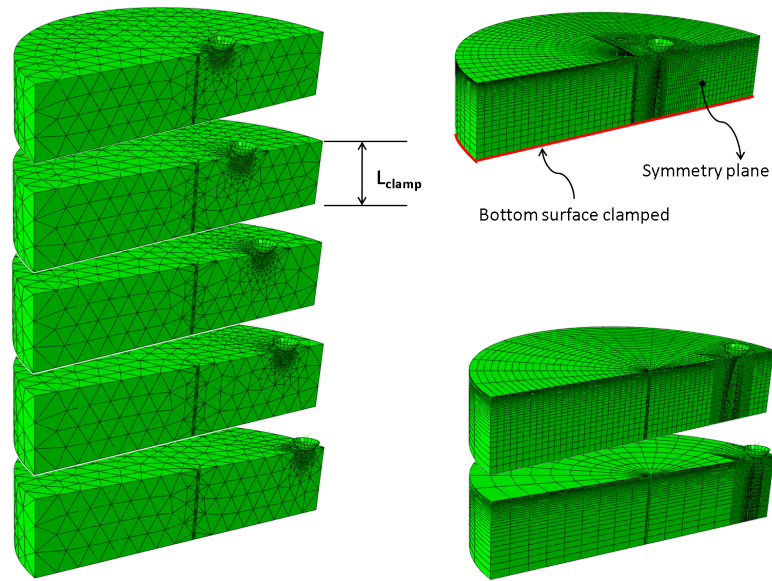


Figure 6.7: Mesh detail of the indentation model.

With the chosen testing configuration few points must be examined in order to ensure the accurate determination of the effective properties of the epoxy:

1. to what extent the presence of the fiber influences the indentation in *POS1*
2. to what extent the vicinity of the edge influences the indentation in *POS5*
3. to what extent the distance  $L_{clamp}$ , of the clamped surface from the test surface influences the tests
4. what is the indentation depth that allows for distinguishing the material properties evolution.

All these points were addressed implementing several FE models in Abaqus and the convergence was studied as function of two type of meshes reported in Fig.6.7. Linear elastic material properties for the fiber and the matrix were used whereas the indenter was considered as a infinitely rigid surface. The reaction force calculated by the model as function of the indentation depth is compared to the one predicted by the Herz formula for the contact of a sphere with an infinite plane. In the case of no appreciable influence of the fiber and/or

of boundary conditions the calculated reaction force must tend to the Hertz value. It was found that the minimal distance between the test surface and the clamped one in order not to affect the results was 10mm. The presence of the fiber introduces only small distortion in the stress field underneath the indenter rigidifying the zone by less than  $\sim 0.2\%$  whereas the presence of the free edge introduces a softening effect in the response to an indentation in *POS5* on the order of  $\sim 5\%$ , the intermediate positions resulted not to be affected. Results obtained from the two different meshes were in disagreement by a maximum of 1% at *POS1* whereas discrepancies are negligible for the other positions. After this analysis the  $L_{clamp}$  distance was imposed to 10mm and although indentations were conducted also in position 1 and 5 the results from *POS1* were discarded in the calculation of the elastic modulus. It was confirmed later on by experiments that only results from *POS5* differed significantly from the others adding support to the latter assumption.

Concerning the depth of the indentation, results showed that an indentation of 100 $\mu\text{m}$  is capable of generating a detectable difference in the reaction force produced when the material has a hypothesized material distribution (Fig. 6.8). For this analysis the indentation in *POS3* is considered as representative. The Young's modulus of the epoxy was taken equal to 2400MPa as initial value (dry resin at room temperature) than a fully saturated value of 1200MPa was assumed. The reaction forces generated on the indenter represent the two extremes cases as shown in Fig. 6.8. At this point a linear variation of the modulus, between the two reported extremes, as function of the concentration was supposed. Then, the concentration profiles reported in Fig. 6.6 were imposed in four different simulation allowing for the calculation of the corresponding reaction forces.

From Fig. 6.8 it is also evident that indentations of less than 50  $\mu\text{m}$  generate load differences close to 1N rising the error. Moreover, since some plasticity is expected the maximum indentation step will be considered in the following.

Furthermore, the execution of the test demands some adroitness that must be taken into account since the design of the indenter setup. In first place, a relatively high precision in the radial positioning is desired. In fact, a radial error has repercussions on the results of the test since a material with a different water content is probed. As can be noticed in Fig. 6.6, if a maximum error of

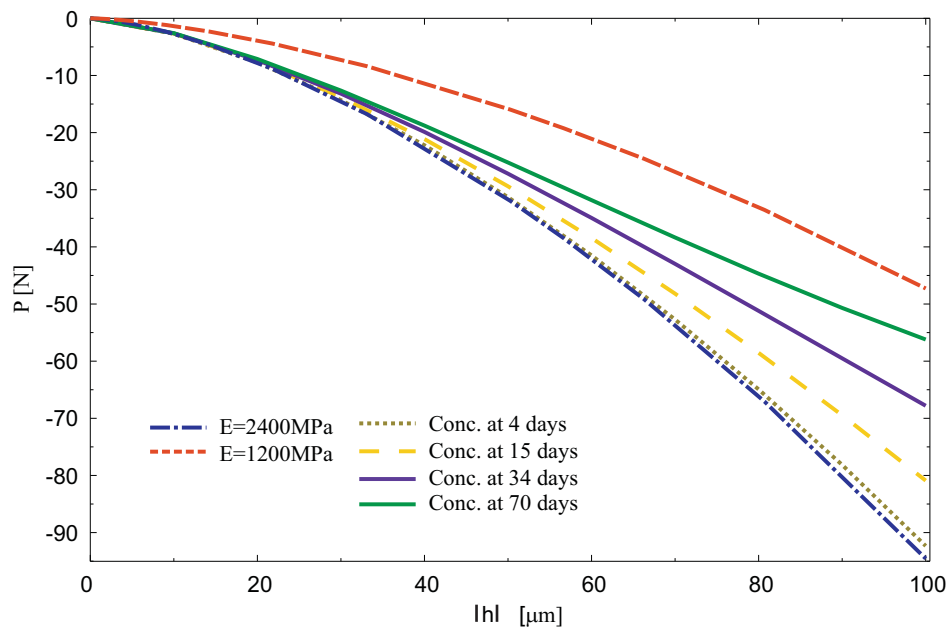


Figure 6.8: Reaction force evolution as function of the indentation depth as predicted by the indentation model. The Young's modulus of the material is varied linearly with concentration. Extremes cases are represented by the dry resin at room temperature, elastic modulus 2400 MPa, and by an estimation of the maximum drop of the property in fully saturated condition at room temperature (1200 MPa).

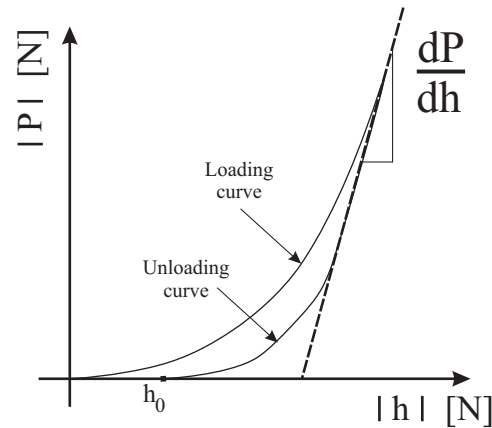


Figure 6.9: Indentation general scheme.

100 $\mu\text{m}$  is assumed, a variation in concentration  $\Delta c$ , identified by the distance between the red and green crosses, is introduced. Secondly, the test, that is conducted at room temperature and in normal laboratory humidity conditions, must be conducted with no loss of time in order to prevent desorption from the specimen.

The indenter concept design is reported in Fig. 6.5. A support is mounted over two micrometric translational stages that allow to move the specimen in the x-y plane. The specimen is clamped on a self-centering mandrel that is constrained radially with 10 $\mu\text{m}$  clearance and it is able to rotate around the specimen axis. The test procedure begins by aligning the tip of the indenter to the specimen's axis. Then, with the help of one of the translational stage, a given radial position is selected. Next, an indentation is performed at the end of which the mandrel is rotated of 90° in order to conduct an new indentation at the same radius, thus probing the same material properties. For each radial position 4 indentations are completed. Note that in the adjacent radii the indentation locations are shifted of 45° in order to eliminate their mutual influence on the results (Fig. 6.5). Finally, the radial position is changed progressively leading to a series of concentric indentation that allow to determine the radial evolution of material properties as function of the local concentration. The process is repeated for different specimens aged for different time periods.

Considering a single indentation, the load-displacement curve assumes the general shape reported in Fig. 6.9 where the absolute load and displacement

are reported in absolute value. Both the loading and the unloading curve can be expressed as a power law of the indentation displacement  $h$  as follows:

$$\begin{aligned} P_{loading} &= Bh^{\alpha_1} \\ P_{unloading} &= C(h - h_0)^{\alpha_2} \end{aligned} \quad (6.1)$$

where  $B$  and  $C$  are constants,  $\alpha_1$  and  $\alpha_2$  are the “degree” of the indentation, and  $h_0$  is the plastic residual displacement when the indenter tip loses contact with the surface. The exponents have a value of 1.5 in the case of a spherical indenter and for a linear elastic material, value that corresponds to Hertzian theory of contact. If a more complex constitutive law describes the behavior of the material, involving for instance plasticity and/or viscoelasticity, the exponents assume different values. Moreover, the slope of the initial part of the unloading curve can be related to the Young’s modulus of the indented surface using the following equation [88]:

$$\frac{dP}{dh} = \frac{2}{\sqrt{\pi}} \sqrt{A} \frac{E}{(1 - \nu^2)} \quad (6.2)$$

where  $A = f(h)$  is the contact area that depends on the indentation depth,  $E$  is the Young’s modulus of the material and  $\nu$  is its Poisson’s ratio. This relationship assumes that at the very beginning of the unloading the contact area between the indenter and the surface remains constant. Using the Sneddon analysis of contact [89], it was shown by Pharr et al. in [88] that the latter assumption is always verified for all axisymmetric indentors, i.e., in this case. Furthermore, it has been established experimentally that the contact area developed by a spherical indenter conserves its shape while the radius is slightly bigger than the nominal indenter value. In this case the contact area can be calculated using

$$A = \pi (h_{max} - h_0) R \quad (6.3)$$

Due to the low load level produced during the test, a 100N load cell is used. The inherent compliance of the load cell the compliance make necessary to evaluate the one of the entire setup that is evaluated using as reference a steel surface with known materials properties [90]. Using an optical microscope the radii of the imprints let by the indenter tip at different indentation depths are

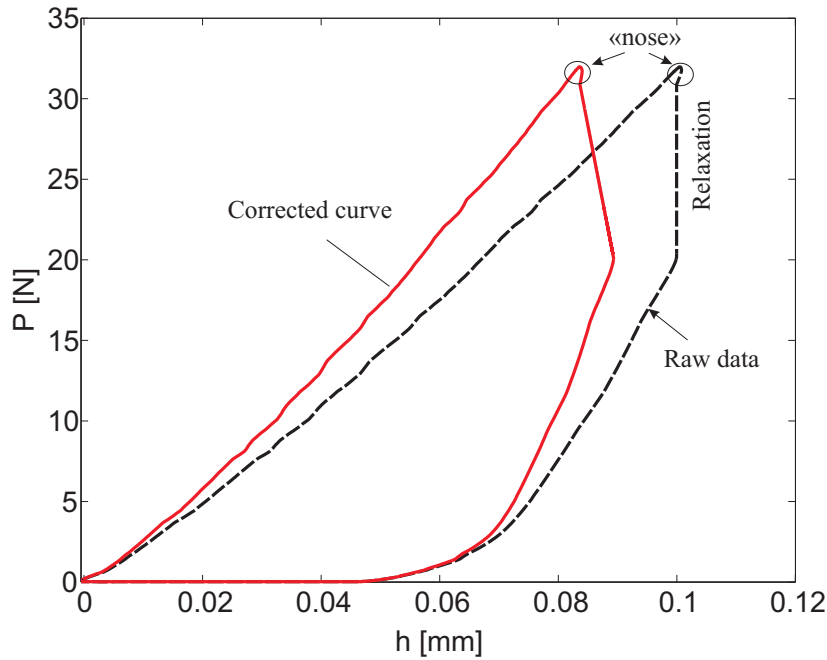


Figure 6.10: Load-indentation depth curve: raw data and correction due to indentation setup stiffness.

evaluated assuming a concavity of spherical shape. This process determines the stiffness of the setup, evaluated equal to  $\sim 1893Nmm$ , that allows to recover the elastic properties of the steel using Eq. 6.2.

Furthermore, the schematic Load-indentation-depth curve can significantly differ from the one reported in Fig. 6.9 if the material under study undergoes to long term relaxation during the loading. In particular the sharp angle formed between the loading and unloading curves could not be present, instead a typical “nose” (e.g. Fig. 6.10) is produced making difficult to identify the initial slope and thus the Yong’s modulus of the material. For this reason, two precautions were adopted:

- a relaxation step is introduced between loading and unloading as reported in Fig. 6.10
- $\frac{dP}{dh}$  is calculated by fitting the unloading curve with the second of the expressions 6.1, as suggested in [91], and evaluating the derivative of the expression at the maximum indentation depth.

Using this procedure the evolution of the Young’s modulus of the epoxy as

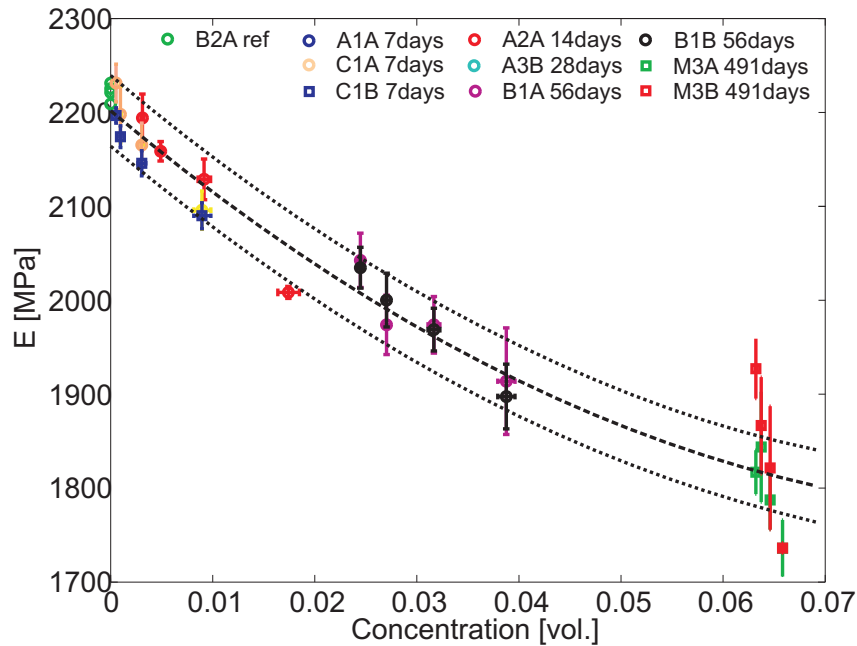


Figure 6.11: Young's modulus as function of local water concentration at room temperature.

function of the local concentration is determined. The results are reported in Fig.6.11. The values were obtained by the average among all the indentation conducted at a given radius and for the same exposure time.

The specimen label identifies the production batch (the first letter), the specimen number, and the tested surface (second letter). The horizontal error bars are obtained assuming a positioning error as reported in Fig. 6.6 whereas the vertical error is  $\pm$  the standard deviation. It can be seen that the data correlate very well and indicate a smooth gradient of properties as function of the local concentration. It is also worth noticing that, assuming as constant the ratio between the short term modulus in dry condition at room temperature and at 50°C (i.e.  $\sim 2$  from Fig. 6.2) the data reported in Fig. 6.11 can be shifted to 50°C. In this case, the same total drop of the property is found when compared to the tensile tests results shown in Fig.6.3 while a smoother gradient is recovered.

The evolution of the local Young's modulus is used in a FE model where a tensile test is simulated during water diffusion. The average response of the volume, that corresponds to the one that would be measured in the same conditions by means of a tensile test is reported in Fig. 6.12 and compared to

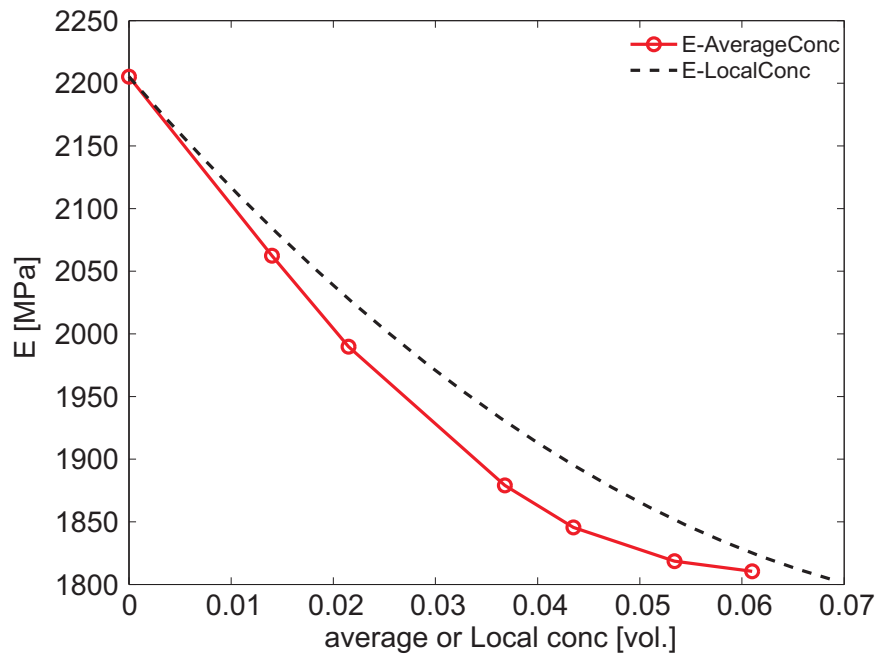


Figure 6.12: Comparison of local and averaged E.

the input data. Note that the difference between the two curves is zero when the concentration gradient is also zero (at  $t = 0$  and at the saturation) while it reaches a maximum,  $\sim 80MPa$  around 0.038 water volume. The difference is found to be small in the present case justifying the assumption that the average material properties evolution can be used, in first approximation, as input in the FE model.

## 6.4 Glass transition temperature evolution

As reported in Section 6.1 the glass transition temperature is influenced by the water uptake. In order to evaluate to what extent this property has an influence on the results the evolution of the  $T_g$  must be studied. In the present case the initial value in the after drying condition and the drop at the saturation point are determined using the differential scanning calorimetry. The results (Fig. 6.13) indicate that the initial value of the glass transition temperature is in the order of  $84^\circ C$ . The absorption of 6.91 water *vol.%* reduced the  $T_g$  to  $38^\circ C$ , i.e., a reduction of  $8^\circ C$  per weight percent gained. This value is in very good agreement with what reported in literature. From these results, and assuming



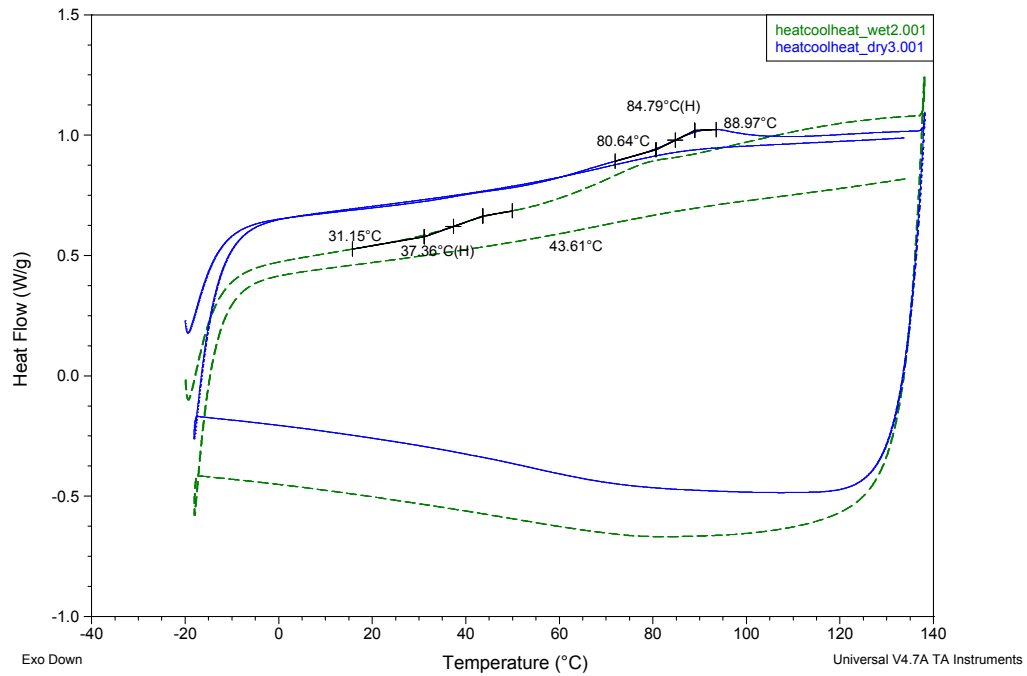


Figure 6.13: DSC analysis.

a linear variation of the property with the water weight percent [85], the  $T_g$  will equal the ageing temperature when the total water uptake is close to  $\sim 4.25w_g\%$  ( $\sim 5.1vol.\%$ )



# Chapter 7

## Modeling of ageing in a single fiber composite

In this chapter two main aspects are studied separately:

1. the residual stress field stored into the SFC by means of an inverse approach,
2. the determination of the coefficient of moisture expansion using the FBG data and the hygro-elastic model.

Afterwards, a comprehensive model is implemented to accurately reproduce the stress state evolution as water diffusion take place at  $T = 50^{\circ}\text{C}$ . The model takes into account the variation of the elastic and/or plastic properties introduced by the temperature and the water uptake.

### 7.1 Residual stress field determination

Residual stresses are self-equilibrating stresses generated during processing of materials. They constitute an internal non-homogeneous field that, under certain conditions, can facilitate the creation of macroscopic defects in components even before the application of external loads. In particular, in the case of fiber reinforced composites the mutual interaction between the resin matrix and reinforcements during the processing is fairly complicated. In fact, the epoxy matrix undergoes radical physical changes during the cure (Ch. 4).

It passes from a viscous liquid state, not capable of transmitting shear forces, throughout a rubber-like state, as the gelation point is approached, and arrives at the glassy state as the polymerization process terminates. The process is thermally activated and, since the chemical reaction involved is exothermic, usually a gradient of temperature appears inside the material even if the curing schedule foresees an isothermal part. Consequently, the kinetic of the reaction is itself not uniform leading to an intrinsic different evolution of local properties inside the material. Moreover, the epoxy material properties are not the only ones that vary. In fact, the reaction is accompanied by a volume reduction as explained in Section 4.1. Furthermore, when the composite is cooled down to room temperature the constraints, created by the adhesion among the components and between the entire composite and the mould, generate a progressive redistribution of stresses that is function of their corresponding coefficient of thermal expansion mismatch.

A lot of effort has been devoted in the past in analyzing this complex process. Two levels of investigation are generally used: The first one involves the use of simplified geometries and elementary composite unit cells with the aim of simulating the physics of the problem, while the second one has as objective the determination of the residual three dimensional field *a posteriori* by means of destructive or non-destructive techniques.

### 7.1.1 Crack compliance method

One of the most known destructive method for the *a posteriori* determination of the residual stress state in a component is the Crack Compliance Method (CCM). It was developed among others by Cheng and Finnie in [92–95] for metal components. It consists in recording the strains generated by introducing a slit or a crack in the material. The technique is based on the reconstruction of the stress distribution perpendicular to the crack plane as a series of known shape functions whose coefficient are unknown:

$$\sigma = \sum_{i=1}^n A_i P_i \quad (7.1)$$

Two possible methods are available for the determination of the coefficients  $A_i$ . The first one consists in measuring the strains in a relatively large number

of point  $N$  in the space, where large number means  $N \gg n$ . Or alternatively, the deformation is measured in a reduced number of points (typically 3) but the depth of the cuts is progressively increased. Both cases present advantages and disadvantages. In particular, with the first technique, due to the rapid decrease of the magnitude of the surface deformation away from the cut, only few points have a discrete sensitivity leading thus to a limitation on the number of functions used. In addition, the distribution of stresses is, at the end, determined only for a given depth. With the second technique, developed also by Schajer and Prime [96–99], a relative high number of experimental data is available but the maximum reachable depth is in the order of the hole diameter because the deeper the hole the smaller is the deformation induced on the surface.

The deformation recorded with one of the two methods can be expressed as function of the compliance matrix  $C_{ij}$  and the coefficient  $A_i$  of the Eq. (7.1) as follows:

$$\varepsilon_{measured}(\mathbf{x}_j; a) = \sum_{i=1}^n A_i C_i(\mathbf{x}_j; a) = C_{ij} A_i \quad (7.2)$$

where  $a$  is the hole/slit depth and  $\mathbf{x}_j$  is the position where the strains are measured. The matrix  $C_{ij}$ , whose columns vectors are  $C_i(\mathbf{x}_j; a)$ , expresses the deformation that a function  $P_i$  would generate if applied to the surface of the cut when its coefficient is set to 1. Nowadays  $C_{ij}$  is determined by FE simulations whereas in the past for known geometries tabular functions were available. The Eq.(7.2) can be inverted in a least square sense solving for the  $A$  coefficients:

$$(A) = \left( [C]^T [C] \right)^{-1} [C]^T \varepsilon_{measured} \quad (7.3)$$

This technique was extended in the case of a SFC with a diameter of 25mm having an axially located FBG by Colpo in [100, 101]. In his work, an incremental radial crack was introduced at the specimen middle plane and the changes in the fiber deformation state, generated during the grooving, were hence measured along the specimen's axis. (Fig. 7.1a). Legendre polynomials were used in the approximation of the stresses perpendicular to the cut while the  $C_{ij}$  matrix was determined using FE simulations.

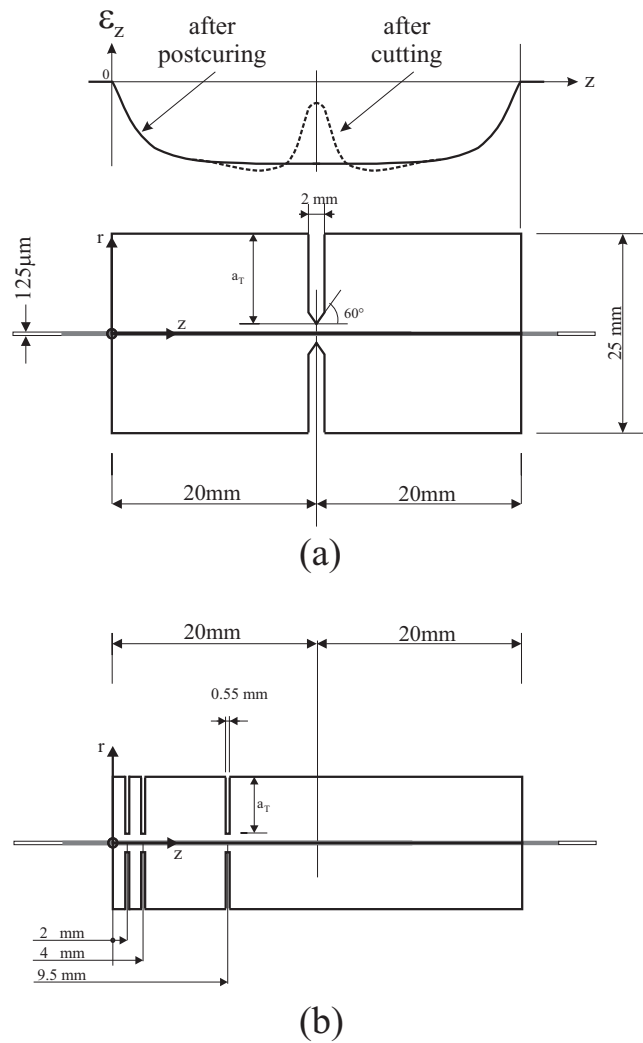


Figure 7.1: Radial cuts description: (a) Determination of  $S_f$  in Colpo et al. [100, 101], determination of  $S_f$  close to the edge using identification scheme (b).

Furthermore, the concept of the shrinkage function was introduced using a fracture mechanics approach in order to generalize the field determined for the SFC of 25mm. The results indicated that for a SFC having external radius of 6 mm (i.e. the present case) only a small radial dependency of the axial stresses  $\sigma_z(z = 20, r)$  is observed up until a distance of 40 fiber diameters from the SFC axis, i.e. the maximum cut depth. The shrinkage effect is thus introduced applying a volumetric deformation in the matrix constitutive equation:

$$\begin{pmatrix} \varepsilon_r(z, r) \\ \varepsilon_\theta(z, r) \\ \varepsilon_z(z, r) \\ \varepsilon_{rz}(z, r) \end{pmatrix}_m = \frac{1}{E_m} \begin{bmatrix} 1 & -\nu_m & -\nu_m & 0 \\ -\nu_m & 1 & -\nu_m & 0 \\ -\nu_m & -\nu_m & 1 & 0 \\ 0 & 0 & 0 & 2(1 + \nu_m) \end{bmatrix}_m \begin{pmatrix} \sigma_r(z, r) \\ \sigma_\theta(z, r) \\ \sigma_z(z, r) \\ \sigma_{rz}(z, r) \end{pmatrix}_m - S_f(z, r) \begin{pmatrix} 1 \\ 1 \\ 1 \\ 0 \end{pmatrix} \quad (7.4)$$

here the  $S_f$  is the shrinkage function and the subscript  $m$  indicates the matrix material. Taking advantage of the determined shape of  $\sigma_z(z = 20, r)$  the  $S_f$  was expressed as the product of two components, a radial expression  $R(r)$  and longitudinal one  $Z(z)$ :

$$S_f = Z(z)R(r) = [az^4 + bz^2 + c] [1 + d f(r)] \quad (7.5)$$

where  $a, b, c, d$  are constants. Note that the value of  $d$  is small compared to the other three. This expression is valid in the vicinity of the middle plane where the  $S_f$  function can be considered a good representation because of the symmetry. Moreover, close to the edges, this approximation could not be valid and the assumption of a minor radial dependency on  $r$  must be experimentally verified in that region. For this reason, a more realistic  $S_f$  representation is developed in the forthcoming sections by introducing multiple radial cuts at different distances from the specimen's edge (Fig.7.1b).

## 7.1.2 Inverse method approach

The C.C. method, outline briefly in the last section, has its weak point in Eq. (7.3) since the inversion of the product  $[C][C]^T$  results to be ill-conditioned. In this case a relatively small error in the measured strains is extremely amplified leading to large values of the  $A$  coefficients and thus to a solution that is globally oscillating. To solve this problem many recipes have been proposed that are based on the artificial regularization of the solution [102] imposing desired characteristic to it.

The problem was reported also by Colpo in [101]. However, a singular value decomposition of the matrix  $([C][C]^T)^{-1}[C]$  was successfully used in the case of a centrally located radial cut leading to a smooth solution for the radial evolution of  $\sigma_z$  at that location ( $\sigma_z(z = 20, r)$ ). In the present case, the cuts are machined close to the specimen's edge. This particular location, because of the complex residual stress field present therein, amplifies the ill-conditioning problem and no straightforward solution was found.

For this reason, an alternative approach was implemented. A new  $S_f$  is built in a general parametric form and used in the identification scheme where the cuts are reproduced in the FE model. The parameters are then identified in such a way that the measured strain change after a given cut depth is recovered. The objective is to extend the validity of  $S_f$  in the edge region and in particular at the fiber entry point.

### 7.1.2.1 Experimental procedure

The series of radial cuts at the  $z$  positions, reported in Fig. 7.1, is introduced using a lathe and a diamanted disk. The machining process was performed without water irrigation in order to avoid resin swelling. A low cutting speed was also used in order to limit the development of heat during the process. The cut depth,  $a_T$ , is increased by 1 mm at the time and after each cut the fiber deformation is retrieved using the OLCR apparatus. It was found that the strain difference recorded was not remarkable up until a depth  $a_T = 5.5$  mm suggesting that even in this region for  $a_T \leq 5$  mm the radial dependency is not dominant. The recorded fiber strains, after each cut reached the maximum depth, are reported in Fig.7.2 together with the reference curve recorded



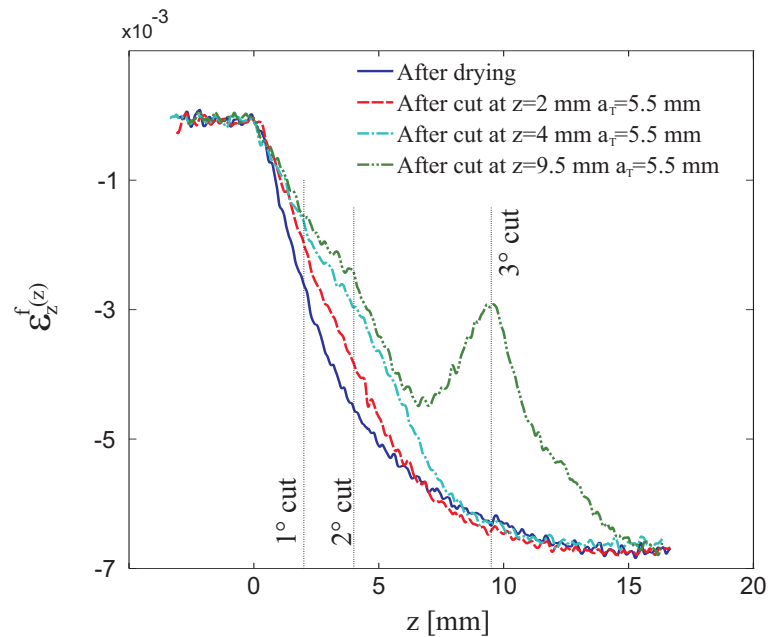


Figure 7.2: Axial strains evolution after 3 sequential cuts at 2mm 4mm and 9.5mm from the edge.

before cutting. It can be noticed that a peak of strain release is developed in correspondence to the cut position in all the studied configuration. The strain difference between each curve is also reported in Fig.7.3.

### 7.1.2.2 Shrinkage function

The mathematical description of the new shrinkage function was chosen in such a way to build a general function able to represent the physics of the problem as well as to introduce a clear coupled dependence in the  $r$  and  $z$  directions. In addition, the following problem is addressed: based on the CCM nothing is known about the stress state in the radial range  $a_T \leq r \leq rf$ . To solve this issue the hypothesis that no shrinkage is developed at the fiber matrix interface is made.

The chosen evolution of the shrinkage function is of an arctangent type:

$$S_f = A + B \arctan(\eta r) \quad (7.6)$$

where  $A$  and  $B$  are the shift and magnification factors respectively,  $\eta$  represents the slope of arctan function at the flex point. These parameters are functions

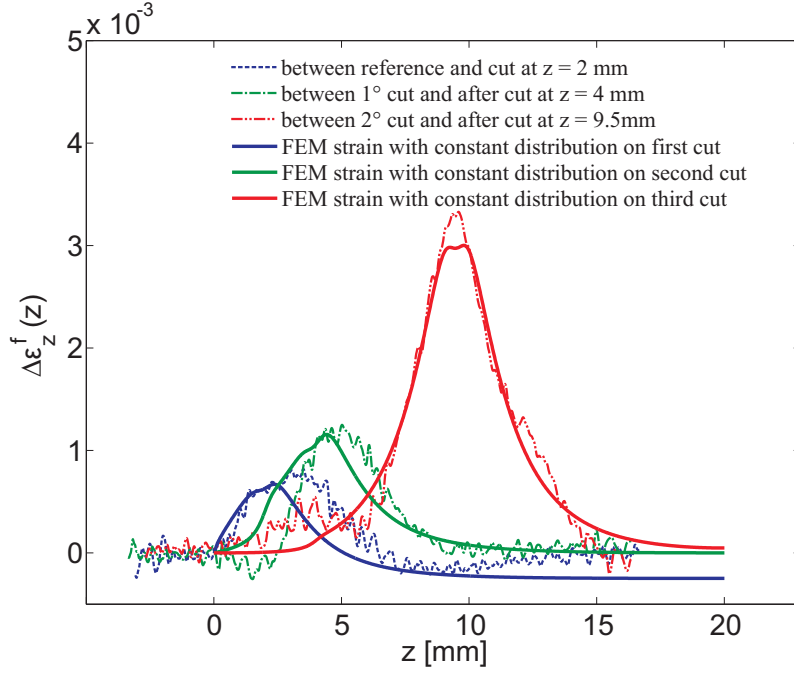


Figure 7.3: Strain difference after each cut.

of the  $z$  coordinate and are determined imposing the following conditions:

$$\begin{cases} S_f(r = r_f) = 0 \\ S_f(r = 6) = T_{R6}(z) \end{cases} \quad (7.7)$$

where  $T_{R6}$  is a function of  $z$  that expresses the axial evolution of the  $S_f$  at  $r = 6$  mm. The Eq. (7.7) leads to:

$$\begin{cases} A = B \arctan(\eta r_f) \\ B = \frac{T_{R6}(z)}{\arctan(6\eta) - \arctan(\eta r_f)} \end{cases} \quad (7.8)$$

The polynomial form used in the previous study [100, 101] is used in the expression of  $T_{R6}$ :

$$T_{R6}(z) = A_{TR6}z^4 + B_{TR6}z^2 + C_{TR6} \quad (7.9)$$

where the parameters  $A_{TR6}$ ,  $B_{TR6}$ ,  $C_{TR6}$  are related to the  $S_f$  value at the middle plane, called  $T_{R6Z20}$ , its value at the edge,  $T_{R6Z0}$ , and its slope at the edge,  $dT_{R6Z0}$ , as follows:

$$\begin{cases} T_{R6}(z = 20mm) = T_{R6Z20} \\ T_{R6}(z = 0) = T_{R6Z0} \\ \left. \frac{dT_{R6}}{dz} \right|_{z=0} = dT_{R6Z0} \end{cases} \quad (7.10)$$

Furthermore, the radial position at which the arctan reaches the arbitrary value of 90% of its horizontal asymptote is called  $R_{0d9}$ . The latter condition inserted in Eq. (7.6) gives:

$$\eta = \frac{\tan\left(\frac{\pi}{2}0.9\right)}{R_{0d9}} \quad (7.11)$$

In summary, the  $S_f$  is governed by 4 parameters  $T_{R6Z20}$ ,  $T_{R6Z0}$ ,  $dT_{R6Z0}$ ,  $R_{0d9}$  having the reported easy-to-see physical meaning ( cfr. Fig. 7.5).

### 7.1.2.3 Parameters identification

The challenge in the identification of the parameters defining the  $S_f$  is represented by the necessity to reproduce the different deformations reported in Fig.(7.2) with a single function. In addition, once the shape of the  $S_f$  is established, it must be able to be calibrated only with the strain curve in after post-curing conditions.

To achieve this objective 3 FE models were prepared and run sequentially in a single identification loop. The first one represents the intact geometry aimed at reproducing the after drying curve in Fig.7.2, the second presents the SFC geometry with a radial cut at  $z = 2mm$  and  $z = 4mm$  in order to reproduce the curve after the introduction of the second cut, and, the third one with the addition of the cut at  $z = 9.5mm$  aimed at reproducing the last set of data.

At each iteration loop in the identification process, the  $S_f$ , defined by a given set of parameters, is applied to the three FE models by solving Eq. (7.4). The generated fiber deformations in the 3 cases constitute the single column vector  $\mathbf{o}_k$  in the Eq.(2.28) as follows:

$$\mathbf{o}_k = \begin{bmatrix} (\varepsilon_z^f(z)_{intact\ model}) \\ (\varepsilon_z^f(z)_{first\ 2\ cuts}) \\ (\varepsilon_z^f(z)_{3\ cuts}) \end{bmatrix} \quad (7.12)$$

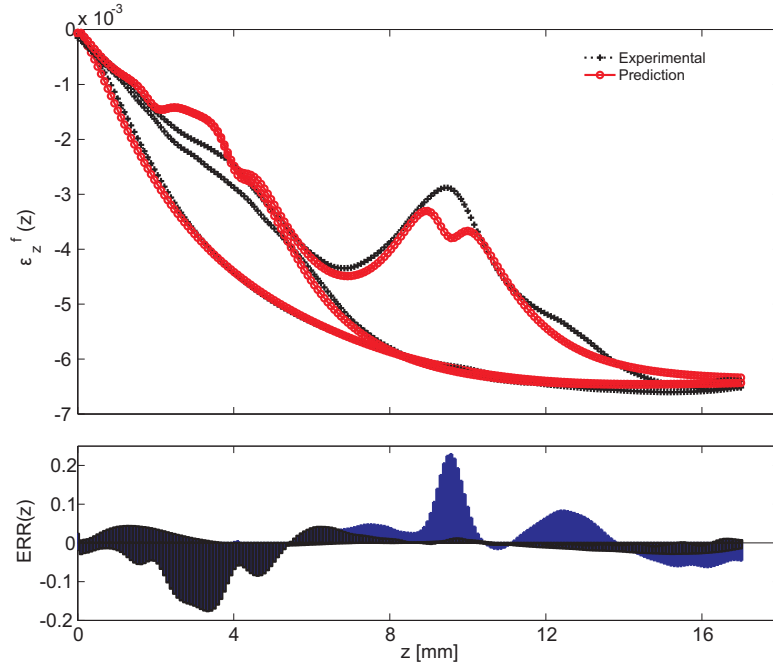


Figure 7.4:  $S_f$  identification results.

In the same way the reference vector  $\mathbf{h}$  in Eq.(2.27) is given by the corresponding experimental data reported in Fig.7.2. The results of the identification process are reported in Fig. 7.4 together with the error committed by the approximation. It can be noticed that the residual strains in the intact configuration are perfectly approximated while the deformation induced by the presence of the cuts shows zones of relatively high error (close to 20%). However, the main features recorded are clearly distinguishable in the simulated results. The identified parameters are reported in Table 7.1 whereas the final shape of the  $S_f$  is reported in Fig. 7.5 together with the physical indication of the controlling parameters.

On the basis of a sensitivity analysis of the convergence rate, the parameter  $R_{0d9}$  was found to be the most sensitive during the identification. In the light of that, this parameter was fixed in the identification of the  $S_f$  on the basis of the only after drying curve. The results of this identification, shown in Table 7.1, indicate very small difference in the parameters  $T_{R6Z20}$  and  $dT_{R6Z0}$ , 1.3% and 9% respectively, showing that with  $R_{0d9}$  fixed it is indeed possible to calibrate the  $S_f$  function based on the after postcuring curve only.

The values obtained by calibrating the  $S_f$  (with the parameter  $R_{0d9}$  fixed)

Table 7.1:  $S_f$  identified parameters.

	$T_{R6Z20}$	$T_{R6Z0}$	$ dT_{R6Z0} $	$R_{0d9}$
Identification on 3 cuts	$6.563 \times 10^{-3}$	$1.347 \times 10^{-3}$	$1.486 \times 10^{-3}$	1.915
Identification on the ref. curve	$6.651 \times 10^{-3}$	$9.270 \times 10^{-5}$	$1.621 \times 10^{-3}$	fixed
Calibration on aged SFC1	$5.858 \times 10^{-3}$	$3.878 \times 10^{-4}$	$1.804 \times 10^{-3}$	fixed
Calibration on aged SFC2	$6.043 \times 10^{-3}$	$3.011 \times 10^{-3}$	$5.250 \times 10^{-4}$	fixed

on two of the aged samples are also reported in Table 7.1.

## 7.2 Hygroscopic deformation

In order to carry out the hygromechanical stress analysis of the SFC specimen the hygromechanical expansion of the resin is needed. The determination of this parameter is obtained by monitoring the expansion of 4 SFC cells during the absorption process, using the OLCR. As soon as the SFC specimens are immersed in the water bath they start to expand, firstly because of the temperature difference and secondly because of water absorption. Since the time to thermal equilibrium is estimated at  $\sim 15$  min, a time much shorter than the characteristic time for diffusion ( $t \sim 1/D$ ), it is assumed that, at the onset of thermal equilibrium, the strains due to the moisture absorption are negligible.

Typical LBW data as a function of immersion time are shown in Fig. 7.6, with the reference curve at zero time taken as the one corresponding to thermal equilibrium at  $50^\circ\text{C}$ . From this point on the specimen is in isothermal condition and all modifications in the strain state are due to the epoxy's swelling as the water enters the specimen. The longitudinal strains on the FBG due to moisture absorption of the epoxy are calculated using Eq. (7.13) obtained from Eq. (2.12) since the only hygric component is non zero at the second member in the latter equation. The calculated values are shown on the right hand axis

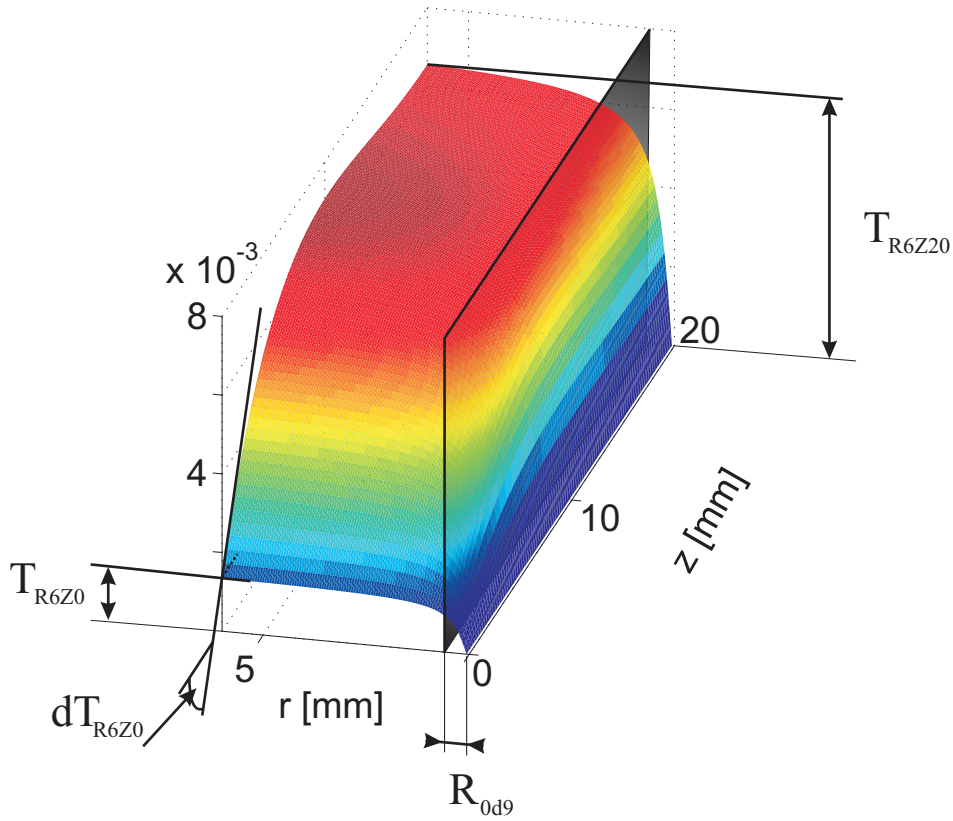


Figure 7.5: Identified shrinkage function. The subscripts in the indicated parameters have the following meanings:  $R_6$  indicates that the parameter refers to  $r = 6$  mm,  $Z_0$  and  $Z_{20}$  indicate that the corresponding parameter is calculated at  $z = 0$  mm or  $z = 20$  mm respectively,  $_{0d9}$  indicates that the values correspond to 90% of the horizontal asymptote of the arctan function.

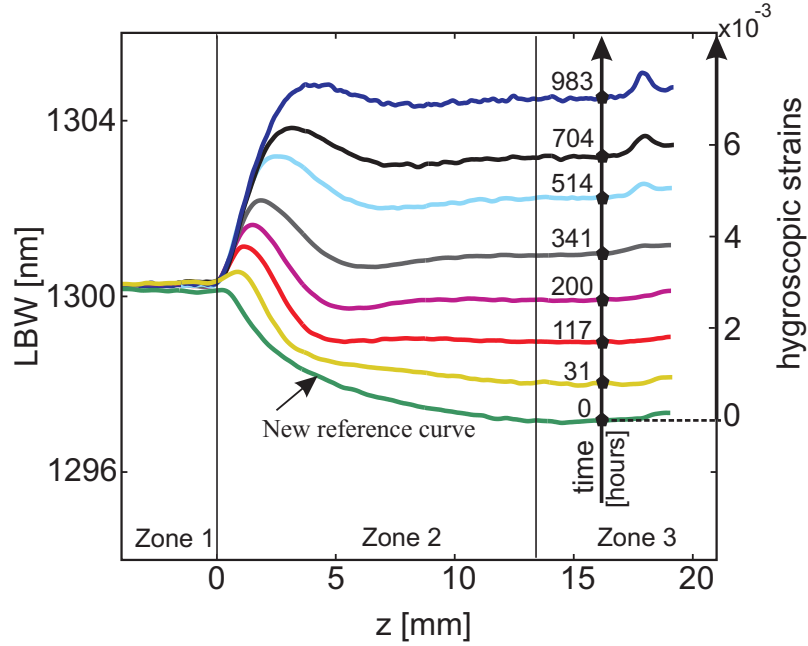


Figure 7.6: Local Bragg wavelength and the corresponding evolution of hygroscopic strains.

in Fig. 7.6:

$$\frac{\lambda_{B1} - \lambda_{B0}}{\lambda_{B0}} = (1 - p_e) \varepsilon_z^h = (1 - p_e) \beta_m \bar{c}(t) \quad (7.13)$$

Here, the first measurement at  $z \geq 16$  mm after thermal equilibrium is used as new reference wavelength (point denoted  $t = 0$ ). Note that *Zone 2* becomes smaller and *Zone 3* longer since water absorption reduces the effect of the specimen's edge on the non-homogeneous strains along the FBG. Moreover, in *Zone 3* (Fig. 7.6) the specimen is in an isostrain condition and behaves as an infinitely long cylinder with a centrally embedded fiber. Thus, the strain evolution with time in this zone is independent of the specimen's free ends and represents the epoxy's expansion due to water uptake in  $2D$  axisymmetric conditions as demonstrated in Section 2.2 and reported in [103]. Interestingly, the increase in strain at  $z = 16$  mm after 983 hrs of immersion, is about 7 times greater than the strain upon thermal equilibrium at  $50^\circ\text{C}$  taken as reference. The difference become even higher over time and the fiber, in every specimen tested, not withstanding such high strains, fractures at a distance of  $\sim 11.5$  mm from the entry point (Ch. 8). Thus no strain data from the FBG sensor

are reported beyond this point in time.

### 7.2.1 Coefficient of moisture expansion

Generally, the hygric strains are modeled as a product of CME,  $\beta_m$ , and the difference of moisture concentration with respect to the reference state. Namely, for an isotropic material,  $\beta_m$  is related to the average, one dimensional hygric strain,  $\varepsilon_z^h$ , and the average moisture content  $\bar{c}(t)$  by the hygromechanical expansion relation  $\varepsilon_z^h = \beta_m \bar{c}(t)$ . Note that the conventional definition assumes that  $\beta_m$  is constant and  $\bar{c}(t)$  is uniform through the specimen [21, 104, 105]. However, for a specimen immersed in water, uniform moisture content is not possible to realize experimentally except at the saturation point. Moreover, as indicated in [103] and verified here experimentally,  $\beta_m$  is a function of the concentration complicating further the calculations. In this work firstly, the conventional definition  $\varepsilon_z^h = \beta_m \bar{c}(t)$  is used to estimate a concentration dependence based on hygric strains and moisture concentration measurements. Secondly, the derived hygromechanical expansion relations are used in simulating the axisymmetric diffusion – hygromechanical stress problem (Section (7.2.2)). Thirdly, the simulation results are compared with the FBG measurements to corroborate on the validity of the hygromechanical expansion relations. As described below, two sets of experimental data are used to estimate the CME.

The data in Fig.7.6 demonstrate that the specimen is subjected to homogeneous strains for  $z > 7$  mm (i.e., *Zone 3*). Considering an isostrain condition after that distance the fiber and epoxy are subjected to nearly equal axial strains. Thus, using the experimental measurements of  $\lambda_B$  (Fig.7.6) and  $\bar{c}(t)$  (Fig. 5.2), as well as the known values of  $p_e$  and  $\lambda_{B0}$  at thermal equilibrium, the epoxy hygric strains in *Zone 3*, are expressed by the left hand side of Eq. (7.13) divided by  $(1 - p_e)$ . These strains are plotted in Fig. 7.7 against moisture content  $\bar{c}(t)$  for all four SFC specimens containing an FBG. Note here the excellent reproducibility and practically zero scatter of the FBG data among all the SFC specimens. It is mentioned earlier, that the glass fibers, in every specimen used, fractured at about the same length from the entry point and at the same moisture content of  $\bar{c}(t) \sim 0.045$ . Accordingly strain data from the FBGs beyond this point are not available. The strain data from the FBG sensors in Fig. 7.7 indicate a clear non-linear trend demonstrating that  $\beta_m$ , the



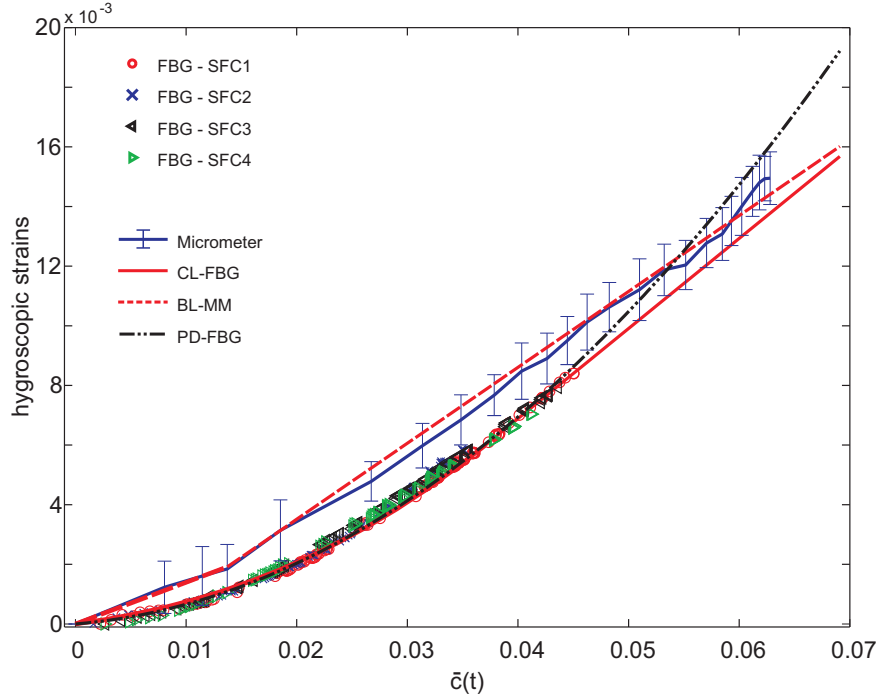


Figure 7.7: Hygroscopic strains as function of water concentration.

slope of the curve defined by the data, is a function of the water content: for concentration values greater than  $\bar{c}(t) = 0.037$  the strains appear to be linearly related to the concentration whereas, for smaller values, the non-linearity of the data is evident.

In order to obtain an average strain due to water uptake, the length between the ends of selected cylindrical specimens (A & B, Fig.7.8) is monitored using a manual micrometer with a resolution of  $2\mu\text{m}$ . This method represents the conventional way [104,105] of measuring the specimen's elongation due to water absorption and is used here to compare the results with the ones obtained with the embedded FBG sensors. The error in such measurements, attributed to the uncertainty in the length measurements on the strain equation  $\varepsilon_l = (l(t) - l_0) / l_0$ , is expressed as,

$$\delta\varepsilon(t) = \left| \frac{\partial\varepsilon(t)}{\partial l(t)} \right| \delta l(t) + \left| \frac{\partial\varepsilon(t)}{\partial l_0} \right| \delta l_0 \quad (7.14)$$

where  $l(t)$  is the longitudinal length at time  $t$  and  $l_0$  is the initial length, both measured at room temperature, upon removal of the specimen from the water bath;  $\delta l(t)$  and  $\delta l_0$  are the corresponding standard deviation of 5 measurements.

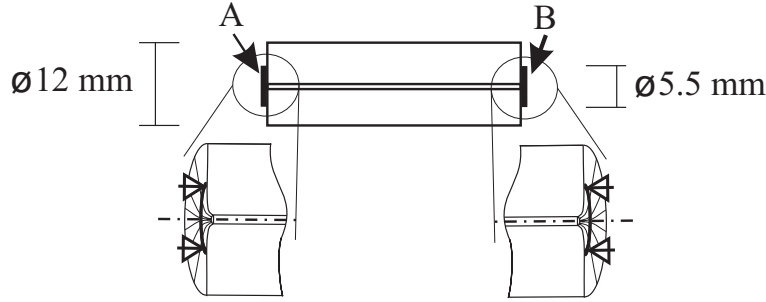


Figure 7.8: Micrometer measurement locations.

The longitudinal strain  $\varepsilon_l(t)$  is evaluated using the mean value of the length measurements and the calculated error from Eq.(7.14) as  $\varepsilon_l(t) = \varepsilon_l^m(t) \pm \delta\varepsilon(t)$ .

Also displayed in Fig. 7.7 are the strain data obtained from micrometer measurements. The error bars, based on standard deviation of five measurements, calculated using Eq.(7.14) indicate errors in the range of  $800\mu\varepsilon$  to  $1000\mu\varepsilon$ . The error diminishes with time because the strains become more uniform along the cylinder due to water uptake. Note here that the data obtained with micrometer length measurement clearly show two linear trends before and after  $\bar{c}(t) = 0.015$ .

It should be emphasized that moisture absorption takes place below  $T_g$  for at least up to  $\bar{c}(t) = 0.035$ . This assertion is based on a  $T_g = 80^\circ\text{C}$  (postcuring temperature of  $70^\circ\text{C}$  plus  $10^\circ\text{C}$ ) before immersion in the water bath and assuming that 1% moisture mass absorption reduces  $T_g$  by  $10^\circ\text{C}$  [85]. This corresponds to a worse case estimation with respect to what determined in Section 6.4 for the material under study. For a  $\bar{c}(t) = 0.035$ , corresponding to  $w_g = 0.030$  (Eq. (5.8)), the  $T_g$  should be around  $50^\circ\text{C}$ . Thus the observed nonlinearity in Fig.7.7 is not due to the specimen being above  $T_g$ .

In view of such experimental data a linear dependence of the hygric strains on  $\bar{c}(t)$ , or a constant  $\beta_m$ , is not realistic to assume during the entire process of moisture absorption. Thus, the following dependencies of on moisture are considered in the coupled numerical analysis for the strains in the SFC specimen:

1. Based on the experimental data from the FBG sensor, a cubic evolution of the hygric strain on  $\bar{c}(t)$  for  $\bar{c}(t) \in [0, 0.037]$  followed by a linear dependence for  $\bar{c}(t) \in [0.037, 0.069]$  is assumed. Here the tangent value,

i.e. the CME, is moisture dependent initially (quadratic) and constant afterwards. Both curves have equal tangent at  $= 0.037$ . This hygromechanical expansion relation is labeled as (CL-FBG).

2. On the basis of the FBG data, a parabolic dependence is considered between the hygric strain and  $\bar{c}(t)$  for  $\bar{c}(t) \in [0, 0.069]$  labeled as (PD-FBG). Here  $\beta_m$  is moisture dependent though out the process (linear evolution of  $\beta_m$ ).
3. Using the strain data from the micrometer measurements, a bilinear dependence of hygric strain on  $\bar{c}(t)$  in two intervals  $[0, 0.014]$  and  $[0.014, 0.069]$  is considered. This relation is labeled as (BL-MM).

Therefore, the moisture content at each point in the specimen is obtained from the diffusion analysis (Section 5). With the moisture concentration known, the three hygromechanical expansion relations reported above are used to calculate the local hygric strains at every point of the SFC specimen in the FE model. To check the validity of the estimated hygric expansion relations, the variable CME is inserted into a hygro-mechanical model to calculate the strain in *Zone 3* of the specimen or the average strain of the entire specimen.

### 7.2.2 Hygroelastic model

The coupled hygro-mechanical model used in order to investigate the influence of the non uniform concentration field on the stresses induced by moisture absorption is presented. The following elasticity equations are solved simultaneously with Eq. (5.4)

$$\boldsymbol{\sigma} = \mathbf{C}(\boldsymbol{\varepsilon} + \beta_m s c^* \mathbf{I}) \quad (7.15)$$

Here  $\boldsymbol{\varepsilon}$  and  $\boldsymbol{\sigma}$  are the strain and stress tensors,  $\mathbf{C}$  and  $\mathbf{I}$  are the elasticity and identity tensors and  $\beta_m$  is the epoxy's CME. In all simulations, the matrix diffusivity  $D$  in Eq. (5.4) is taken as a linear function of the concentration while the fiber's diffusivity is set equal to zero. In Eq.(7.15), the SM and LM Young's moduli for the epoxy are taken from Fig. 6.3 and the Poisson's ratio is assumed as  $\nu_m = 0.38$ . For the glass fiber the corresponding parameters are  $E_f = 72$  GPa and  $\nu_f = 0.19$ .

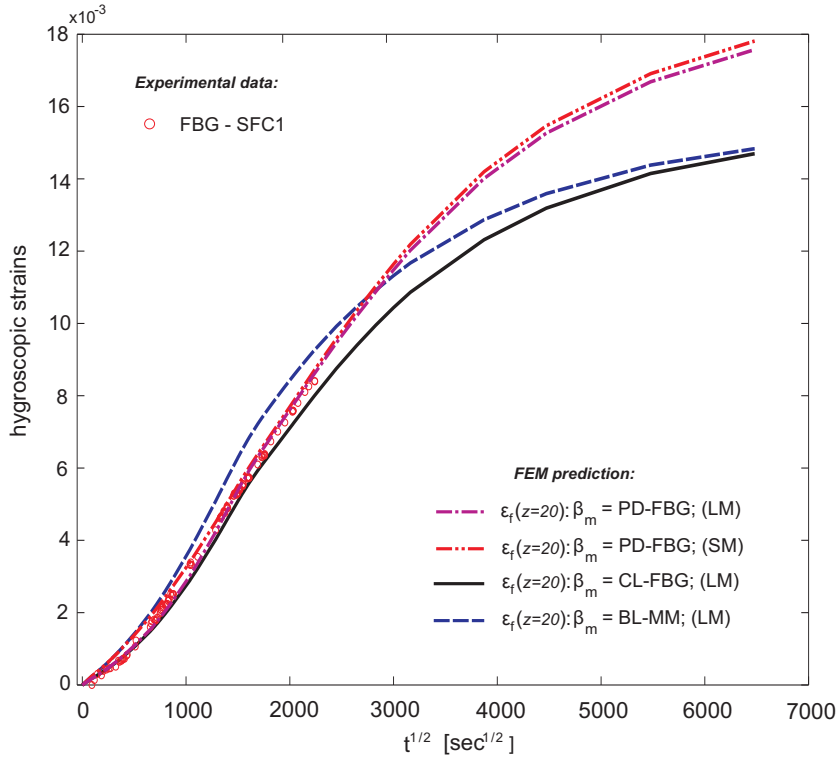


Figure 7.9: Evolution of the hygroscopic strain predicted by the coupled hygroelastic model as function of the different hygroscopic expansion laws.

The evolution of the simulated strain in Zone 3 of the SFC specimen as a function of  $t^{1/2}$  is shown in Fig.7.9 for the three different cases of three hygromechanical relations listed above. Also shown in Fig.7.9 are the experimental data from the FBG sensor (specimen SFC1).

While all the simulated strain evolutions match fairly well the experimental data measured with the FBG until its fracture ( $\bar{\epsilon}(t) \simeq 0.045$ ), the curve corresponding to BL-MM (case 3) indicates an error in the range of 5 to 15% from the experimental data after  $t \sim 10^6$ sec. This discrepancy is attributed to the relatively larger uncertainty on the average strain measurements from the micrometer. Moreover, the measurement errors committed with a micrometer are systematically biased towards higher values because of surface curvature and alignment uncertainties, thus it is to be expected that the micrometer based strain measurements are systematically higher than the actual values. Although, the experimental data are not available until the saturation point, the parabolic fit PD-FBG (case 2) seems to overestimate the hygroscopic strain

evolution at long immersion times. This argument is based on the trend of the strain data from the micrometer, which despite the measurements error, indicate a realistic trend towards the saturation point. Alternatively, the simulated strains based on the CL-FBG (case 1) describe well the experimental FBG measurement and have a similar trend towards saturation as for the BL-MM curve. With respect to the effects of the moduli, i.e., SM or LM, it is found that they are insignificant in all cases of CME used. Typical results for PD-FBG (case 3) are presented in Fig. 7.9. Such response is due to the large difference in the stiffness between the epoxy cylinder and that of the fiber. This assertion can be corroborated if we consider the longitudinal strain in the central part of a long cylindrical epoxy specimen with a centrally located glass fiber subject to a uniform temperature change  $\Delta\theta$  (or uniform moisture concentration change  $\Delta\bar{c}$ ). As demonstrated, such strain is a function of the stiffness ratio  $k = \frac{A_m E_m}{A_f E_f}$  ( $A_m, A_f$  being the cross sectional areas of the epoxy and fiber) and  $\Delta\theta$ . The aforementioned stiffness ratio for the geometry used here and result in a strain difference of 2% when the  $E_m$  takes the ST and LM values of 0.8 and 0.35 GPa (Fig. 6.3), respectively.

The simulated average axial strains in the entire cylindrical SFC specimen due to water absorption for the three relations of the CME listed above are compared to the experimental micrometer measurements in Fig.7.10. As expected the simulated average axial strains when the CME is taken from BL-MM (case 3) are very close to the measured ones. However, the simulated strains, when the CME is taken from the CL-FBG (case 1), are systematically below the experimental measurements. As in the case of the data in Fig.7.9, this is attributed to the relatively large experimental error and the systematic bias in the micrometer measurements. The strains from the simulations when the CME is taken from the PD-FBG (case 2) predicts relatively high strains after  $9 \times 10^6$ sec. and is considered unrealistic for the same reasons stated earlier. Alternatively, the simulated average strains in the specimen based on the CME from the CL-FBG (case 1) relation are more precise and give close results to those obtained using the micrometer based BL-MM CME relation. Interestingly, close to the saturation point, both approximations of the CME (CL-FBG case 1; BL-MM case 3) predict similar strains evolution. Overall, the predictions based on the CL-FBG hygromechanical expansion relation are

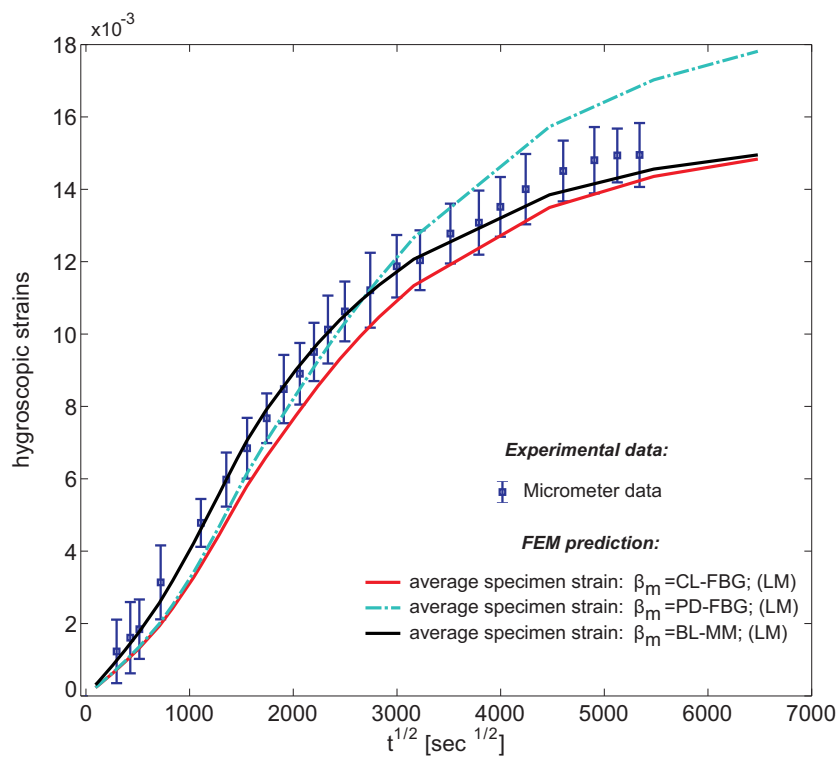


Figure 7.10: Comparison of the predicted hygroscopic strains evolution with the experimental micrometer data.

in good agreement with both the axial strain in Zone 3 measured with FBG and the averaged strain measured with a micrometer (Figs. 7.9 and 7.10, respectively). Moreover, owing to the very small scatter and uncertainties in the FBG data on which it is based, the CL-FBG relation is considered the most appropriate and accurately represents the hygromechanical response of the epoxy resin studied in the present work. It has been shown by the present investigations that:

1. The proposed method using an embedded FBG for measuring the CME leads to reproducible and accurate results. This is due to the fact that the FBG possesses a self referencing capability because the signals are decoded in the wavelength domain. This characteristic leads to very precise measurements as demonstrated by the reproducibility of the experimental results in four specimens.
2. It is demonstrated that the CME is a concentration dependent parameter. Thus a single constant CME does not describe the physical process properly. However, the exact nature of the dependence during the entire moisture absorption is not fully established here because of fiber's fracture inside the specimen due to the high hygric strains and possible weakening in the fiber due to the FBG inscription.
3. The experimental data suggest that the hygromechanical strain can be described initially by a cubic form followed by a linear dependence on moisture content. In other words, the tangent CME as a function of concentration appears to follow first a quadratic progression up to  $c \simeq s/2$  and then stabilizes to a constant value until the concentration reaches the saturation.

### 7.3 Residual-thermo-hygric model

In order to study the evolution of the initial residual stress state, determined in Section 7.1, as heat and water diffuse during ageing, and the fiber fracture and debonding processes, the information obtained so far has to be integrated in a single FE model.

For this purpose an user subroutine UEXPAN had to be coded since the original Abaqus software does not allow to integrate the inelastic residual deformation neither the simultaneous diffusion of temperature and humidity.

The UEXPAN subroutine is used to define incremental strains,  $\Delta\varepsilon$ , as function of temperature, predefined variables and state variables [106]. According to the Abaqus Manual, “the subroutine is called at all the integration points of elements for which the material behavior contains user-subroutine-defined thermal expansion”. “It is called twice per material point in each iteration during a coupled temperature displacement analysis”.

Taking advantage of the formal identical mathematical description of the heat and moisture diffusion equations the UEXPAN subroutine has been generalized as follows. First a temperature surrogate,  $\Theta$ , is introduced as state variable. As reported in Fig. 7.11 it assumes different meanings depending on which simulation step is taken into consideration. In fact, during the water diffusion step it represents the normalized water concentration  $c^*$  in the Eq. (7.15). Whereas, during the heat diffusion it represents the actual temperature  $T$  in the equation

$$\nabla^2 (T) = 0 \quad (7.16)$$

During the “pre-step1” and in “step1”,  $\Theta$  has not a physical meanings and constitutes a handy state variable.

The 3 computation steps can be described as follows:

**1. step1: Residual stress development:**

The shrinkage function is introduced calling the subroutine UFIELD, that calculate the  $S_f$  at each point, from the UEXPAN and the Eq. (7.4) is solved.

**2. step2: Heat diffusion:**

The substantial time scale decoupling between the heat and moisture diffusion is exploited to calculate the thermal expansion in a separated step. The experimentally determined CTE is used to solve the coupled temperature-displacement equation



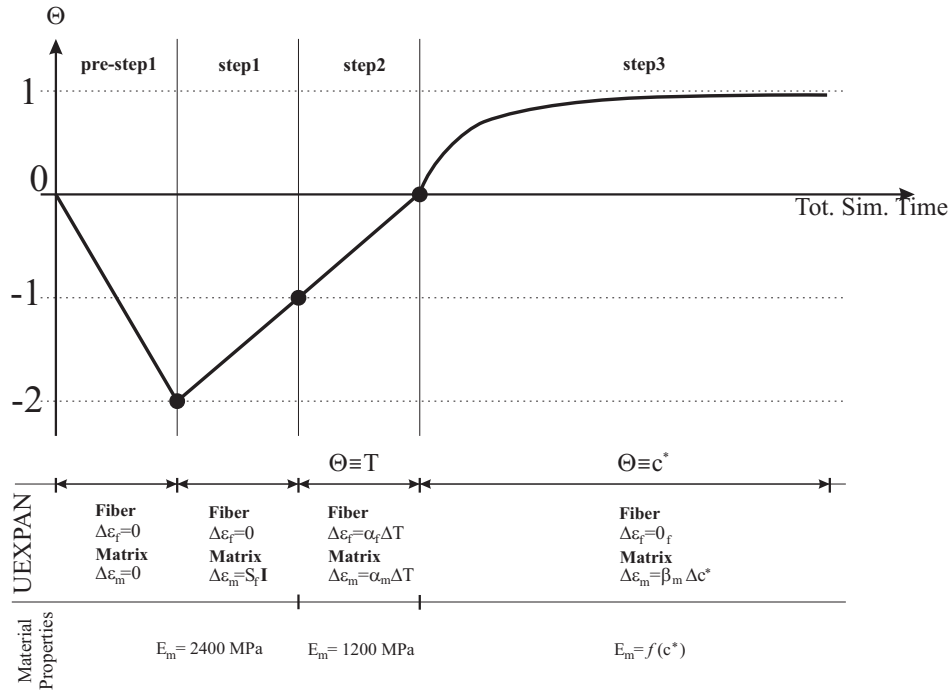


Figure 7.11: UEXPAN subroutine description.

$$\boldsymbol{\sigma} = \mathbf{C} (\boldsymbol{\varepsilon} + \alpha_m \Delta T \mathbf{I}) \quad (7.17)$$

where  $\Delta T = 25 \text{ }^\circ\text{C}$  and  $\mathbf{C}$ ,  $\boldsymbol{\varepsilon}$ ,  $\mathbf{I}$  are the compliance, deformation and identity tensors.

### 3. step3: Transient moisture diffusion step:

The hygric expansion is calculated at each time increment using one of determined CME laws and solving the Eq. 7.15. In particular, the results reported in the following are obtained using the parabolic dependency for the CME.

The variable  $\Theta$  is used also to modify the material properties of the resin according to what found in Chapter 6.

#### 7.3.1 Elastic model results

The fiber axial deformation is calculated and compared to the one recorded experimentally. The results are reported in Fig.7.12 where the good global

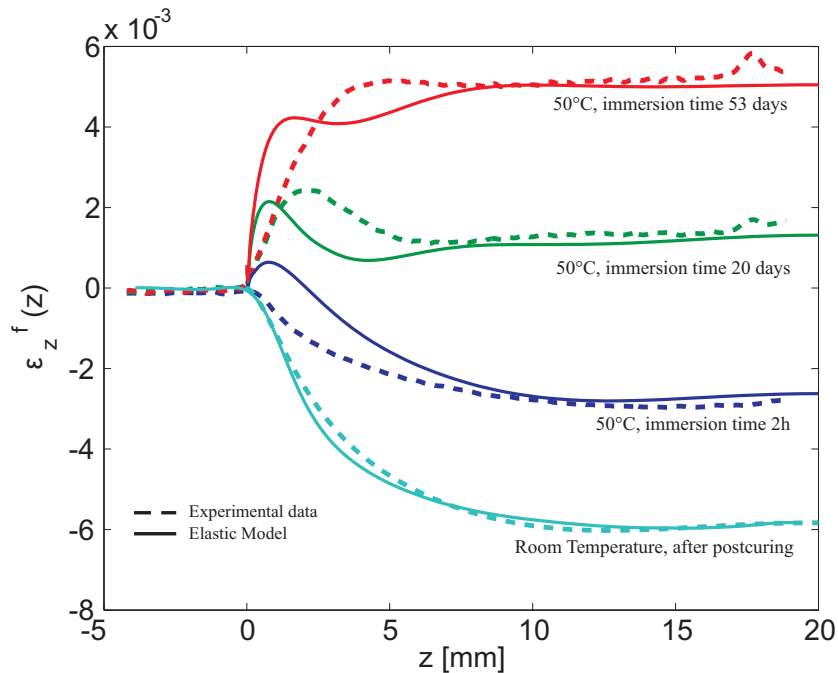


Figure 7.12: Experimental fiber strains and prediction obtained with the residual-thermal-hygro model.

agreement between experimental and simulated results can be noticed. Moreover, the accuracy of the predicted fiber deformation at the specimen's zone 3 is confirmed whereas a certain discrepancy around the specimen entry point can be distinguished. In particular, the deformation gradient appears to be steeper in the simulations as compared to the experimental data. Several reasons can be the cause of this behavior. The possibility of damage at the fiber/matrix entry point, errors in the representation of the residual stress field, and probably the approximation with a pure elastic behavior of the matrix are possible explanations. However, the global characteristics of the experimental curves are reproduced since the initial strain peak, developed during ageing, appears earlier and only displaced towards the external part of the specimen.

### 7.3.2 Elastoplastic model

In order to investigate the influence of the plasticity on the model results and in particular on the strain gradient at the entry point, Von Mises plasticity is added to the material constitutive law. In particular, the plastic stress-strain

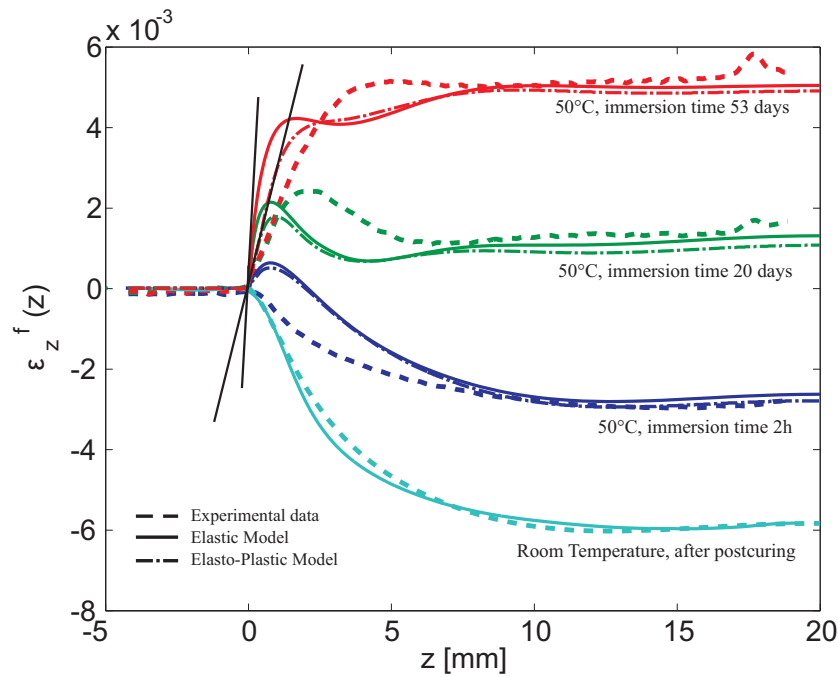


Figure 7.13: Comparison between elastic and elasto-plastic model predictions.

description as function of  $c^*$  was obtained from the tensile tests results reported in Fig. 6.2.

The results (Fig.7.13) indicate that the plasticizing effect suddenly introduced by the water absorption strongly affect the fiber deformation gradient at the entry point. On the other hand, the fiber deformation at the inner plateau is only minimally affected. It can be concluded that a greater part of the discrepancy in zone 2, noticeable in Fig. 7.12, is due to the inappropriate full elastic representation of the matrix.



# Chapter 8

## Ageing induced damage

The progressive decrease of the material properties and the increasing expansion of the resin, that accompanies the water diffusion, transform the residual stress state stored into the single fiber composite. The deformation state on the fiber passes from completely compressive to completely tensile with a total variation greater than  $12000\mu\varepsilon$  in the middle plane of the specimen. This imposed deformation is sufficient to introduce a fiber fracture and, depending on the time at which it takes place, evolves into progressive debonding at the fiber-matrix interface. Longer time of exposure results in a progressive degradation of the interface that, notwithstanding the load imposed, breaks generating progressive debonding starting from the fracture location and from the fiber-matrix entry point. Conversely, if the fiber fracture occurs at lower diffusion time, the load is continuously transferred to the fiber without generating immediate debonding.

In this chapter the fiber fracture event is treated firstly according to the Linear Elastic Fracture Mechanics (LEFM) in order to identify the principle mode of fracture acting at interface crack tip. Secondly the information retrieved is used for the simulation of the debonding process by a cohesive-elements modeling approach.

### 8.1 Fiber fracture

In general, optical fibers used in telecommunications exhibit Young's modulus  $E \sim 72$  GPa, elongation at break of  $4.5 \div 5\%$ , and ultimate tensile strength

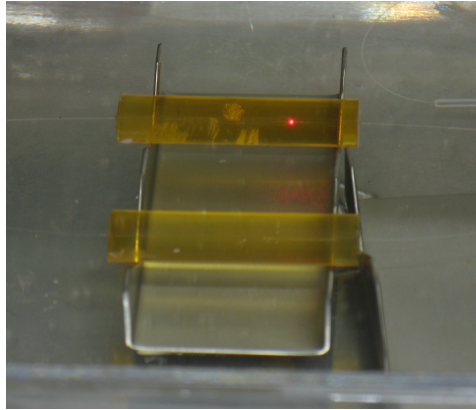


Figure 8.1: Fiber failure evidence.

$\sigma_u \sim 3.6 \div 6$  GPa [107]. These data refer to the virgin state at room temperature. It is well known that these characteristics decrease with high temperature and humidity, especially if the fiber is simultaneously subjected to mechanical loads. In particular, corrosion cracking and creep can lead to a premature failure of the filament [14–16, 108]. Moreover, the inscription of FBGs lowers the mechanical response of the fiber at that point because of the introduction of a higher subcritical crack density region during the fiber irradiation [109]. It has been found by Varelas [109] that ultimate strength of the fiber before irradiation is reduced to one fourth of its original value by inscription of a 4mm FBG. In addition, the decrease is a moderate function of the FBG length.

In the present case, all the elements previously reported are synergistically present. In fact, the fiber constantly sustains mechanical load, firstly compressive and then tensile, for a long period of time (more than 1 month), the environment is relatively hot and the surrounding resin increases its level of humidity with time. Finally, the inscription of a long FBG,  $\sim 24$ mm, appeared to be determinant in causing the fiber fracture process since all the failure loci appeared inside the gage length.

The failure event was clearly distinguishable in the OLCR data because of a sudden jump in the measured OLCR phase signal always located at about the same  $z$  position. It indicates that the correlation between the reference arm and the test arm is lost at one point. This evidence is corroborated by visual inspection when redlight is injected into the fiber, as reported in Fig.8.1.

The evolution of the fiber deformation state for one of the specimens is

reported in Fig. 8.2a & b. In this case, after  $\sim 27$  days of immersion a fiber fracture appeared at  $z \cong 11.4$  mm. Interestingly, at this early stage of diffusion, the interface still has a sufficient strength to transmit the expansion strain from the matrix to the fiber. In fact, both sides of the fracture are subjected to an increasingly tensile deformation caused by the progressive swelling of the matrix (Fig. 8.2a). Moreover, an extensive interface damaged at the specimen entry point (Fig. 8.2b), triggered by the high water concentration therein present, is established leading to a progressive fiber-matrix debonding. Notice also that on the right hand side of the fracture, where no debonding is visible, the deformation increases progressively up to  $\sim 5500\mu\varepsilon$ .

### 8.1.1 Shear lag analysis

The strain plateau reached on the right hand side of the fiber fracture (Fig. 8.2b) for every absorption time suggests that the stress transfer in this zone can be modeled using the shear lag approximation. Using the notation reported in the description of the model in Section 2.2.1.2, the stress evolution along a fiber segment can be expressed by the Eq. (2.23). Moreover, it has been pointed out in [110] that the latter equation reduces to:

$$\sigma_f(\zeta) = E_f \varepsilon_{f\infty} [1 - e^{-\gamma\zeta}] \quad (8.1)$$

for sufficiently long fiber segments, i.e., for  $\gamma l \geq 10$ . Here  $\zeta$  is the distance from the fracture and the parameter  $\gamma$  expresses an indication about the stress-transfer efficiency of the interface [110]. In fact, for  $\zeta = \frac{1}{\gamma}$  the 63% of the infinite load is reached. In the present case, the evolution of the fiber deformation as a function of the  $z$  coordinate, and thus as function of the distance  $\zeta$  from the fiber failure, is available allowing for the determination of  $\gamma$  and  $\sigma_{f\infty} = E_f \varepsilon_{f\infty}$  by a fitting procedure. Their evolution as function of the ageing time are reported in Fig.8.3 and in Fig. 8.4 respectively.

Note that the long term curves corresponding to immersion time greater than 130 days are not reported in Fig. 8.2 for clarity.

The theoretical value of the coefficient  $\gamma$ , Eq. (2.24), depends on the elastic properties of the matrix and on the parameter  $R^*$  that defines the radial distance at which the matrix is sheared. These parameters are evidently linked in

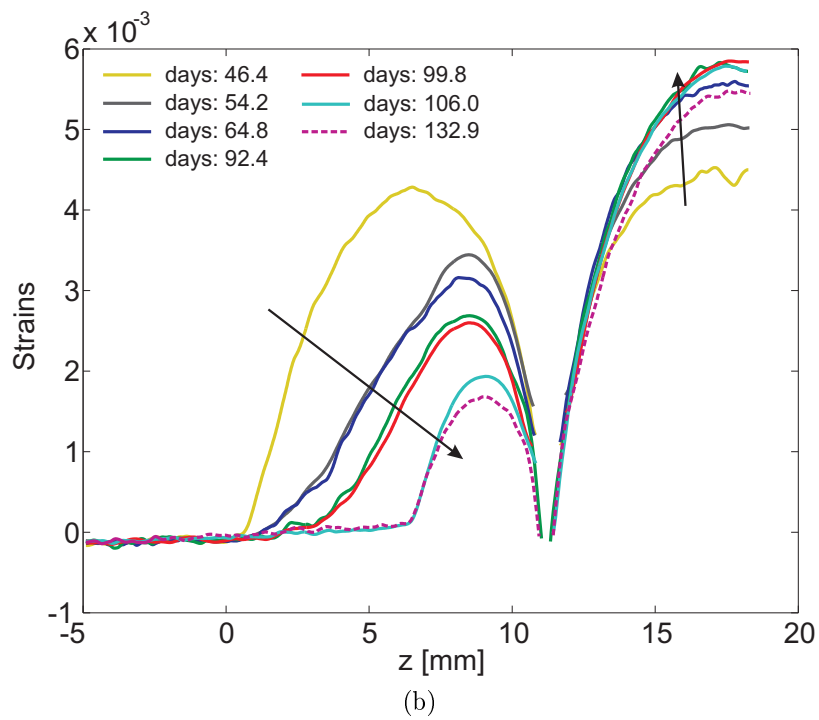
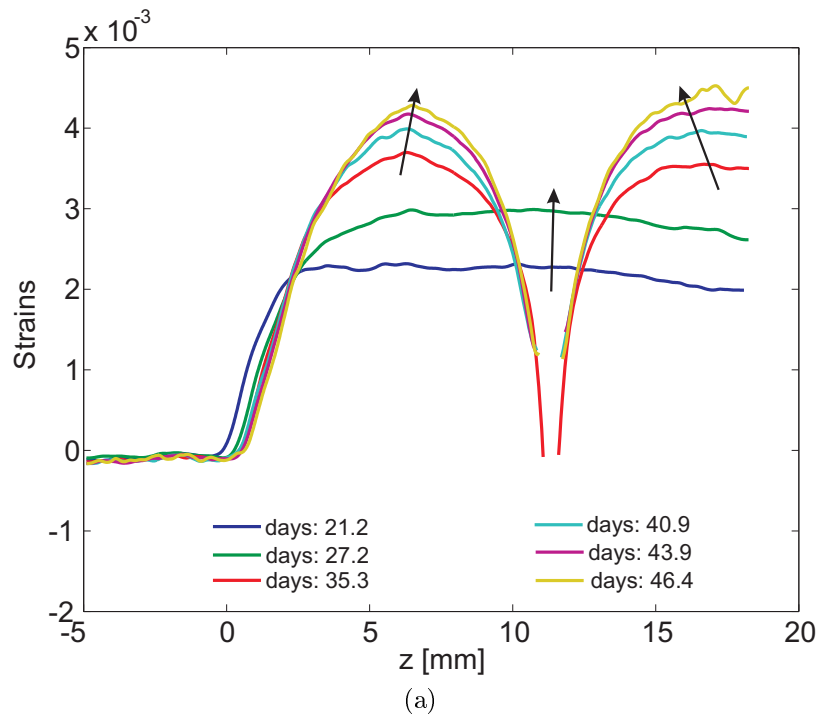


Figure 8.2: Fiber strains evolution: a) right before fracture and just after, b) long time exposure.



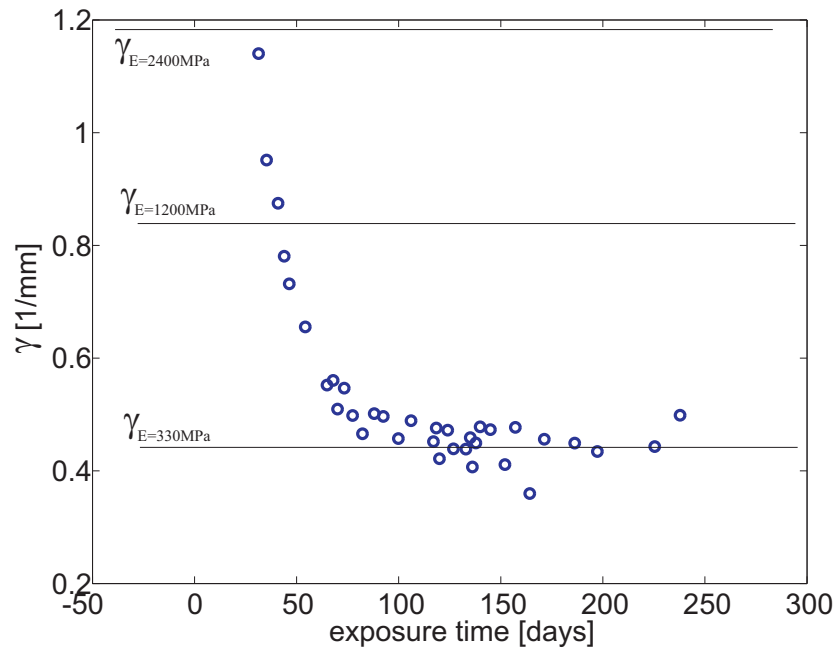


Figure 8.3: Evolution of the stress-efficiency as function of the ageing time.

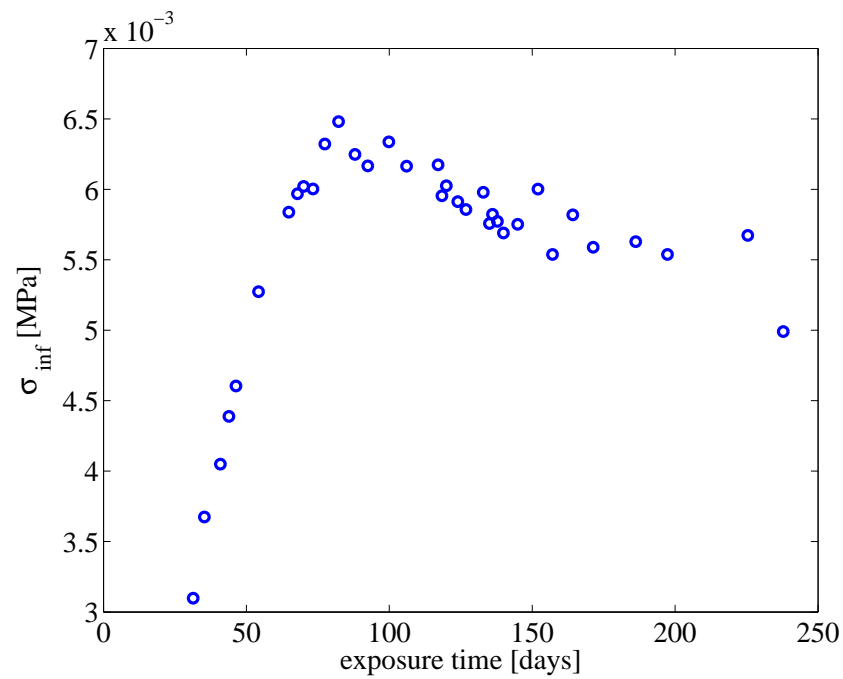


Figure 8.4: Shear lag stress plateau evolution as function of the exposure time.

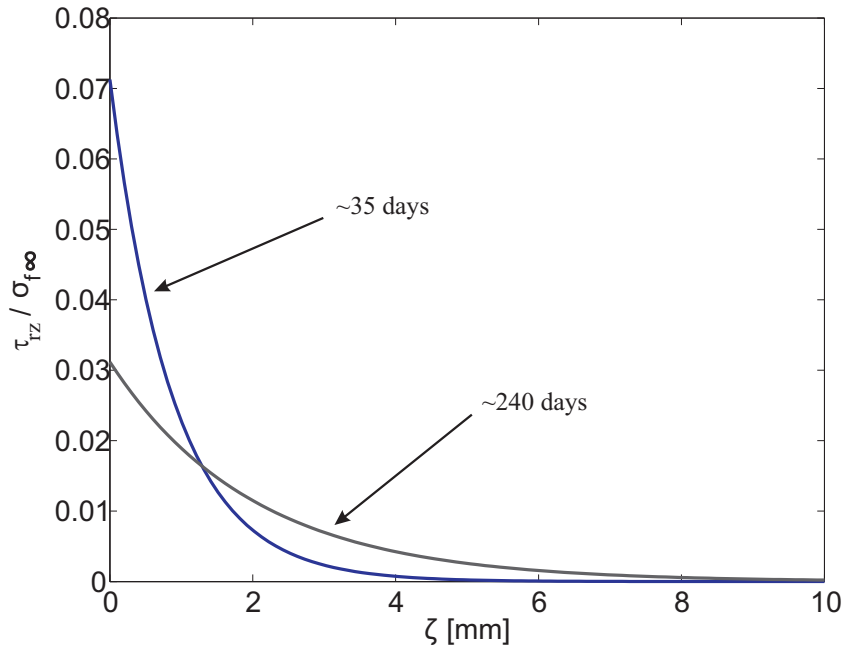


Figure 8.5: Shear stress distribution as function of the distance from the fiber failure at the early stage of diffusion and close to saturation.

the present case since the matrix material properties are changing with water concentration inducing a change also in the  $R^*$ .

As an example, three theoretical values of  $\gamma$  are determined using Eq. (2.24) in which  $R^* = 3r_f$  and the following material properties are used: the Young's modulus corresponding to the dry state at room temperature, dry state at  $50^\circ\text{C}$  and the average of the long term modulus plateau (Fig. 6.3). The results are shown in Fig. 8.3. It can be seen that the combination of the chosen  $R^*$  and  $E = 330$  MPa well approximate the long term experimental trend of  $\gamma$ .

The influence of the  $\gamma$  parameter on the shear distribution at the interface is reported in Fig. 8.5 where the reduction to one third of the shear stress peak from the low concentration state to the close to saturation state can be noticed.

### 8.1.2 Linear elastic fracture mechanics approach to interfacial cracks

The fiber/matrix debonding growth is by definition an interphase crack propagation. It was demonstrated by Williams [111] that a crack propagating at

the interface of two dissimilar materials is in a generalized mixed mode state.

In this case the complex stress intensity factor is defined :

$$\mathbf{K} = K_I + iK_{II} \quad (8.2)$$

whose physical meaning is related to the following interface traction expression [111–115]:

$$\sigma_{22} + i\sigma_{12} = \frac{(K_I + iK_{II})}{\sqrt{2\pi r}} r^{i\epsilon} \quad (8.3)$$

where  $\epsilon$ , called oscillatory index, is a function of the material properties that compose the interface:

$$\epsilon = \frac{1}{2\pi} \ln \left( \frac{1 - \beta}{1 + \beta} \right) \quad (8.4)$$

where  $\beta$  is a measure of the mismatch between the bulk modulus of the two components and assumes the following form [112]:

$$\beta = \frac{\mu_1(k_2 - 1) - \mu_2(k_1 - 1)}{\mu_1(k_2 + 1) + \mu_2(k_1 + 1)} \quad (8.5)$$

in which  $\mu_{i=1,2}$  are the shear moduli of the 2 components, and  $k_{i=1,2} = 3 - 4\nu_i$  or  $k_{i=1,2} = \frac{3-\nu_i}{1+\nu_i}$  for a plane stress or plane strain problem respectively.

Moreover, fixing an arbitrary distance from the crack tip, i.e. posing  $r = \hat{r} = \frac{r_f}{2}$ , an indication on the mode mixity of the actual configuration can be determined by calculating the angle  $\Psi$  as follows:

$$\Psi = \arctan\left(\frac{\sigma_{12}}{\sigma_{22}}\right) \quad (8.6)$$

In order to establish the evolution of the dominant opening mode, the stress intensity factors generated by the presence of interfacial cracks of different lengths are determined using Abaqus. In particular, in the residual-thermo-hygro-mechanical model presented in Section 7.3, the fiber failure and three interfacial cracks are introduced by doubling the nodes in the fiber at  $z \sim 11.4$  mm and at the fiber-matrix interface as indicated in Fig. 8.6.

The introduction of interfacial cracks at the beginning of the diffusion process is possible because at the fiber-matrix interface the concentration flux is

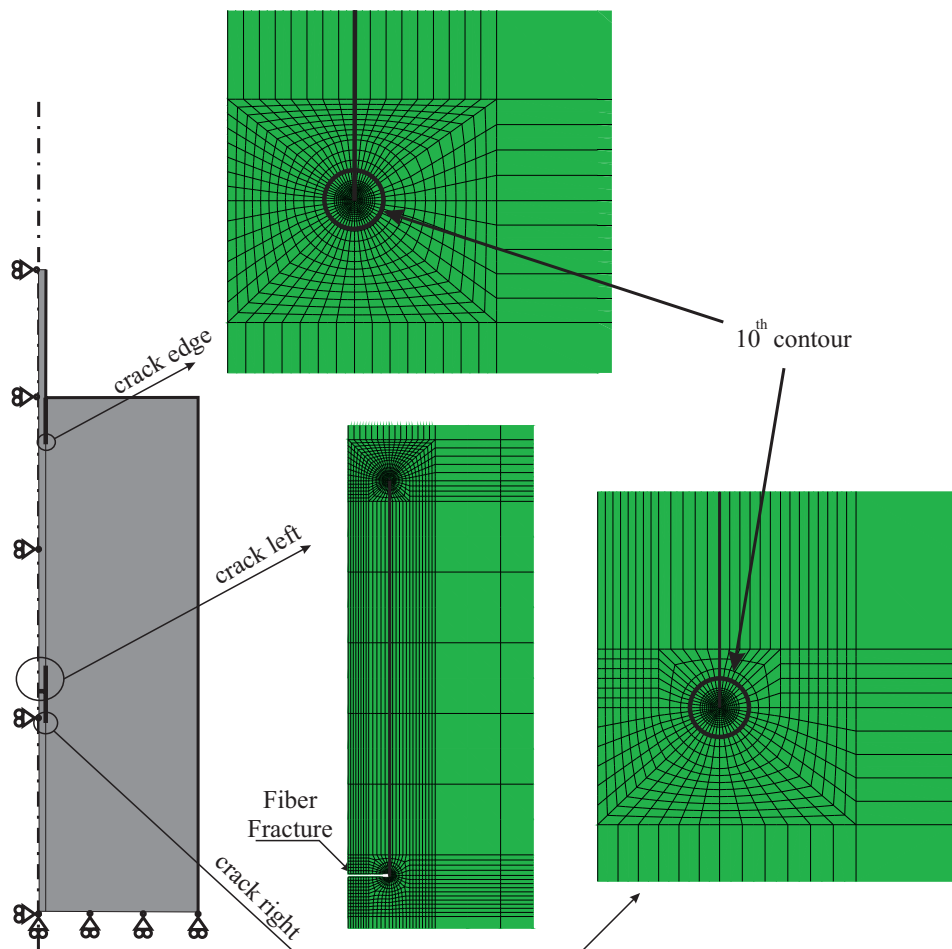


Figure 8.6: Fiber fracture and fiber-matrix debonding locations.

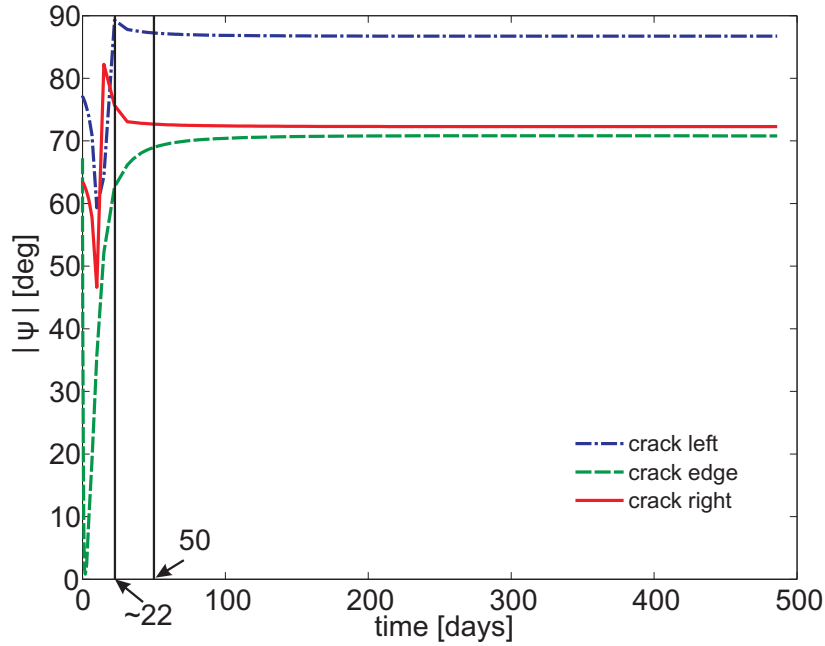


Figure 8.7: Evolution of the  $\Psi$  angle with the exposure time.

imposed equal to zero by the materials properties of the fiber, condition that is also respected by doubling the nodes and creating a new free surface. The results indicate that the three interfacial cracks are subjected to a predominant shear opening mode as showed in Fig. 8.7. In fact, it can be noticed that after 50 days of immersion all the cracks exhibit a  $\Psi \geq 70^\circ$  that become  $\sim 90^\circ$ , i.e pure shear mode, for the crack situated on the left hand side of the fiber failure. Since all fiber fractures appeared in a range of time comprised between  $\sim 30$  and  $\sim 60$  days a predominant shear state is assumed. Moreover, for earlier ageing times only, a crack already present at the edge would have experienced a practically pure opening mode for a reduced amount of time.

## 8.2 Fiber matrix debonding

Based on the discussion in the Section 8.1.2 it can be said that the propagation of an interfacial crack take place due to a substantial shear opening mode. For this reason, an uncoupled cohesive model is chosen and only a propagation in shear is allowed to take place. In the next paragraph, the notation used in the description of the cohesive law is reviewed. Furthermore, because the water has

a large influence on the properties of the interface, the parameters describing the cohesive law are made concentration dependent by the development of appropriate user defined subroutine that works interactively with the available code in Abaqus.

### 8.2.1 Cohesive-elements approach

The cohesive description chosen is a traction-separation law in both shear and tensile deformation. According to Camanho [116] and as implemented in Abaqus [106] a traction vector,  $\mathbf{t}$ , is defined having 2 components in the axisymmetric case,  $t_n$  and  $t_s$  that are the normal and shear traction respectively. The traction vector is linked to the corresponding nominal strains by the elastic matrix  $\mathbf{K}$  as follows:

$$\mathbf{t} = \begin{Bmatrix} t_n \\ t_s \end{Bmatrix} = \begin{bmatrix} K_{nn}(c^*) & 0 \\ 0 & K_{ss}(c^*) \end{bmatrix} \begin{Bmatrix} \varepsilon_n \\ \varepsilon_s \end{Bmatrix} = \mathbf{K}\boldsymbol{\varepsilon} \quad (8.7)$$

Where the  $K_{nn}$  and  $K_{ss}$  componets are the element's stiffness in traction and in shear that are functions of the concentration at the interface. Notice that in the formulation used, the off-diagonal elements are set to zero in order to force the cohesive elements' behavior to be uncoupled in normal and shear mode as determined on the basis of the LEFM approach. In addition, in order to ensure the same stress transfer between the matrix and the fiber, as if the cohesive elements were replaced by the matrix, the following relationships are used [106,116]:

$$\begin{cases} K_{nn}(c^*) = \frac{(1-\nu_m)E(T,c^*)}{(1+\nu_m)(1-2\nu_m)} \frac{1}{T_0} \\ K_{ss}(c^*) = G(T,c^*) \frac{1}{T_0} \end{cases} \quad (8.8)$$

where  $K_{nn}$  is determined on the basis of the plain strain modulus of the matrix and the  $K_{ss}$  on the basis of the shear modulus.

Moreover the following relationships are established between the thickness of the cohesive elements,  $T_0$ , and the separations  $\delta_n$  and  $\delta_s$  :

$$\varepsilon_n = \frac{\delta_n}{T_0} \quad \varepsilon_s = \frac{\delta_s}{T_0} \quad (8.9)$$

The chosen damage initiation criterion is the maximum nominal stress. The

condition is satisfied when one of the normalized nominal stress in Eq. (8.10) reaches unity:

$$\max \left\{ \frac{t_n}{t_n^0}, \frac{t_s}{t_s^0(c^*)} \right\} = 1 \quad (8.10)$$

Here,  $t_n^0$  and  $t_s^0$  are the imposed limit stresses in traction and in shear. Note that, because a substantial mode II drives the crack,  $t_n^0$  is set to infinity in such a way that non mode I fracture is triggered. In addition, the maximum shear stress,  $t_s^0(c^*)$ , depends on  $c^*$ .

The damage evolution is considered linear and the maximum shear deformation is determined on the basis of the energy criterion. The evolution of the dissipated energy  $G_c(c^*)$  is itself function of the concentration. The so-defined cohesive law is reported schematically in Fig. 8.8 where the used value at zero concentration are  $G_c(c^* = 0) = 0.23 \text{ mJ/mm}^2$  and  $t_s^0(c^* = 0) = 20 \text{ MPa}$  obtained from [117, 118] and at saturation the following reductions are found:  $G_c(c^* = 1) = 0.0025 \text{ mJ/mm}^2$  and  $t_s^0(c^* = 1) = 0.25$ . It can be noticed from Fig. 8.8 that a non linear evolution between the cohesive properties in the dry and at saturation is used in the modeling. In particular, a quadratic decay was found to be appropriate and it should be highlighted that, with the same extreme properties, a linear evolution is not sufficient to keep the fracture propagating at the interface.

The comparison between experimental data and the prediction is reported in Fig.8.9a & b. In particular, the redistribution of strains in the fiber at the early stage of the fracture propagation is reported in Fig.8.9a. It can be seen that on the right hand side of the fracture the strains level at  $z \simeq 20 \text{ mm}$  and the strain gradient between that zone and the fiber failure are predicted with high accuracy. Moreover, on the left side of the fracture, the strain gradient and the peak of fiber deformation are also showing very good agreement with the experimental results. Concerning the specimen entry point, the development of a damaged zone at  $0 \leq z \leq 1.5 \text{ led}$ , in first place, to replicate the initial debonding in that zone (cfr. with Fig. 8.2) and, secondly, to better describe the therein present strain gradient (cfr. with 7.12). The comparison reported in Fig.8.9b is quantitatively less accurate. However, the main experimental features are correctly reproduced. Firstly, the debonding continues almost

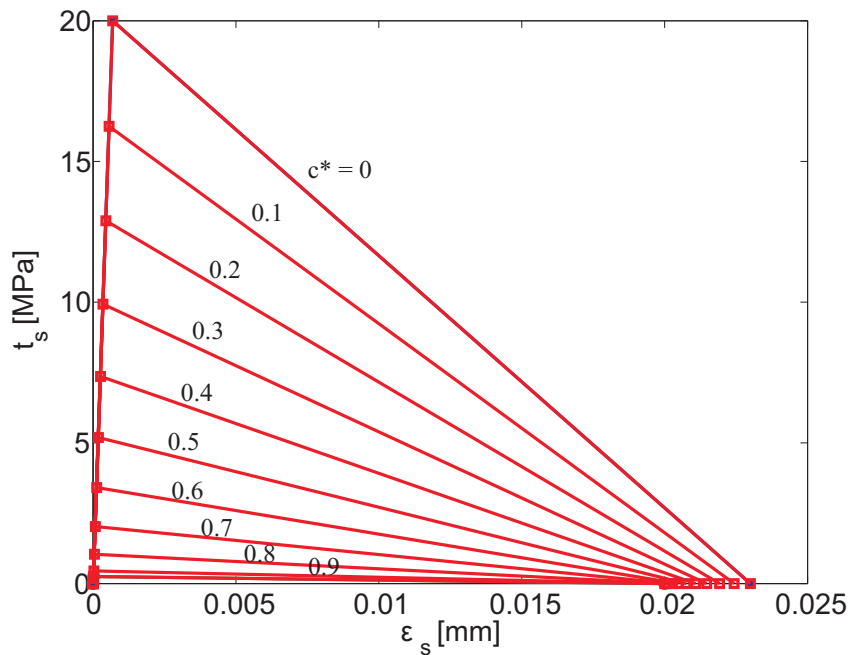


Figure 8.8: Cohesive law evolution with concentration at the interface: quadratic dependency.

uniquely from the specimen edge, letting the response of both sides of the fiber fracture unaltered. Secondly, for increasing exposure time the extensive debonded created has as secondary effect the reduction of the strain peak on the left fracture side whereas on the right side the deformation continuously increases. It appears that the deformation imposed to the fiber is the result of the balance between the increasing matrix swelling and the interface fracture propagation. In fact, these two concurrent phenomena act in opposite ways: increasing (and respectively decreasing) the fiber strains.

A first order verification of the quality of the debonding model herein presented can be drawn by comparing the position of the crack tip for the edge crack in both the experimental and numerical data. For this purpose, a virtual crack tip position is defined as the interception of a straight line tangent to the strain gradient at edge crack with the zero strain line in both experimental and simulated data. The results are reported in Fig.8.10 where a very good agreement can be noticed immediately after the fracture event. Afterwards, a similar trend of the numerical model and the experimental data is reported.

In order to evaluate the influence of plasticity on the debonding process



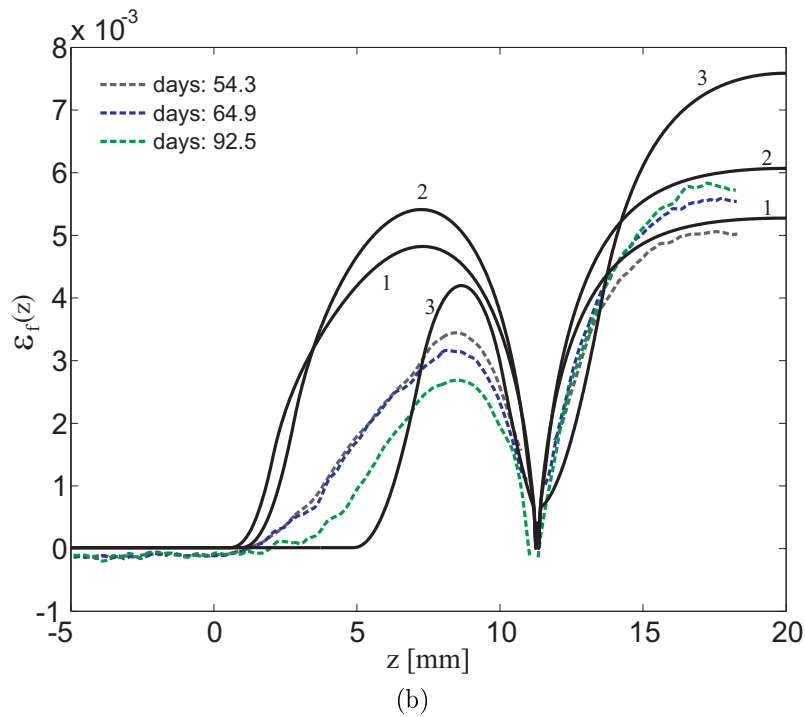
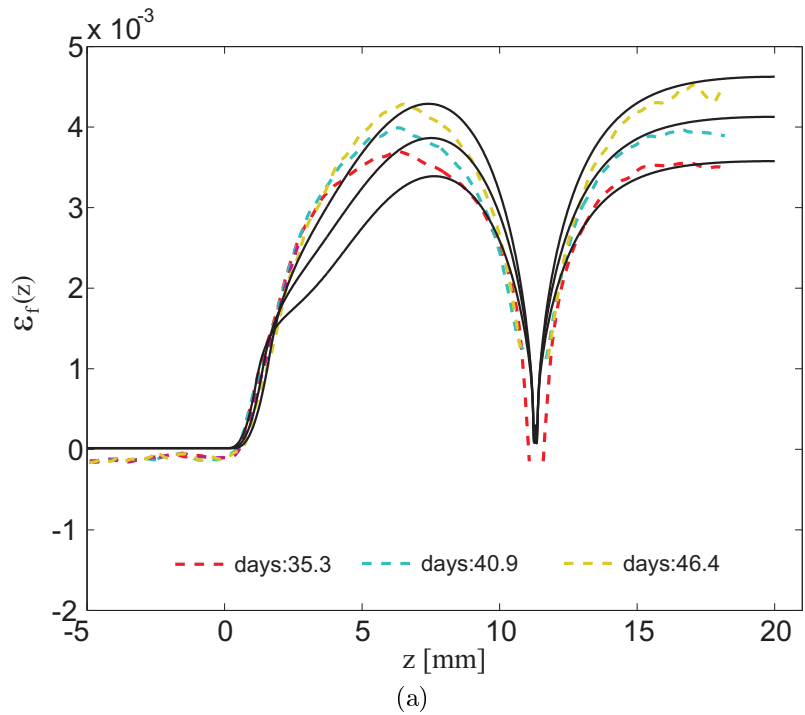


Figure 8.9: Fiber matrix debonding propagation: comparison between experimental data and predictions. (a) right after fracture, (b) long time exposure.

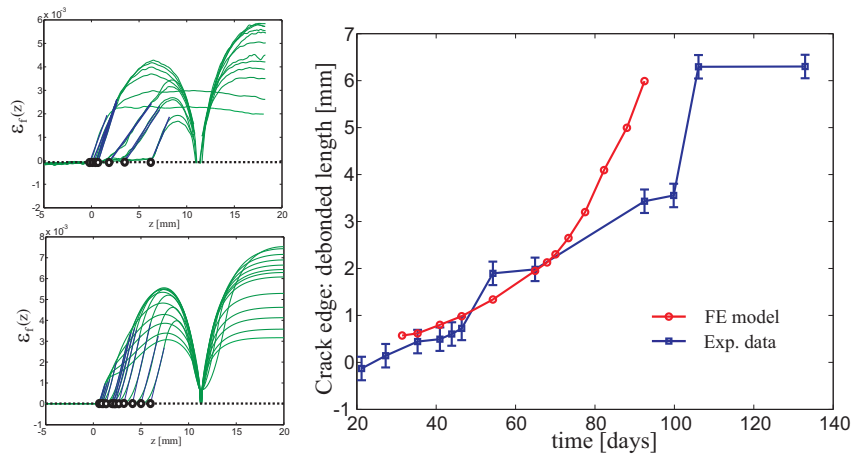


Figure 8.10: Debonding length evolution of the interface crack at the specimen edge. Comparison with FE prediction.

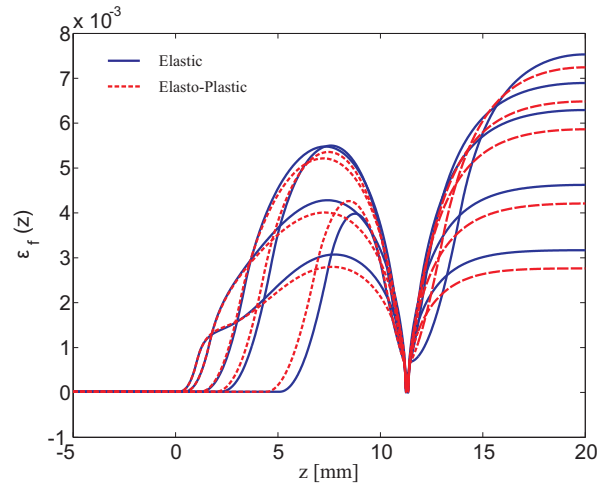


Figure 8.11: Influence of plasticity on the propagation rate.

the same model was run using the same material properties utilized to obtain the results in Fig.7.13. The results are reported in Fig.8.11 and compared with the prediction in the case of the matrix considered a linear elastic material. As could be expected, plasticity introduces a sort of shielding effect at the crack tip reducing the stress level therein created and thus reducing the crack propagation rate. Consequently, the maximum strain levels predicted appeared lowered.

## Chapter 9

# Hygrothermal ageing of unidirectional composites

In this section, the developed methodology for the analysis of the hygrothermal ageing of the single fiber composite is applied to the case of unidirectional composite. In particular, the composite's coefficient of moisture expansion along the fiber and in the transverse directions are calculated using short FBG gratings. In addition, the absorption curve of the composite is determined by means of control coupons. The data retrieved this way are used in an identification procedure in order to compute the diffusivity and saturation level based on a pure Fick's law of diffusion.

### 9.1 Specimens preparation<sup>1</sup>

Composites plate having external dimensions of 250mm×150mm and a thickness of 3.5mm were prepared using pre-impregnated carbon fibers sheets supplied by the SGL group international. Each plate is composed of 24 layers of pre-pregs that are successively laid on a aluminum frame that ensures the above reported nominal dimensions and serves also as guide for the optical fiber positioning. In fact, slits are machined in predefined locations of the frame in order to keep the optical fibers straight and aligned along the desired directions (Fig.9.2).

---

<sup>1</sup>The experimental work reported in this chapter was conducted by Miss Amaia Uriarte during a semester Master project conducted under the author's supervision.

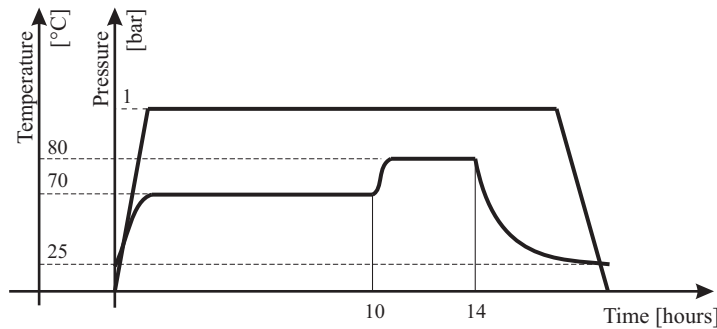


Figure 9.1: Composite plate processing cycle inside autoclave.

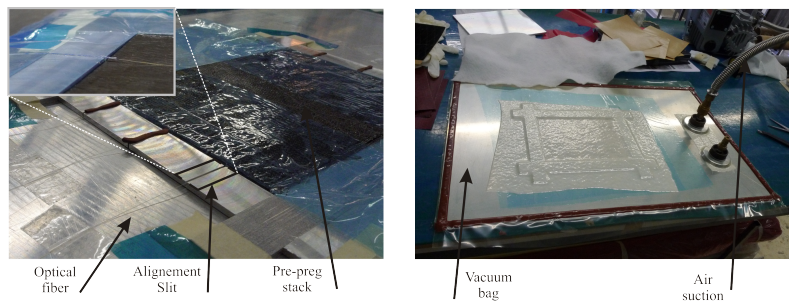


Figure 9.2: Composite preparation details.

The optical fibers are placed at the composite middle plane, i.e. between the 12<sup>th</sup> and 13<sup>th</sup> prepreg sheet in order for the FBG to capture the overall deformation of the laminate. The ensemble is then sealed into a vacuum bag and placed into the autoclave for the curing cycle reported in Fig.9.1. In order to study the hygrothermal behavior of the composite in the two principle directions, two sets of plate were produced. In the first one, the optical fibers are aligned along the reinforcement direction, while in the second set, the optical fibers are placed perpendicularly to the reinforcements. After the curing step, each plate is machined with a diamanted disk in order to obtain 3 rectangular samples with the following dimensions: 130mm×40mm ×3.5mm. Among the so produced 3 specimens, 2 of them have FBG sensors while in the third one a dummy fiber was embedded.

The latter specimen is used for the determination of the absorption curve while the first two are devoted to the hygric strain determination. Moreover, for the measurement of the longitudinal deformation, that is expected to be small since this deformation direction is dominated by the fibers properties, a multiplexed type of sensor with 8 FBGs, each one having a length of  $\sim 1.5$ mm

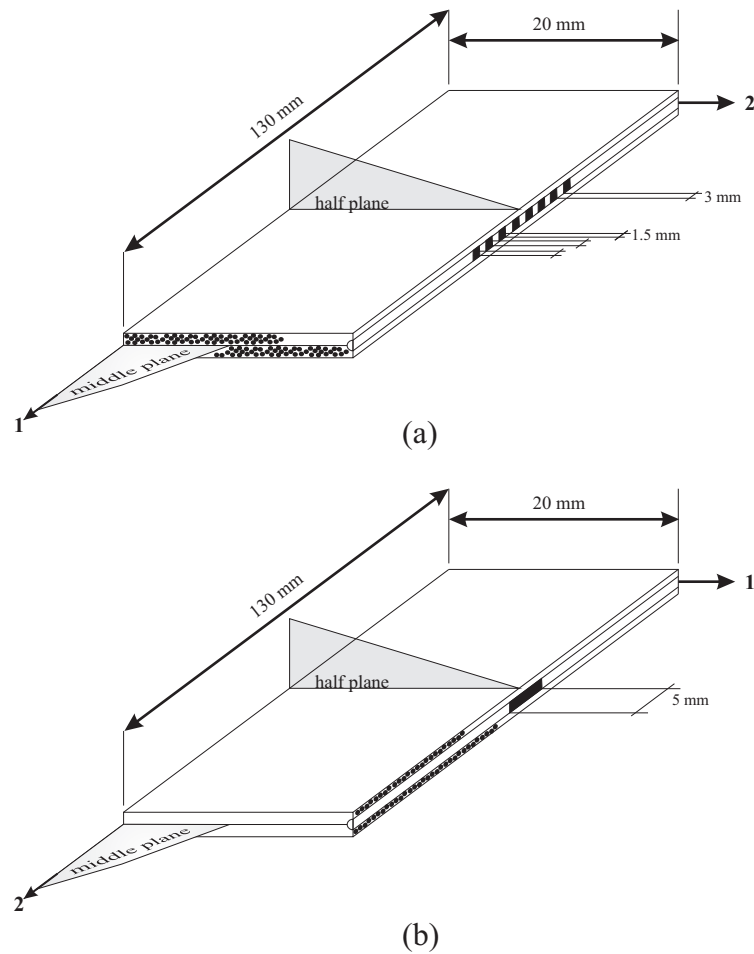


Figure 9.3: Composite specimen geometries for longitudinal strain deformation (a), and transverse strain deformation (b).

and spaced of about  $\sim 3\text{mm}$ , is used in order to average the deformation over a larger specimen zone. Conversely, the measurement of the transverse deformation is obtained by the use of single FBG having a length of 5mm. Details of the final specimen configuration are displayed in Fig. 9.3.

## 9.2 Residual deformation and thermal response

The longitudinal and transverse deformations imposed to the fiber by the processing were measured at room temperature after the specimen machining using Eq.(2.2). Concerning the longitudinal residual deformation an average value of  $450\mu\epsilon$  is found whereas the average transverse deformation was in the

Table 9.1: Composite longitudinal and transverse coefficient of thermal expansion.

	$\alpha_1$	$\alpha_2$
$^{\circ}\text{C}^{-1}$	$-2.65 \times 10^{-6}$	$28.7 \times 10^{-6}$

Table 9.2: Identified diffusion parameters.

	$D \left[ \frac{\text{mm}^2}{\text{s}} \right]$	$s[\text{vol.}]$
longitudinal	$9 \times 10^{-7}$	0.0252
transverse	$8.55 \times 10^{-7}$	0.0264

order of  $1200\mu\epsilon$ . It must be reported that a certain variation from specimens to specimens was noticeable and can be partially due to differences in void content and fiber volume fraction as highlighted by successive micrographies.

Moreover, the specimens were put into a oven at  $50^{\circ}\text{C}$  for 4h in order for the steady state thermal response to be established. Following a procedure similar to the one reported in Section 4.2 the longitudinal and transverse coefficients of thermal expansion,  $\alpha_1$  and  $\alpha_2$ , were determined from the change in wavelength of the sensors between room temperature and  $50^{\circ}\text{C}$ . The results are reported in Table 9.1 showing quantitatively good agreement with values reported in literature for carbon fiber composites [105]. The negative value of the longitudinal CTE is due to the thermal response of carbon fibers.

### 9.3 Diffusion identification

The ageing environment chosen also in the case of composite specimens is represented by a bath of demineralized water at  $50^{\circ}\text{C}$ . Specimens with dummy fibers were immersed and their weight monitored using the procedure reported in Section 5.3. The absorption curves for the two specimen configurations are reported in Fig.9.4 and successively used in an identification loop in order to determine the saturation and the diffusivity coefficient that are reported in Table 9.2.

The predictions for the two absorption curves are also reported in Fig.9.4, showing a maximum relative error (Eq. 2.29) of 14%.

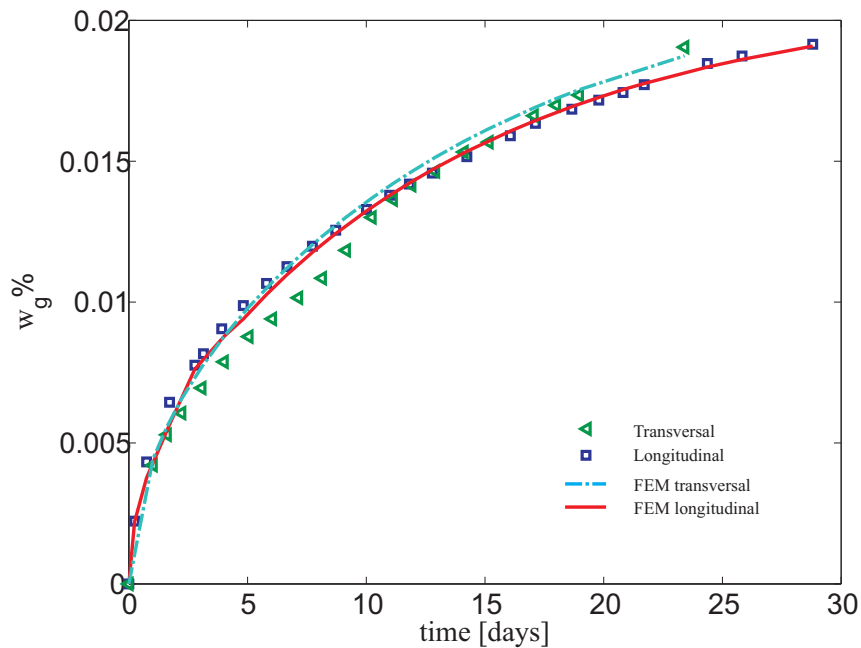


Figure 9.4: Composite absorption curves: experimental data and identification predictions.

## 9.4 Evaluation of the coefficients of moisture expansion

After the determination of the CTEs of the composite, both specimen types with the embedded optical sensors were immersed into the ageing bath. Because of the small thickness of the plates, the thermal equilibrium is rapidly established and the deformation recorded in dry condition at 50°C is firstly re-imposed. The FBGs wavelengths detected at this stage are chosen as new reference and the following changes are then due to the composite hygric expansion only. The longitudinal and transverse deformation as function of the total water uptake are reported in Fig. 9.5.

It can be noticed that the longitudinal deformation is practically absent whereas in the transverse deformation 2 linear trends can be distinguished. This behavior has been reported in the past by Hahn in [104]. The reduced expansion in the first part of the absorption curve was attributed the water filling the composite macrovoids. On the light of what is reported on the previous chapters, it appears reasonable to make the hypothesis that the presence of two

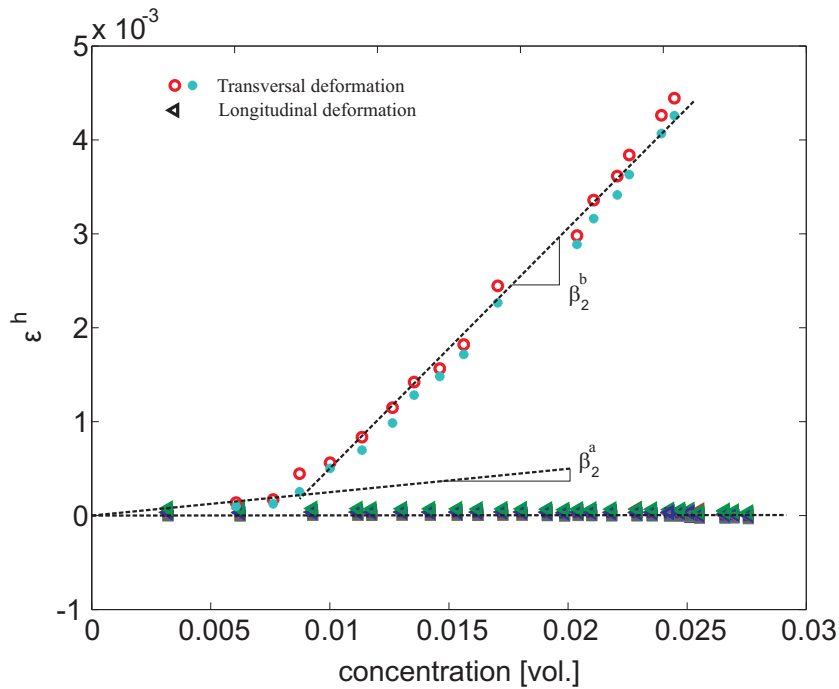


Figure 9.5: Composite hygroscopic expansion: longitudinal and transverse deformation.

Table 9.3: Composite coefficients of moisture absorption.

Coefficients of moisture absorption	
$\beta_1$	0.0003
$\beta_2^a$	0.0205
$\beta_2^b$	0.2430

expansion rates is more related to the intrinsic resin response to water absorption rather than the presence of cavities and voids into the composite. Further work is necessary to establish the correctness of this hypothesis since the resin used in the prepregs is different from the one used in the micromechanics analysis, although the general class of epoxies is conserved. The CMEs in the two principal directions are reported in Table 9.3 showing very good agreement to what reported by Daniel [105] for similar materials ( $\beta_1 = 0.01$  and  $\beta_2 = 0.2$ ).



# Chapter 10

## Conclusions and future work

### 10.1 Synthesis and Conclusion

The hygrothermal ageing of epoxies and epoxy-based composites was successfully addressed under multiples points of view. The work analyzes the physics involved into the problem and determines the progressive decrease of the load bearing capacity of a SFC as function of the exposure time. The ageing environment considered was a water bath constantly kept at 50°C in which neat resin coupons, single-fiber composites specimens and carbon-fiber composites were immersed for time periods ranging from few months to couples of years.

The mechanical properties evolution of the bare resin, as function of the water content, were investigated using conventional tensile and relaxation tests performed into a special designed tensile-setup able to reproduce the imposed ageing conditions. These methodologies established the average mechanical response of the epoxy to the considered hot-wet environment shading light to the progressive decrease of both short and long term moduli. In addition, the elastic properties of the resin were investigated using a developed macro-indentation procedure at room temperature allowing to establish the influence of the sole water on the resin. The latter approach allowed to determine that a smooth gradient of properties is present across the specimen thickness.

The diffusion type and relative parameters were determined experimentally measuring the absorption curve of the epoxies and using a mixed experimental-numerical identification scheme. In particular, it was found that a concentration dependent diffusivity better described the epoxy absorption behavior with

respect to a classical Fickian type of diffusion.

Moreover, the analysis was then conducted using a SFC whose reinforcement is represented by an optical fiber having a long FBG sensor inscribed on it. This elementary unit cell was helpful in determining in first place the residual deformation field produced during the fabrication process; in particular, a new shrinkage function was identified on the basis of radial cuts machined into the SFC at different  $z$  locations. Secondly, the SFC cell was used in the determination of the epoxy CTE. The established method was then successfully applied to a particle-reinforced epoxy allowing to determine the influence of the different fillers to the CTE of the composite. Thirdly, the hygric expansion of the SFC cell was also monitored using the OLCR apparatus. The fusion of the latter data with the absorption curve allowed for the determination of the CME of the resin. It was found that the expansion rate is not linear with the water content. With the data retrieved a residual-thermo-hygroscopic model was successfully built in order to simulate the complex response of the SFC to ageing environment.

Furthermore, the synergistic effect of the decreasing of the epoxy's material properties and the progressive expansion of the resin introduces firstly the failure of the fiber and then a progressive interface damage and fiber debonding. The fiber fracture is studied with the help of the shear lag model, whereas the debonding process was initially analyzed using the LEFM approach. The latter one allowed to establish the opening mode mixity for interfacial cracks at different locations. It was found that a substantial mode 2 opening is developed and this knowledge is used afterwards to simplify the debonding phenomenon. In fact, the debonding process is studied integrating cohesive elements, at the fiber-matrix interface, into the residual-thermo-hygroscopic model and establishing the dependency of the cohesive properties on the water concentration.

Finally, the developed characterization methodologies were applied to the case of a carbon-fiber/epoxy composite in order to prove the possibility to extend the work done on the unit cell to a real composite.

On the light of the study briefly summarized above, it can be concluded that the hygrothermal ageing of epoxy based composites is strongly affected by the matrix response to hot-wet environments. In particular, the coefficient

of moisture expansion of the resin, playing a fundamental role on the evolution of the internal stress-strain field, is accurately determined. This parameter is found to be an increasing function of the water concentration and its influence on the global hygric expansion of the laminate can be suspected on the basis of the recorded experimental data.

The fiber fracture event highlighted the importance of the residual deformation field stored in the composite. In fact, it is essential for a correct analysis of the stress redistribution around a fiber failure and, in addition, the simulation of the debonding process would not have been possible without knowledge of the initial stress state.

Finally, the properties and strength of the interface can be considered a decreasing function of the water concentration. The latter consideration has great relevance on materials like composites, where the load among the components is distributed by the interfaces.

## 10.2 Connected problems not directly examined

During this work, two tacit assumptions were made in order to simplify the already complicated coupling among the Physics involved. The first one concerns the possibility that the diffusion process depends on the stress state of the materials. This possibility is reported in literature by Fahmy and Hurt in 1980 [75], they found that the diffusivity coefficient in the diffusion law is an exponential function of the volumetric stress. This dependency has two principals repercussions on the analysis conducted: in first place, the concentration dependency highlighted during the diffusion identification procedure can be in part due to this cross-coupling effect. Secondly, when the fiber failure occurs the stress intensification produced close to the tip of the crack can be the source for a preferential diffusion path explaining partially why the interface weakening is not a simple function of the water concentration. However, it must be underlined that the SFC cell was not externally loaded and, for this reason, the average level of stress was relatively low justifying the assumption made.

The second hypothesis concerns the coefficient of thermal expansion of the resin. It was assumed that once the thermal equilibrium is reached no further

thermal expansion is added to the system. The latter statement is correct only if the thermal expansion of the matrix is not function of the concentration, in the opposite case, the derivative of the thermal expansion with respect to the concentration must be taken and multiplied by the  $\Delta c$  step considered. This effect was judged to have a second order influence and thus non considered in the analysis although evidence of the phenomenon are reported in literature by Drotning and Roth in [119] for the PMMA material. They reported a reversible increase in the expansion that in the present case should be depurated from the hygric response.

### 10.3 Perspectives

Ending this work, as probably it happens when closing the development of a methodology, many areas remain to be further explored. In first place, the assessment of the coefficient of moisture expansion in the high-concentration region, although its behavior was bound between a linear and a quadratic extrapolation, it is still to be completed because of the failure of the optical fiber. It is opinion of the author that, regarding this subject, a multifiber cell can be developed in order to verify the already available expansion law and then to infer the remaining part of the curve.

The evolution of the interface properties should be investigate using independent measurements and the possibility of water permeation at the interface, as the fiber debonds from the matrix, verified. On this matter, the use of the single fiber fragmentation test is undoubtedly a valid option because allows to test the interface properties at different aged conditions. Moreover, the test can be conducted using long FBG sensors recording the evolution of deformation following multiple fiber fractures.

The coupling of the latter two propositions represents the natural evolution of the work. In fact, the tools developed are ready to be applied to more complex composite unit cells opening, *de facto*, the way towards a homogenized analysis of the hygrothermal response of composites and of their damage accumulation during ageing. In addition, the study of stress redistribution after a fiber failure on neighbouring fibers it surely of great interest from a micromechanical and multiscale point of view.

Finally, the questions of size effects regarding the dimensions of the optical fiber with respect to the diameters of the standard reinforcements in composites should be addressed. It must be reported that some effort were devoted in this direction during this work and a brief summary is reported in the next section.

## 10.4 Reduction of the sensor's intrusiveness: small diameter fiber Bragg gratings<sup>1</sup>

In this section, optical low coherence reflectometry and fiber Bragg gratings written in small diameter (50 micrometer) optical fiber were used for measurements of non-homogeneous internal strain fields inside an epoxy specimen. The results were compared with measurements using fiber Bragg gratings in standard size (125 micrometer) single mode fiber and showed that smaller fibers are less intrusive at stress heterogeneities.

### 10.4.1 Fiber Bragg grating sensors

For the measurements of the distributed strain along the fiber inside the epoxy specimen, three fiber Bragg gratings were embedded. Each FBG was inserted in a different specimen. First, a commercial FBG written in standard SMF-28 single-mode fiber with core/cladding dimensions of 9/125 $\mu\text{m}$  was used. The grating length was 20mm with a peak reflectivity of 50%. Second, FBGs written in small-diameter fiber (SILITEC SA) with core/cladding dimension of 11.6/50  $\mu\text{m}$  were used. The fibers were hydrogen loaded before inscription using ArF excimer laser, and thermally annealed after fabrication. The gratings were 13 mm long with typical peak reflectivity of 50 %. The Bragg wavelength of all gratings was around 1550 nm.

Before embedding the FBGs into the epoxy, the measurement of the stress sensitivity for standard and small-diameter fiber was performed. Calibrated axial loads were applied (using precisely measured weights) and the corre-

---

<sup>1</sup>This part of the chapter reports the preliminary work on distributed strain measurement in small diameter optical fibers and FBG sensors conducted in collaboration with the Advanced Photonics Laboratory at EPFL and published in [120].

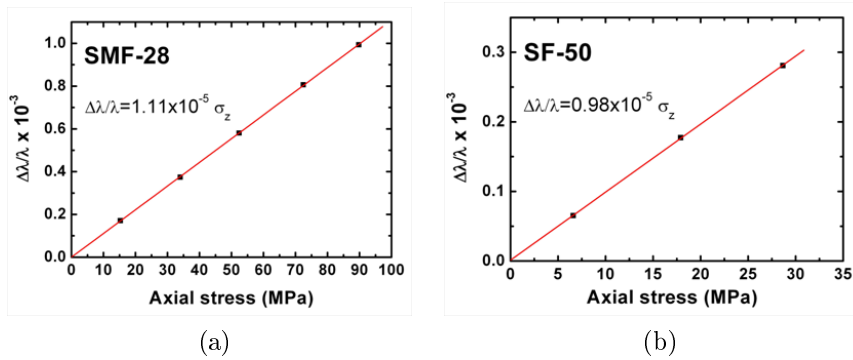


Figure 10.1: Wavelength shift as a function of the applied axial stress for (a) standard single-mode fiber (SMF-28 125  $\mu\text{m}$ ) and (b) for a small-diameter fiber (SF-50, 50  $\mu\text{m}$ ).

sponding changes in the Bragg wavelength were obtained for both fibers as shown in Fig. 10.1 in terms of stresses. The results for the standard fiber correspond well to the results reported in the literature [121]. The small fiber showed lower sensitivity to the axial stress, which might be attributed to the fiber material composition (Young's modulus). Assuming similar  $p_e = 0.22$ , and fiber diameters of  $125 \pm 0.3 \mu\text{m}$  and  $49.6 \pm 0.3 \mu\text{m}$  the corresponding Young's moduli are  $\sim 70 \text{ GPa}$  and  $\sim 81 \text{ GPa}$ , respectively.

#### 10.4.2 Sample preparation

Both FBG types were embedded in rectangular epoxy samples (Fig. 10.2a). Rectangular blocks of dimensions  $10 \times 10 \times 40 \text{ mm}$  have been fabricated using the mixture of two resins DER330<sup>©</sup> DER732<sup>©</sup> and the hardener DEH26<sup>©</sup> following the procedure reported in Section 3.1.

The mixture is then casted in a specially designed horizontal mould with the fiber in place (Fig. 10.2b). To prevent fiber fracture at the exit points of the mould and avoid resin leakage, thin rubber bands (RB) were placed horizontally on the right and left upper and lower parts of the mould. The fiber was manually positioned in the mould with the FBG near the edge of the mould to achieve non uniform strains with a small pretension held with tapes on planes (PL) extended from both sides of the mould. Once the fiber was fixed in the correct position the mould was closed with a cap (CP) with two

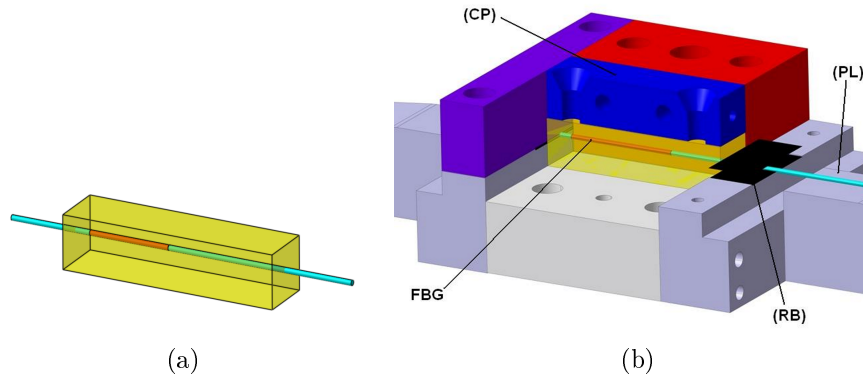


Figure 10.2: Rectangular epoxy sample (10x10x40 mm) with embedded FBG (a) and mould for specimen preparation (b): RB: rubber stripes; PL: plane to support the fiber; CP: cap with openings.

openings in one of which the resin is casted and the other one guaranteed air evacuation. This mould configuration allowed achieving good fiber placement and excellent external surface finish.

### 10.4.3 Measurement of embedded gratings

After embedding the FBGs into the epoxy specimen, reflectivity and OLCR spectra (amplitude and phase) were measured and compared with the spectra before embedding. Fig. 10.3 and Fig 10.4 show the reflectivity with the maximum normalized to 0 dB (Fig. 10.3a) and OLCR phase measurement (Fig. 10.3b) for the SMF-28 fiber and as an example for the small diameter fiber 2 (Fig. 10.4). All gratings indicated a noticeable shift to lower wavelength due to a compressive strain induced by the epoxy shrinkage. In addition, there is spectral broadening and chirping as a typical signature of non-homogeneous strains.

The FBGs written in the small-diameter fiber showed a smaller shift compared to FBG in SMF-28, which can be explained by the lower stress sensitivity (Fig. 10.1). From the spectral measurements, it is possible to obtain information on the average strain (proportional to peak shift) along the grating, but it is not possible to assess the strain distribution itself. However, using the OLCR measurement, the strain distribution can be retrieved from the local Bragg wavelength distribution. The distributed strain can be

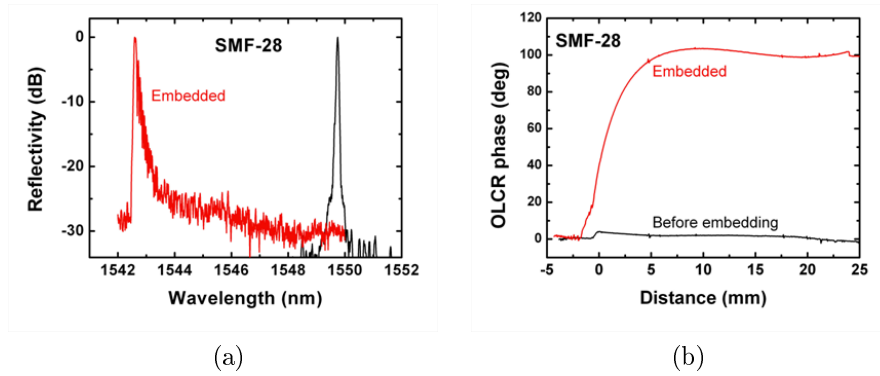


Figure 10.3: Reflection spectra (a) and OLCR phase measurement (b) for FBGs written in SFM-28 before (black) and after embedding (red). The reflectivity was normalized to 0 dB.

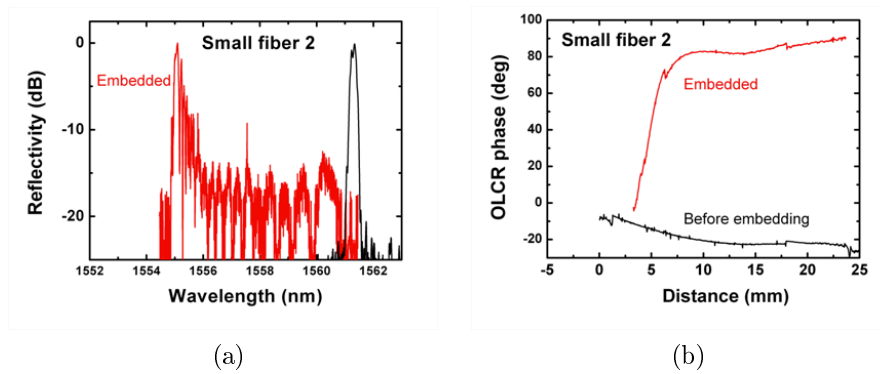


Figure 10.4: Reflection spectra (a) and OLCR phase measurement (b) for FBGs written in small diameter fibers from SILITEC SA (SF-50) before (black) and after embedding (red). The reflectivity was normalized to 0 dB.

obtained from Eq.2.11 and using the wavelength-strain conversion factor of  $\Delta\lambda_B/\varepsilon_z = \lambda_{B0}(1 - p_e) = 1.21 \mu\text{m}/\text{pm}$  for all fibers.

Fig. 10.5a shows strain distributions along the FBGs as a function of the position inside the sample; The strain distributions show a steep gradient near the sample edge and a plateau in the middle where the strains are uniform. The strain data from the small fiber 2 extend almost to the specimen entrance because the FBG was closer to the surface. The residual strain of  $5500\mu\varepsilon$  is similar (10% difference) for big and small fibers and approximately the same to the level reported under similar conditions [101]. A clear difference is observed between the SMF-28 and the small diameter fiber 2 at the specimen



entrance where the stress changes are maximal; this difference is attributed to the fact that, from the stress analysis standpoint, the smaller diameter fiber is less intrusive and disturbs to a lesser extent the strain field near the edge of the specimen. Residual strains in epoxies are commonly modeled as equivalent thermoelastic strains induced by an equivalent temperature change in the specimen. Thus, to better understand the experimental results and assess the influence of the fiber diameter, finite element simulations were performed. Two cylinders of 12 mm in diameter, each one with an axially located fiber of diameters 125  $\mu\text{m}$  and 50  $\mu\text{m}$  were considered with material properties equal to those of the material used in the experiments. Since the dimensions of the specimen's cross section were large compared to the fiber diameter, the cylindrical geometry considered in the simulations of the specimen with the small diameter does not influence the strain evolution along the axis. For simplicity and to qualitatively determine the influence of the fiber diameter on the residual strains, a uniform equivalent temperature change of 52  $^{\circ}\text{C}$  was considered. This temperature was calculated on the basis of a thermal expansion coefficient for the matrix  $\alpha_m = 11 \times 10^{-5} \text{ }^{\circ}\text{C}^{-1}$  [122], and that the strain matches the maximum experimentally observed value of 5750  $\mu\epsilon$  (Fig. 10.5a). Note that since the thermal expansion of the fiber is very small, as compared to that of the surrounding epoxy, it was considered negligible. Regarding the elastic properties the following values were considered: for the epoxy a Young modulus of  $E_m = 2.35 \text{ GPa}$ , measured experimentally, and a Poisson's ratio, assumed equal to,  $\nu_m = 0.38$  were used. The corresponding values used for the fibers were: small fiber  $E_f = 81 \text{ GPa}$ , SMF-28  $E_f = 72 \text{ GPa}$ , and a Poisson's ratio of  $\nu_f = 0.16$  for both fibers. The results of the simulations shown in Fig. 10.5b indicate that the calculated distributions correspond qualitatively well to the experimental results. The strain in the middle of the specimen is independent of the fiber dimension; while at the entrance of the specimen, a steeper strain gradient along the small diameter fiber is calculated. The measured gradients are smaller than the simulated ones for both fibers; this is mainly attributed to the uniform equivalent temperature change applied along the specimen in the simulations.

The comparison of small-diameter and standard size fiber showed that the influence of the sample entrance is different for the two fiber types, but the

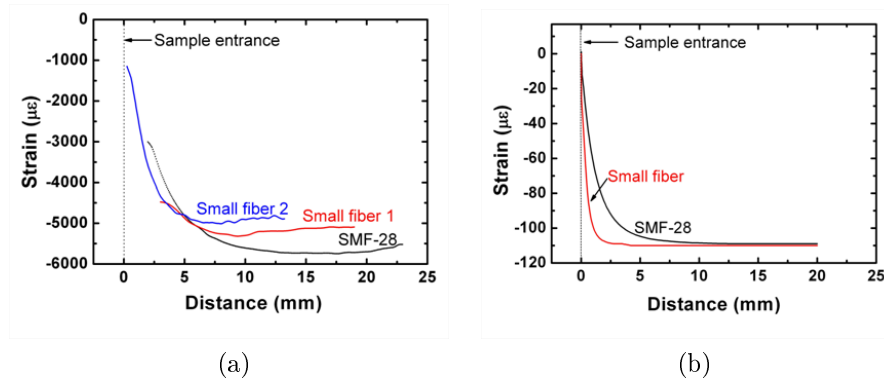


Figure 10.5: Distribution of the non-homogeneous internal strain along the FBG length inside epoxy specimen measured (a) and numerical simulation with  $1^\circ\text{C}$  decrease on the matrix, (b) for SMF-28 and small diameter fibers.

level of the strain in the middle of the sample was almost identical. Small diameter fibers are promising candidates to replace standard size fibers for sensing application in the near future as they are less intrusive at stress heterogeneities.

# Bibliography

- [1] L. G. Zhao, N. A. Warrior, and A. C. Long. A micromechanical study of residual stress and its effect on transverse failure in polymer-matrix composites. *International Journal of Solids and Structures*, 43(18-19):5449–5467, September 2006.
- [2] A.S. Maxwell, W.R. Broughton, G. Dean, and G.D. Sims. *Review of accelerated ageing methods and lifetime prediction techniques for polymeric materials*. NPL report DEPC MPR 016, 2005.
- [3] J. Comyn. *Polymer permeability*. Elsevier applied science publishers, Springer, 1985.
- [4] M. C. Lee and N. A. Peppas. Models of moisture transport and moisture-induced stresses in epoxy composites. *Journal of Composite Materials*, 27(12):1146–1171, 1993.
- [5] S. Roy. Modeling of anomalous moisture diffusion in polymer composites: A finite element approach. *Journal of Composite Materials*, 33(14):1318–1343, 1999.
- [6] P. Bonniau and A. R. Bunsell. A comparative study of water absorption theories applied to glass epoxy composites. *Journal of Composite Materials*, 15(3):272–293, 1981.
- [7] K. K. Aniskevich, A. Kh Kurzemnieks, and Yu O. Yanson. Effect of the prolonged action of temperature and moisture on the elastic properties and structure of an organic fiber-reinforced plastic. *Mechanics of Composite Materials*, 21(4):421–424, 1986.

- 
- [8] P. Nogueira, C. Ramirez, A. Torres, M. J. Abad, J. Cano, J. Lopez, I. Lopez-Bueno, and L. Barral. Effect of water sorption on the structure and mechanical properties of an epoxy resin system. *Journal of Applied Polymer Science*, 80(1):71–80, 2001.
- [9] W.J. Mikols, J.C. Seferis, A. Apicella, and L. Nicolais. Evaluation of structural changes in epoxy systems by moisture sorption-desorption and dynamic mechanical studies. *Polymer Composites*, 3(3):118–124, 1982.
- [10] C.E. Browning, G.E. Husman, and J.M. Whitney. Moisture effects in epoxy matrix composites. In *Composite Materials: Testing and design 4th Conference, ASTM STP 617*, pages 481–496. American Society for testing materials, 1977.
- [11] L. E. Asp. The effects of moisture and temperature on the interlaminar delamination toughness of a carbon/epoxy composite. *Composites Science and Technology*, 58(6):967–977, 1998.
- [12] C. L. Schutte, W. McDonough, M. Shioya, M. McAuliffe, and M. Greenwood. The use of a single-fibre fragmentation test to study environmental durability of interfaces/interphases between dgeba/mpda epoxy and glass fibre: the effect of moisture. *Composites*, 25(7):617–624, 1994.
- [13] C. L. Schutte. Environmental durability of glass-fiber composites. *Materials Science and Engineering: R: Reports*, 13(7):265–323, November 1994.
- [14] M. Ciccotti. Stress-corrosion mechanisms in silicate glasses. *Journal of Physics D-Applied Physics*, 42(21), 2009.
- [15] M. Muraoka, K. Ebata, and H. Abe. Effect of humidity on small-crack growth in silica optical fibers. *Journal of the American Ceramic Society*, 76(6):1545–1550, 1993.
- [16] N. Gougeon, M. Poulain, and R. El Abdi. Evolution of strength silica optical fibers under various moisture conditions. *Optical Materials*, 27(1):75–79, 2004.

- 
- [17] W. B. Hillig. Model of effect of environmental attack on flaw growth kinetics of glass. *International Journal of Fracture*, 143(3):219–230, 2007.
- [18] E. McKague Lee Jr, J. D. Reynolds, and J. E. Halkias. Swelling and glass transition relations for epoxy matrix material in humid environments. *Journal of Applied Polymer Science*, 22(6):1643–1654, 1978.
- [19] M. J. Adamson. Thermal expansion and swelling of cured epoxy resin used in graphite/epoxy composite materials. *Journal of Materials Science*, 15(7):1736–1745, 1980.
- [20] G. Z. Xiao and M. E. R. Shanahan. Swelling of dgeba/dda epoxy resin during hygrothermal ageing. *Polymer*, 39(14):3253–3260, 1998.
- [21] E. H. Wong, R. Rajoo, S. W. Koh, and T. B. Lim. The mechanics and impact of hygroscopic swelling of polymeric materials in electronic packaging. *Journal of Electronic Packaging*, 124(2):122–126, 2002.
- [22] H. Ardebili, E. H. Wong, and M. Pecht. Hygroscopic swelling and sorption characteristics of epoxy molding compounds used in electronic packaging. *Components and Packaging Technologies, IEEE Transactions on [see also Components, Packaging and Manufacturing Technology, Part A: Packaging Technologies, IEEE Transactions on]*, 26(1):206–214, 2003. 1521-3331.
- [23] A. J. Cervenka, R. J. Young, and K. Kueseng. Micromechanical phenomena during hygrothermal ageing of model composites investigated by raman spectroscopy. part ii: comparison of the behaviour of pbo and m5 fibres compared with twaron. *Composites Part A: Applied Science and Manufacturing*, 36(7):1020–1026, 2005.
- [24] A. J. Cervenka, R. J. Young, and K. Kueseng. Micromechanical phenomena during hygrothermal ageing of model composites investigated by raman spectroscopy. part i: Twaron fibres with different surface treatments. *Composites Part A: Applied Science and Manufacturing*, 36(7):1011–1019, 2005.

- [25] K. H. G. Ashbee and R. C. Wyatt. Water damage in glass fibre/resin composites. *Proceedings of the Royal Society of London Series A-mathematical and Physical Sciences*, 312(1511):553, 1969.
- [26] W. Noobut and J. L. Koenig. Interfacial behavior of epoxy/e-glass fiber composites under wet-dry cycles by fourier transform infrared microscopy. *Polymer Composites*, 20(1):38–47, 1999.
- [27] D. H. Kaelble, P. J. Dynes, L. W. Crane, and L. Maus. Interfacial mechanisms of moisture degradation in graphite-epoxy composites. *The Journal of Adhesion*, 7(1):25 – 54, 1975.
- [28] W. Beckert and B. Lauke. Critical discussion of the single-fibre pull-out test: does it measure adhesion. *Composites Science and Technology*, 57(12):1689–1706, 1998.
- [29] M. Kuntz, K. H. Schlapschi, B. Meier, and G. Grathwohl. Evaluation of interface parameters in push-out and pull-out tests. *Composites*, 25(7):476–481, 1994.
- [30] C.H. Hsueh. Interfacial debonding and fiber pull-out stresses of fiber-reinforced composites iii: With residual radial and axial stresses. *Materials Science and Engineering A*, 145(2):135–142, 1991.
- [31] J.K. Kim, S. Lu, and Y.W. Mai. Interfacial debonding and fibre pull-out stresses. *Journal of Materials Science*, 29(2):554–561, 1994.
- [32] J.K. Kim, C. Baillie, and Y.W. Mai. Interfacial debonding and fibre pull-out stresses: Part i - critical comparison of existig theories with experiments. *Journal of Materials Science*, 27(12):3143–3154, 1992.
- [33] S. Zhandarov, E. Pisanova, E. der, and J. A. Nairn. Investigation of load transfer between the fiber and the matrix in pull-out tests with fibers having different diameters. *Journal of Adhesion Science and Technology*, 15:205–222, 2001.
- [34] A. N. Gent and C. Wang. What happens after a fiber breaks - pull-out or resin cracking. *Journal of Materials Science*, 28(9):2494–2500, 1993.

- [35] Y. S. Chai and Y.W. Mai. New analysis on the fiber push-out problem with interface roughness and thermal residual stresses. *Journal of Materials Science*, 36(8):2095–2104, 2001.
- [36] Y. Dai, J. K. Kim, and J. Park. Numerical study of the single fibre push-out test: Part iii. singularity of interface stresses. *Composite Interfaces*, 10(1):17–39, 2003.
- [37] G. Lin, P. H. Geubelle, and N. R. Sottos. Simulation of fiber debonding with friction in a model composite pushout test. *International Journal of Solids and Structures*, 38(46-47):8547–8562, 2001.
- [38] P. Feillard, G. Désarmot, and J. P. Favre. A critical assessment of the fragmentation test for glass/epoxy systems. *Composites Science and Technology*, 49(2):109–119, 1993.
- [39] P. J. Herrera-Franco and L. T. Drzal. Comparison of methods for the measurement of fibre/matrix adhesion in composites. *Composites*, 23(1):2–27, 1992.
- [40] E. Graciani, V. Mantic, F. Paris, and J. Varna. Numerical analysis of debond propagation in the single fibre fragmentation test. *Composites Science and Technology*, 69(15-16):2514–2520, 2009.
- [41] J. P. Favre and D. Jacques. Stress transfer by shear in carbon fibre model composites - part 1 results of single-fibre fragmentation tests with thermosetting resins. *Journal of Materials Science*, 25(2):1373–1380, 1990.
- [42] J. P. Favre, P. Sigety, and D. Jacques. Stress transfer by shear in carbon fibre model composites - part 2 computer simulation of the fragmentation test. *Journal of Materials Science*, 26(1):189–195, 1991.
- [43] P. Feillard, D. Rouby, G. Désarmot, and J. P. Favre. Limits of conventional micromechanical analysis of interface properties in glass-epoxy model composites. *Materials Science and Engineering A*, 188(1-2):159–166, 1994.

- [44] E. Feresenbet, D. Raghavan, and G. A. Holmes. The influence of silane coupling agent composition on the surface characterization of fiber and on fiber-matrix interfacial shear strength. *The Journal of Adhesion*, 79(7):643 – 665, 2003.
- [45] F. Ramirez and L. Carlsson. Modified single fiber fragmentation test procedure to study water degradation of the fiber/matrix interface toughness of glass/vinylester. *Journal of Materials Science*, 44:3035–3042, 2009.
- [46] P. Pandey and M. J. Sundaresan. Strain distributions and over-stressed volumes in unidirectional composites with multiple fiber breaks. *Journal of Thermoplastic Composite Materials*, 9(2):199–215, 1996.
- [47] Z.F. Li, D. T. Grubb, and S. L. Phoenix. Fiber interactions in the multi-fiber composite fragmentation test. *Composites Science and Technology*, 54(3):251–266, 1995.
- [48] M. R. Wisnom and D. Green. Tensile failure due to interaction between fibre breaks. *Composites*, 26(7):499–508, 1995.
- [49] L. Mishnaevsky. Hierarchical composites: Analysis of damage evolution based on fiber bundle model. *Composites Science and Technology*, 71(4):450–460, 2011.
- [50] C. Galiotis. Interfacial studies on model composites by laser raman spectroscopy. *Composites Science and Technology*, 42(1-3):125–150, 1991.
- [51] A. Paipetis, C. Galiotis, Y. C. Liu, and J. A. Nairn. Stress transfer from the matrix to the fibre in a fragmentation test: Raman experiments and analytical modeling. *Journal of Composite Materials*, 33(4):377–399, 1999.
- [52] S. J. Eichhorn, J. A. Bennett, Y. T. Shyng, R. J. Young, and R. J. Davies. Analysis of interfacial micromechanics in microdroplet model composites using synchrotron microfocus x-ray diffraction. *Composites Science and Technology*, 66(13):2197–2205, 2006.



- [53] Y. Shyng, J. Bennett, R. Young, R. Davies, and S. Eichhorn. Analysis of interfacial micromechanics of model composites using synchrotron micro-focus x-ray diffraction. *Journal of Materials Science*, 41(20):6813–6821, 2006.
- [54] P. Giaccari, G. R. Dunkel, L. Humbert, J. Botsis, H. G. Limberger, and Salathe R.P. On a direct determination of non-uniform internal strain fields using fibre bragg gratings. *Smart Materials and Structures*, (14):127, 2005.
- [55] N. Shibata, S. Shibata, and T. Eda Hiro. Refractive-index dispersion of lightguide glasses at high-temperature. *Electronics Letters*, 17(8):310–311, 1981.
- [56] A. Bertholds and R. Dandliker. Determination of the individual strain-optic coefficients in single-mode optical fibers. *Journal of Lightwave Technology*, 6(1):17–20, 1988.
- [57] George S. Springer R. J. Van Steenkiste. *Strain and temperature measurement with fiber optic sensors*. CRC press, 1996.
- [58] S. Leng and A. Asundi. Real-time cure monitoring of smart composite materials using extrinsic fabry-perot interferometer and fiber bragg grating sensors. *Smart Materials and Structures*, 11(2):249–255, 2002.
- [59] R.M. Measures. *Structural monitoring with fiber optic technology*. Academic Press, 2001.
- [60] P. Giaccari. *Fiber bragg grating characterization by optical low coherence reflectometry and sensing applications*. PhD thesis, EPFL, 2003.
- [61] T. Erdogan. Fiber grating spectra. *Lightwave Technology, Journal of*, 15(8):1277–1294, 1997.
- [62] J. Skaar, Wang Ligang, and T. Erdogan. On the synthesis of fiber bragg gratings by layer peeling. *Quantum Electronics, IEEE Journal of*, 37(2):165–173, 2001.

- [63] J. Skaar and R. Feced. Reconstruction of gratings from noisy reflection data. *J. Opt. Soc. Am. A*, 19(11):2229–2237, 2002.
- [64] H.L. Cox. The elasticity and strength of paper and other fibrous materials. *British Journal of Applied Physics*, (3):72, 1952.
- [65] A. Kelly and N.H. Macmillan. *Strong solids*. 1986.
- [66] J.V. Beck, B. Blackwell, and C.R. Clair. *Inverse heat conduction: Ill-posed problems*. Wiley interscience, 1985.
- [67] T. A. Bogetti and J. W. Gillespie. Process-induced stress and deformation in thick-section thermoset composite laminates. *Journal of Composite Materials*, 26(5):626–660, 1992.
- [68] M. Zarrelli, A. A. Skordos, and I. K. Partridge. Investigation of cure induced shrinkage in unreinforced epoxy resin. *Plastics Rubber and Composites*, 31(9):377–384, 2002.
- [69] D. Karalekas, J. Cugnoni, and J. Botsis. Monitoring of process induced strains in a single fibre composite using fbg sensor: A methodological study. *Composites Part a-Applied Science and Manufacturing*, 39(7):1118–1127, 2008.
- [70] R. Montanini and L. D’acquisto. Simultaneous measurement of temperature and strain in glass fiber-epoxy composites by embedded fiber optic sensors: 2. post-cure testing. *Smart Materials and Structures*, 16:1727–1735, 2007.
- [71] J.Crank. *The Mathematics of Diffusion*. Oxford science publications, 1989.
- [72] D. Fox, M. Labes, and A. Weissberger. *Physics and chemistry of the organic solid state*, volume II. John Wiley & Sons Inc, 1965. C.E. Rogers. chapter 6: Solubility and diffusivity.
- [73] X. Chen, S. Zhao, and L. Zhai. Moisture absorption and diffusion characterization of molding compound. *Journal of Electronic Packaging*, 127(4):460–465, 2005.

- [74] W. K. Loh, A. D. Crocombe, M. M. Abdel Wahab, and I. A. Ashcroft. Modelling anomalous moisture uptake, swelling and thermal characteristics of a rubber toughened epoxy adhesive. *International Journal of Adhesion and Adhesives*, 25(1):1–12, 2005.
- [75] A. A. Fahmy and J. C. Hurt. Stress dependence of water diffusion in epoxy resin. *Polymer Composites*, 1(2):77–80, 1980.
- [76] L. W. Jelinski, J. J. Dumais, A. L. Cholli, T. S. Ellis, and F. E. Karasz. Nature of the water-epoxy interaction. *Macromolecules*, 18(6):1091–1095, 1985.
- [77] J. Zhou and J.P. Lucas. Hygrothermal effects of epoxy resin. part i: the nature of water in epoxy. *Polymer*, 40(20):5505–5512, 1999.
- [78] M. K. Antoon and J. L. Koenig. Irreversible effects of moisture on the epoxy matrix in glass-reinforced composites. *Journal of Polymer Science Part B-polymer Physics*, 19(2):197–212, 1981.
- [79] M. K. Antoon, J. L. Koenig, and T. Serafini. Fourier-transform infrared study of the reversible interaction of water and a crosslinked epoxy matrix. *Journal of Polymer Science Part B-polymer Physics*, 19(10):1567–1575, 1981.
- [80] S. Cotugno, D. Larobina, G. Mensitieri, P. Musto, and G. Ragosta. A novel spectroscopic approach to investigate transport processes in polymers: the case of water-epoxy system. *Polymer*, 42(15):6431–6438, 2001.
- [81] J. Mijovic and H. Zhang. Local dynamics and molecular origin of polymer network-water interactions as studied by broadband dielectric relaxation spectroscopy, ftir, and molecular simulations. *Macromolecules*, 36(4):1279–1288, 2003.
- [82] G. Z. Xiao, M. Delamar, and M. Shanahan. Irreversible interactions between water and dgeba/dda epoxy resin during hygrothermal aging. *Journal of Applied Polymer Science*, 65(3):449–458, 1997.
- [83] A. Apicella, R. Tessieri, and C. de Cataldis. Sorption modes of water in glassy epoxies. *Journal of Membrane Science*, 18:211–225, 1984.

- 
- [84] A. N. Tikhonov and A. Samarskii. *Equations of Mathematical Physics*, volume 39 of *International series of monographs in pure and applied mathematics*. 1963.
- [85] T. S. Ellis and F.E. Karasz. Interaction of epoxy resins with water: the depression of glass transition temperature. *Polymer*, 25(5):664–669, 1984.
- [86] J. Zhou and J. P. Lucas. Hygrothermal effects of epoxy resin. part ii: variations of glass transition temperature. *Polymer*, 40(20):5513–5522, 1999.
- [87] G. C. Papanicolaou, T. V. Kosmidou, A. S. Vatalis, and C. G. Delides. Water absorption mechanism and some anomalous effects on the mechanical and viscoelastic behavior of an epoxy system. *Journal of Applied Polymer Science*, 99(4):1328–1339, 2006.
- [88] G. M. Pharr, W. C. Oliver, and F. R. Brotzen. On the generality of the relationship among contact stiffness, contact area, and elastic-modulus during indentation. *Journal of Materials Research*, 7(3):613–617, 1992.
- [89] I.N. Sneddon. The relation between load and penetration in the axisymmetric boussinesq problem for a punch of arbitrary profile. *International Journal of Engineering Science*, 3(1):47 – 57, 1965.
- [90] W. C. Oliver and G. M. Pharr. An improved technique for determining hardness and elastic-modulus using load and displacement sensing indentation experiments. *Journal of Materials Research*, 7(6):1564–1583, 1992.
- [91] W. C. Oliver and G. M. Pharr. Measurement of hardness and elastic modulus by instrumented indentation: Advances in understanding and refinements to methodology. *Journal of Materials Research*, 19(1):3–20, 2004.
- [92] W. Cheng and I. Finnie. A method for measurement of axisymmetric axial residual-stresses in circumferentially welded thin-walled cylinders. *Journal of Engineering Materials and Technology-transactions of the Asme*, 107(3):181–185, 1985.

- 
- [93] W. Cheng and I. Finnie. Comparison of the strains due to edge cracks and cuts of finite width with applications to residual stress measurement. *Journal of Engineering Materials and Technology, Transactions of the ASME*, 115(2):220–226, 1993.
- [94] I. Finnie and W. Cheng. Residual stress measurement by the introduction of slots or cracks. In *Proceedings of the 1996 4th International Conference on Computer-Aided Assessment and Control*, pages 37–51. Computational Mechanics Inc, 1996.
- [95] S. Finnie, W. Cheng, I. Finnie, J. M. Drezet, and M. Gremaud. The computation and measurement of residual stresses in laser deposited layers. *Journal of Engineering Materials and Technology*, 125(3):302–308, 2003.
- [96] G.S. Schajer. Application of finite-element calculations to residual-stress measurements. *Journal of Engineering Materials and Technology-transactions of the Asme*, 103(2):157–163, 1981.
- [97] G. S. Schajer. Measurement of non-uniform residual-stresses using the hole-drilling method: 1. stress calculation procedures. *Journal of Engineering Materials and Technology-Transactions of the Asme*, 110(4):338–343, 1988.
- [98] M. B. Prime. Residual stress measurement by successive extension of a slot: The crack compliance method. *Applied Mechanics Reviews*, 52(2):75–96, 1999.
- [99] G. S. Schajer and M. B. Prime. Use of inverse solutions for residual stress measurements. *Journal of Engineering Materials and Technology*, 128(3):375–382, 2006.
- [100] F. Colpo. *Residual stress characterization in a single fibre composite specimen by using FBG sensor and the OLCR technique*. PhD thesis, EPFL, 2006.
- [101] F. Colpo, L. Humbert, and J. Botsis. Characterisation of residual stresses in a single fibre composite with fbg sensor. *Composites Science and Technology*, 67(9):1830–1841, 2007.

- 
- [102] A.N. Tikhonov, A.V. Goncharsky, V.V. Stepanov, and A.G. Yagol. *Numerical methods for the solution of Ill-posed problems*. Kluwer Academic Publishers, 1995.
- [103] D. Karalekas, J. Cugnoni, and J. Botsis. Monitoring of hygrothermal ageing effects in an epoxy resin using fbg sensor: A methodological study. *Composites Science and Technology*, 69(3-4):507–514, 2009.
- [104] H.T. Hahn and R.Y. Kim. Swelling of composite laminates. *Advanced Composite Materials Environmental Effects*, ASTM STP 658:98–120, 1978. ASTM 658.
- [105] M.I. Daniel and I. Ori. *Engineering Mechanics of Composite Materials*. Oxford, 2006.
- [106] *Abaqus Manual V.6.8*.
- [107] <http://www.matweb.com>, 2008.
- [108] K. Liao and Y.M. Tan. Influence of moisture-induced stress on in situ fiber strength degradation of unidirectional polymer composite. *Composites Part B: Engineering*, 32(4):365–370, 2001.
- [109] D. Varelas. *Mechanical reliability of optical fiber Bragg gratings*. PhD thesis, EPFL, 1998.
- [110] C. Galiotis and A. Paipetis. Definition and measurement of the shear-lag parameter, beta, as an index of the stress transfer efficiency in polymer composites. *Journal of Materials Science*, 33(5):1137–1143, 1998.
- [111] M.L. Williams. The stresses arounds a fault or crack in dissimilar media. *Bulletin of the seismological society of america*, 49(2):199–204, 1959.
- [112] J. Dundurs and D. B. Bogy. Edge-bonded dissimilar orthogonal elastic wedges under normal and shear loading. *Journal of Applied Mechanics*, 36(3):650–652, 1969.
- [113] A. H. England. A crack between dissimilar media. *Journal of Applied Mechanics*, 32(2):400–&, 1965.

- [114] F. Erdogan. Stress distribution in bonded dissimilar materials with cracks. *Journal of Applied Mechanics*, 32(2):403–410, 1965.
- [115] J. R. Rice. Elastic fracture-mechanics concepts for interfacial cracks. *Journal of Applied Mechanics-Transactions of the Asme*, 55(1):98–103, 1988.
- [116] P.P. Camanho and C.G. Davila. Mixed-mode decohesion finite elements for the simulation of delamination in composite materials. *NASA/TM-2002-211737*, pages 1–37, 2002.
- [117] A. Sekulic and A. Curnier. Experimentation on adhesion of epoxy. *International Journal of Adhesion and Adhesives*, 30(2):89–104, 2010.
- [118] A. Sekulic and A. Curnier. An original epoxy-stamp on glass-disc specimen exhibiting stable debonding for identifying adhesive properties between glass and epoxy. *International Journal of Adhesion and Adhesives*, 27(8):611–620, 2007.
- [119] W. D. Drotning and E. P. Roth. Effects of moisture on the thermal expansion of poly(methylmethacrylate). *Journal of Materials Science*, 24(9):3137–3140, 1989.
- [120] D. Coric, M. Lai, J. Botsis, A. P. Luo, and H. G. Limberger. Distributed strain measurements using fiber bragg gratings in small-diameter optical fiber and low-coherence reflectometry. *Optics Express*, 18(25):26484–26491, 2010.
- [121] A. D. Kersey, M. A. Davis, H. J. Patrick, M. LeBlanc, K. P. Koo, C. G. Askins, M. A. Putnam, and E. J. Friebele. Fiber grating sensors. *Light-wave Technology, Journal of*, 15(8):1442–1463, 1997.
- [122] M. Lai, J. Botsis, D. Coric, and J. Cugnoni. On the degree of conversion and coefficient of thermal expansion of a single fiber composite using a fbg sensor. In D. Acierno, A. Damore, and L. Grassia, editors, *4th International Conference on Times of Polymers TOP and Composites*, pages 135–137. Amer Inst Physics, 2008.

# Curriculum Vitæ

Marco Lai

July 26, 2011

## Personal Information



*Date of Birth:* 7 July 1980  
*Place of Birth:* Nùoro, Sardinia, Italy  
*e-mail:* marco.lai@a3.epfl.ch

## Personal Interests & Skills

The main field of interest is the stress analysis of aerospace structures with particular attention to fatigue and damage tolerance of metal and composite materials. The attraction to the experimental work is associated to the interest in finite element simulations to design experiments and to analyze the results. The research conducted on composite materials motivates the attention to the micromechanical analysis as a tool to build more reliable multiscale models for the prediction of complex behavior of structures. In this framework, the mastering of the optical fiber sensing technology, that I achieved during the Phd, represents an important background extremely helpful for the study and monitoring of the internal deformation of composite components.

## Education

---

*2011:* PhD in mechanics of solids  
LMAF (Laboratoire de mécanique appliquée et analyse de fiabilité), EPFL, Lausanne.  
Phd Thesis: “**Hygrothermal ageing and damage characterization in epoxies and epoxy-glass interfaces: a micromechanical approach using embedded optical sensors**”

*2006:* Master Science degree in Aerospace Engineering with specialization in structures, Politecnico di Torino.  
Master Thesis: “**Fatigue crack growth of lightweight aerospace alloys with nanometric microstructure**”

## Teaching Experiences

---

*2007-2011:* Assistant for the course “Mechanics of Structures”, Prof. J. Botsis, LMAF, EPFL.

*2009-2011:* Assistant for the course “Continuum Mechanics”, Prof. J. Botsis, LMAF, EPFL.



## Working Experiences

---

- 2011:** **Member of local organizing committee**  
for the 5th International Conference on Composite Testing and  
Model Identification, COMPTTEST2011, Lausanne
- 2007:** Research grant awarded by Politecnico di Torino on  
“**Fatigue crack growth of magnesium alloy subjected to  
innovative thermal treatment**”.

## Selected Projects

---

### PhD thesis:

During the PhD I have successfully developed a micromechanical approach for the study of the hygrothermal ageing in composites. A single fiber composite was chosen and followed from processing through ageing. The main attractive of this methodology is the possibility of using as the cell's reinforcement an optical fiber having a fiber Bragg grating sensor (FBG). In fact, the internal strain field can be recorded during process, having access to important knowledge on the residual strain formation, and during ageing allowing the unique possibility of following the interface damage evolution triggered by the water uptake. The work led to the determination of the influence that residual strains have on the hygrothermal response in a single fiber composite.

### Particles reinforced epoxy:

The project was conducted in conjunction with the Institute for Composite Materials (IVW GmbH), Technical University of Kaiserslautern. It was aimed at the residual stress characterization, using FBG sensors, of an epoxy resin loaded with increasing volume fractions of  $SiO_2$  nanoparticles and rubber macroparticles. In addition the thermal response of the compounds was also determined.

### Reduction of the intrusiveness of FBG sensors:

The project was conducted in conjunction with the applied optical laboratory (LOA) of the EPFL. It was aimed at the demonstration of the advantages in conducting distributed strains measurements in optical fibers of reduced diameter, 50 $\mu$ m, using the optical low coherence reflectometry (OLCR). It was proved that the same accuracy in strain detection is reached, in comparison with standard telecommunication fibers, guaranteeing, at the same time, reduced intrusiveness of the sensor in the structure.

## Competences

---

### Softwares:

Word, Excel, Power Point, Lyx  
Matlab, FORTRAN, Python  
Abaqus, COMSOL Multiphysics  
CATIA V5

### Languages:

Italian, mother tongue  
French, good command  
English, good command

## List of Publications

---

- 2010:** **M. Lai**, J. Botsis, J. Cugnoni and D. Coric, An experimental-numerical study of moisture absorption in an epoxy, (2010), submitted  
**Lai M.**, Friedrich K., Botsis J., Burkhart T., Evaluation of residual strains in epoxy with different nano/micro-fillers using embedded fiber Bragg grating sensor, Composites Science and Technology, 70, pp. 2168-2175, (2010)  
Coric D., **Lai M.**, Botsis J., Luo A.P., Limberger, H. G., Distributed strain measurements using fiber Bragg gratings in small-diameter optical fiber and low-coherence reflectometry, Optics Express, 18, 25, pp. 26484-26491, (2010)
- 2008:** **M. Lai**, J. Botsis, D. Coric and J. Cugnoni, On the degree of conversion and coefficient of thermal expansion of a single fiber composite using a FBG sensor, AIP conference proceedings 1042, pp. 135-137, (2008)

## Conference participation

---

- 2011:** **M. Lai**, J. Cugnoni and J. Botsis, Analysis of hygrothermally induced fiber Fracture and interface damage in a single fiber composite, 5th international conference on composites testing and model identification, COMPTEST2011, Lausanne, (2011)
- 2010:** **M. Lai**, J. Cugnoni, and J. Botsis, Analysis of hygrothermally induced fiber fracture in single fiber composite using fiber Bragg grating, ICEM14, Poitiers, (2010)
- 2009:** **Lai M.**, C. Shizas, D. Coric, D. Karalekas and J. Botsis, FBG based investigation of the degree of consolidation in cured resins, ICCS 15 Porto, (2009)  
**M. Lai**, J. Cugnoni, J. Botsis, D. Coric, Analysis of accelerated ageing of a single fiber composite, Summer school, CCMX, EPFL, (2009)  
**M. Lai**, J. Botsis, D. Coric and J. Cugnoni, On moisture induced property changes and stress analysis of a single fiber composite during ageing, proceeding of international conference on composite materials ICCM 17 (F1:15), Edimburgh, (2009)
- 2008:** **M. Lai**, J. Botsis, J. Cugnoni and D. Coric , The Hygro-Thermal Response of a Glass-Epoxy Single Fibre Composite Using FBG Distributed Sensing and Numerical Modeling, Fractures of polymers, Les diablerets, (2008)  
J. Botsis, **M. Lai**, J. Cugnoni and D. Coric, Effects of moisture on ageing and debonding in a single fiber composite using a long FBG sensor and numerical modeling, COMPTEST2008, Dayton, (2008)